

ABSTRACT

HOU, TIAN. Fatigue Performance Prediction of North Carolina Mixtures Using Simplified Viscoelastic Continuum Damage Model. (Under the direction of Dr. Y. Richard Kim.)

Fatigue performance modeling is one the major topics in asphalt concrete modeling work. Currently the only standard fatigue test available for asphalt concrete mixtures is the flexural bending fatigue test, AASHTO T-321. There are several issues associated with flexural fatigue testing, the most important of which are the stress state is not uniform but varies over the depth of the specimen and equipment for fabricating beam specimens is not widely available. Viscoelastic continuum damage (VECD) fatigue testing is a promising alternative to flexural fatigue testing. Different researchers have successfully applied the VECD model to asphalt concrete mixtures using constant crosshead rate direct tension test. However, due to the load level limitation of the new coming Asphalt Mixture Performance Tester (AMPT) testing equipment, there is an immediate need to develop a model that can characterize fatigue performance quickly using cyclic test data. In this study, a simplified viscoelastic continuum damage model developed at NCSU is applied to various North Carolina mixtures, which are used in the NCDOT HWY-2007-7 MEPDG local calibration project. It is shown that the simplified VECD model can predict fatigue tests fairly accurately under various temperature conditions and strain levels. It is also shown that the model can be further utilized to simulate both the strain controlled direct tension fatigue test and the traditional beam fatigue test. In this thesis, simulation results are presented. Conclusions regarding the applicability of the new model are advanced as well as suggestions for further work.

Fatigue Performance Prediction of North Carolina Mixtures Using Simplified Viscoelastic
Continuum Damage Model

by
Tian Hou

A thesis submitted to the Graduate Faculty of
North Carolina State University
in partial fulfillment of the
requirements for the degree of
Master of Science

Civil Engineering

Raleigh, North Carolina

2009

APPROVED BY:

Dr. Y. Richard Kim
Committee Chair

Dr. Murthy N. Guddati

Dr. Roy H. Borden

DEDICATION

To my parents

BIOGRAPHY

Tian Hou was born in 1985 in Wuxi, Jiangsu Province, China, where he spent his childhood. In 2004, he joined the University of Hong Kong as one of the ninety mainland students, majoring in Civil Engineering. He received his Bachelor of Engineering degree with First Class Honor in May, 2007, and the same year, in July, he came to North Carolina State University, Raleigh, North Carolina, US to study for his Master of Science degree in Civil Engineering under the supervision of Dr. Y. Richard Kim.

ACKNOWLEDGMENTS

First of all, I want to thank my advisor, Dr. Y. Richard Kim. Without his guidance and encouragement, the research for this thesis would not be possible. I also would like to acknowledge my research group mates. Shane Underwood, the most talented young researcher that I have ever met, is always a good example for me to follow. Without his patience to answer my questions, I cannot solve headaches so quickly. A special thanks to Fadi Jadoun, my 'big brother', who works on the same project with me. I cannot imagine I will survive without his help moving and carrying tons of aggregates from the quarry. Current and former group members, Charlie Cheolmin Baek, Andrew Lacroix, Taeyoung Yun, Jaejun Lee, Yeongtae Choi, also greatly contributed in various encouraging and practical ways.

I would like to thank my parents, who deliver endless encouraging voices through telephone far away from China every week. In the end, I would like to thank my girlfriend, Zihan Cao, who stays with me, encourages me and supports me throughout my hard time. Meeting with you is the most beautiful thing for me in the United States.

TABLE OF CONTENTS

LIST OF FIGURES	viii
LIST OF TABLES	xiii
Chapter 1 Introduction	1
1.1 Fatigue Tests and Fatigue Models for Asphalt Concrete	1
1.1.1 <i>Flexural bending test</i>	1
1.1.2 <i>Simplified fatigue test with viscoelastic continuum damage model</i>	3
1.2 Research Needs and Research Objective	5
Chapter 2 Theoretical Background	7
2.1 Linear Viscoelasticity Theory	7
2.2 Complex Modulus	7
2.3 Time-Temperature Superposition Principle	8
2.4 Interconversion between Unit Response Functions	12
2.5 Elastic-Viscoelastic Correspondence Principle	14
2.6 Viscoelastic Continuum Damage Theory	15
Chapter 3 Specimen Preparation and Experimental Program	18
3.1 Materials	18

3.2	Specimen Fabrication.....	21
3.3	Test Set-up	21
3.4	Test Methods.....	22
3.4.1	<i>Complex modulus test</i>	22
3.4.2	<i>Controlled crosshead cyclic test</i>	24
3.5	Failure Definition in Cyclic Test	25
Chapter 4 Simplified VECD Model		27
4.1	Rigorous Modeling Approach.....	27
4.2	Simplified Modeling Approach	28
4.2.1	<i>Defining Alpha</i>	29
4.2.2	<i>Identification of tensile loading time</i>	30
4.2.3	<i>Simplification and adjustment factor</i>	32
4.2.4	<i>Specimen-to-specimen variability</i>	33
4.2.5	<i>Model formulation</i>	34
Chapter 5 Test Results and Model Verification.....		36
5.1	Linear Viscoelastic Characterization	36
5.2	Viscoelastic Damage Characterization	39
Chapter 6 Model Application		50

6.1	Simulation Failure Envelope.....	50
6.2	Fatigue Test Prediction	52
6.3	Further Development of Failure Envelope Using Optimization Technique	58
6.4	Direct Tension Fatigue Simulation	64
6.5	Beam Fatigue Simulation.....	71
Chapter 7 Conclusions and Future Research Recommendations		81
References.....		82
Appendices.....		84
	Appendix A Complex Modulus Test Data.....	85
	Appendix B Comparison of DMR and I.....	98
	Appendix C Damage Characterization Data.....	110
	Appendix D Comparison of Different Failure Definitions in Cyclic Test.....	112
	Appendix E Fatigue Test Prediction Results	115

LIST OF FIGURES

Figure 1.1 Beam fatigue test configuration and specimen dimension	2
Figure 1.2 Flowchart of the simplified fatigue test program	5
Figure 2.1 Graphical representation of complex modulus in complex plane	8
Figure 2.2 Horizontal shifting of $ E^* $ value from different temperatures to reference temperature (5°C)	10
Figure 2.3 Shifted $ E^* $ mastercurve	11
Figure 2.4 Example of time-temperature shift factor function curve	11
Figure 2.5 Typical test result from a constant crosshead rate tension test: (a) stress-strain plot; (b) stress-pseudo strain plot	15
Figure 3.1 Mixture gradation chart	18
Figure 3.2 Test set-up	22
Figure 3.3 Stress and strain history plot in a typical tension-compression complex modulus test	23
Figure 3.4 Strain and stress history for first five cycles of a typical CX test	25
Figure 3.5 Fatigue life (N_f) definition of a typical good CX cyclic test	26
Figure 4.1 Schematic view of variables defined in simplified modeling approach for controlled crosshead cyclic test	29
Figure 4.2 Loading history for a typical cycle during controlled crosshead cyclic test	31
Figure 5.1 Average dynamic modulus mastercurves for all mixes (semi-log)	37
Figure 5.2 Average dynamic modulus mastercurves for all mixes (log-log)	37

Figure 5.3 Average phase angle mastercurves for all mixes (semi-log).....	38
Figure 5.4 Shift factor functions for all mixes.....	38
Figure 5.5 Damage curves for (a) S9.5C; (b) S9.5B; (c) I19C; (d) B25B; (e) RS9.5C mix...	42
Figure 5.6 Damage curves for (a) S12.5C; (b) I19B; (c) RS12.5C; (d) RI19B; (e) RI19C; (f) RB25B mix.	44
Figure 5.7 Failure locations of CX cyclic tests: (a) mid-failure; (b) end-failure.....	45
Figure 5.8 Damage curves for CX cyclic tests with different failure locations: (a) S9.5B; (b) I19C; (c) RS12.5C; (d) I19B; (e) RI19C.	47
Figure 5.9 Damage characteristic curves for all mixtures	49
Figure 6.1 Failure envelope for fatigue test simulation	51
Figure 6.2 Typical good pseudo stiffness prediction (RI19B-5)	54
Figure 6.3 Typical bad pseudo stiffness prediction (I19C-10)	54
Figure 6.4 Controlled-crosshead cyclic test simulation results for (a) S9.5C; (b) S9.5B; (c) I19C; (d) B25B; (e) RS9.5C mix.....	55
Figure 6.5 Controlled-crosshead cyclic test simulation results for (a) S12.5C; (b) I19B; (c) RS12.5C; (d) RI19B; (e) RI19C; (f) RB25B mix.....	56
Figure 6.6 Comparison of measured and predicted fatigue life for all mixtures in (a) arithmetic scale; (b) log scale	57
Figure 6.7 Fatigue life prediction result in (a) arithmetic; (b) log scale after minimizing total prediction error in arithmetic scale	59

Figure 6.8 Fatigue life prediction result in (a) arithmetic; (b) log scale after minimizing total prediction error in log scale	59
Figure 6.9 Optimized failure envelope	60
Figure 6.10 Optimized slope coefficients versus NMAS	61
Figure 6.11 Final failure envelope	63
Figure 6.12 Fatigue life prediction result using final failure envelope	63
Figure 6.13 Strain controlled direct tension fatigue test simulation results for (a) S9.5C; (b) S9.5B; (c) I19C; (d) B25B and (e) RS9.5C.	67
Figure 6.14 Strain controlled direct tension fatigue test simulation results for (a) S12.5C; (b) I19B; (c) RS12.5C; (d) RI19B; (e) RI19C and (f) RB25B.	68
Figure 6.15 5°C strain controlled direct tension fatigue test simulations for all mixtures	70
Figure 6.16 19°C strain controlled direct tension fatigue test simulations for all mixtures ...	70
Figure 6.17 27°C strain controlled direct tension fatigue test simulations for all mixtures ...	71
Figure 6.18 Beam fatigue test simulation process	73
Figure 6.19 Example of beam fatigue simulation result	74
Figure 6.20 Beam fatigue test simulation results for (a) S9.5C; (b) S9.5B; (c) I19C; (d) B25B and (e) RS9.5C.	75
Figure 6.21 Beam fatigue test simulation results for (a) S12.5C; (b) I19B; (c) RS12.5C; (d) RI19B; (e) RI19C and (f) RB25B.	76
Figure 6.22 5°C beam fatigue test simulations for all mixtures	78
Figure 6.23 19°C beam fatigue test simulations for all mixtures	78

Figure 6.24 27°C beam fatigue test simulations for all mixtures	79
Figure B. 1 Damage curves for S9.5C mixture using (a) DMR and (b) I as specimen-to-specimen variability factor.....	99
Figure B. 2 Damage curves for S9.5B mixture using (a) DMR and (b) I as specimen-to-specimen variability factor.....	100
Figure B. 3 Damage curves for I19C mixture using (a) DMR and (b) I as specimen-to-specimen variability factor.....	101
Figure B. 4 Damage curves for B25B mixture using (a) DMR and (b) I as specimen-to-specimen variability factor.....	102
Figure B. 5 Damage curves for RS9.5C mixture using (a) DMR and (b) I as specimen-to-specimen variability factor.....	103
Figure B. 6 Damage curves for S12.5C mixture using (a) DMR and (b) I as specimen-to-specimen variability factor.....	104
Figure B. 7 Damage curves for I19B mixture using (a) DMR and (b) I as specimen-to-specimen variability factor.....	105
Figure B. 8 Damage curves for RS12.5C mixture using (a) DMR and (b) I as specimen-to-specimen variability factor.....	106
Figure B. 9 Damage curves for RI19B mixture using (a) DMR and (b) I as specimen-to-specimen variability factor.....	107
Figure B. 10 Damage curves for RI19C mixture using (a) DMR and (b) I as specimen-to-specimen variability factor.....	108

Figure B. 11 Damage curves for RB25B mixture using (a) DMR and (b) I as specimen-to-specimen variability factor..... 109

Figure D. 1 Comparison of different failure definitions: (a) arithmetic scale; (b) log scale 113

LIST OF TABLES

Table 3.1 Summary of the Eleven Most Popular Mixes in North Carolina.....	20
Table 5.1 Summary of controlled-crosshead cyclic test results.....	40
Table 5.2 Summary of failure locations for all CX cyclic tests.....	46
Table 6.1 Coefficients for failure envelope	52
Table 6.2 Optimized failure envelope coefficients	60
Table 6.3 Summary of regression coefficients for empirical model from direct tension fatigue simulation.....	69
Table 6.4 Summary of regression coefficients for empirical model from beam fatigue simulation.....	77
Table 6.5 Summary of fatigue performance ranking	80
Table A.1 Summary of sigmoidal coefficients and shift factor coefficients for all mixtures ..	86
Table A.2 Complex Modulus Test Result Data for S9.5C Mixture.....	87
Table A.3 Complex Modulus Test Result Data for S9.5B Mixture.....	88
Table A.4 Complex Modulus Test Result Data for I19C Mixture	89
Table A.5 Complex Modulus Test Result Data for B25B Mixture	90
Table A.6 Complex Modulus Test Result Data for RS9.5C Mixture.....	91
Table A.7 Complex Modulus Test Result Data for S12.5C Mixture.....	92
Table A.8 Complex Modulus Test Result Data for I19B Mixture	93
Table A.9 Complex Modulus Test Result Data for RS12.5C Mixture.....	94
Table A.10 Complex Modulus Test Result Data for RI19B Mixture.....	95

Table A.11 Complex Modulus Test Result Data for RI19C Mixture.....	96
Table A.12 Complex Modulus Test Result Data for RB25B Mixture	97
Table C. 1 Viscoelastic damage characterization coefficients for all mixtures.....	111
Table D. 1 Experimental measured fatigue lives by two different definitions	114
Table E. 1 Summary of fatigue test prediction results.....	116

Chapter 1 Introduction

Fatigue cracking is one of the major types of distress in asphalt concrete pavements. This form of distress results from the application of repeated traffic loading which causes failure in flexible pavements. Depending on the failure mechanisms and the location of crack initiation, fatigue cracking can be classified into bottom-up fatigue cracking and top-down fatigue cracking. Propagation of fatigue cracks throughout the asphalt layer will eventually allow water to come into unbounded layer, and cause deterioration of pavement structure and its serviceability. Thus, accurate description and prediction of fatigue resistance of hot mix asphalt (HMA) is extremely important to flexible pavement design and preservation.

1.1 Fatigue Tests and Fatigue Models for Asphalt Concrete

In order to simulate the fatigue performance of asphalt concrete in the field, different scientists and researchers have developed various laboratory fatigue tests and models. In this section, two major fatigue test methods are discussed, which are (1) flexural bending test, and (2) direct tension test.

1.1.1 Flexural bending test

The most popular flexural bending test is the standard beam fatigue test, which measures the fatigue life of a compacted asphalt beam subjected to repeated flexural bending. The standard procedure for beam fatigue test is described in the AASHTO T-321 standard, and it was

adopted by researchers at University of California Berkeley under the Strategic Highway Research Program (SHRP) Project (SHRP 1994; Tayebali et al. 1995). The standard rectangular beam size used for the fatigue test is 380 mm long by 63 mm wide by 50 mm thick. The specimen dimensions and test configurations are illustrated in Figure 1.1.

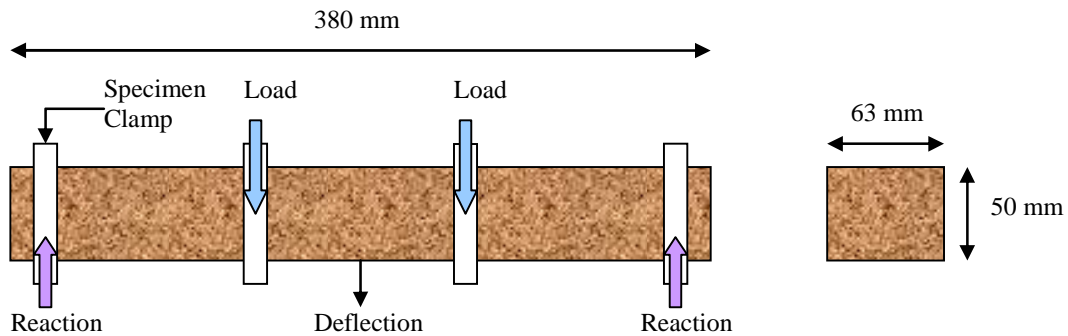


Figure 1.1 Beam fatigue test configuration and specimen dimension

To produce a uniformly distributed bending moment throughout the mid-span of the beam, loads are applied at two third points. During the test, mid-span deflection, strain, and load are recorded at each cycle. A control and data acquisition system is used so that it helps adjust the load and ensures specimen undergoes a constant level of strain on each load cycle. Specimen stiffness at the 50th load cycles is used as an estimate of the initial stiffness and failure point is defined as the load cycle at which the specimen exhibits a 50 percent reduction in stiffness relative to that initial stiffness.

It has been accepted for many years that the fatigue performance of asphalt concrete mixtures can be characterized by either strain based or stress based equations:

$$N_f = k_1 \left(\frac{1}{\epsilon_0} \right)^{k_2} \quad (1.1)$$

$$N_f = k_1 \left(\frac{1}{\sigma_0} \right)^{k_2} \quad (1.2)$$

where

N_f = number of cycles to failure;

ε_0 and σ_0 = initially applied strain and stress amplitudes; and

k_1, k_2 = material constants.

Later, it was suggested by Monismith et al. (1985) to include the mixture stiffness term into the equations so that the temperature effect can be taken into consideration as in Equation (1.3).

$$N_f = k_1 \left(\frac{1}{\varepsilon_0} \right)^{k_2} (|E^*|)^{k_3} \quad (1.3)$$

In the recently developed Mechanistic-Empirical Pavement Design Guide (MEPDG), the mathematical model shown above is selected as an input to predict fatigue performance of HMA, except that a laboratory to field adjustment factor is added.

1.1.2 Simplified fatigue test with viscoelastic continuum damage model

All the traditional fatigue tests, such as the beam fatigue test described in the previous section, are empirical in nature, which could introduce large errors when used in material performance prediction. Nowadays researchers and asphalt industry are moving toward the mechanistic approaches, which include more rigorous theoretical considerations. The viscoelastic continuum damage (VECD) model is such a technique that makes use of

materials' fundamental properties and helps develop a much simplified laboratory test program.

The history of the VECD model started with Kim and Little (1990), who first successfully applied Schapery's (1981) nonlinear viscoelastic constitutive theory for materials with distributed damage to sand asphalt under cyclic loading. Later Lee and Kim (1998) developed the VECD model and proved that it can be applied to asphalt concrete under both controlled stress and controlled strain cyclic loading. The work of Daniel and Kim (2002) showed that damage characteristics of asphalt concrete is a material property and can be determined using a simplified procedure such as constant crosshead rate monotonic direct tension test. Later it was shown by Chehab et al. (2002, 2003) that the time-temperature superposition (t-TS) can be extended from material's linear viscoelastic range to high damaged levels, which helps reduce the required testing time significantly. The most recent work was done by Underwood (2006), who applied these principles to mixtures tested at the Federal Highway Administration Accelerated Load Facility (FHWA ALF) in McLean, VA, demonstrated the use of the modeling principles to both modified and unmodified asphalt concrete mixtures, and successfully predicted the ALF mixture fatigue resistance ranking using the simplified VECD model. The theoretical background behind the test method and model is discussed in details in Chapter 2.

As a summary, the flowchart of simplified fatigue test program with the help of VECD model is illustrated in Figure 1.2. The major advantages of this test program include: (1) much shorter testing time; (2) ability to take into account many different conditions due to its

theoretically-based nature; and (3) ability to separate material property from structure component.

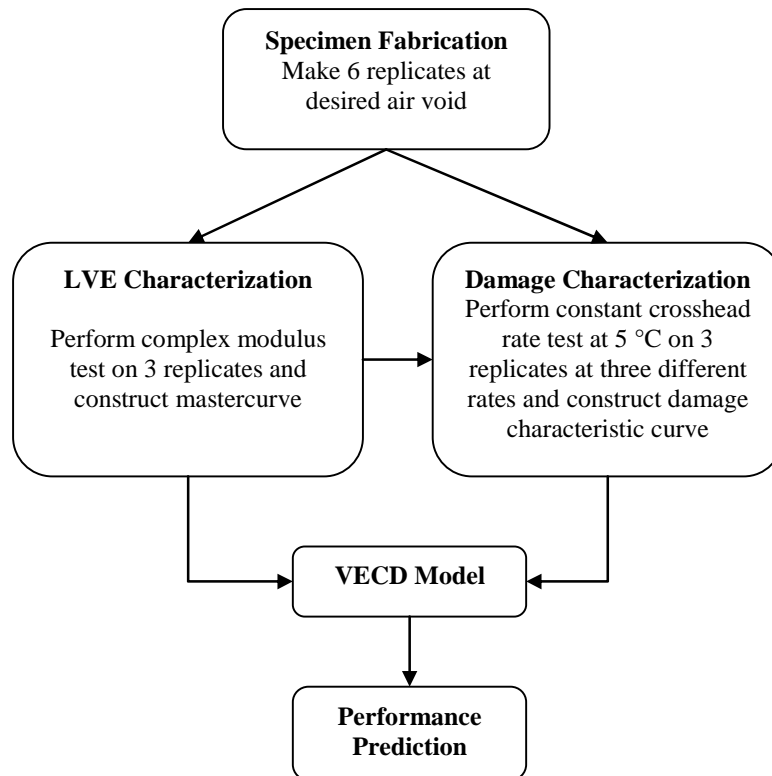


Figure 1.2 Flowchart of the simplified fatigue test program

1.2 Research Needs and Research Objective

As stated in the previous section, the VECD model is much simpler than traditional beam fatigue test for fatigue performance characterization purpose. However, there are still several existing shortcomings. One is that the characterization process requires constant rate tests, which is theoretically appropriate for the work potential theory formulation, but there are

certain practical constraints with regard to testing machine load capacity requirements. This issue is particularly important because the capacity of the Asphalt Mixture Performance Tester (AMPT) is nearly equal to the threshold value needed for constant rate testing. Thus there is an immediate need to develop a model that not only applies to cyclic fatigue test data, but also can be characterized quickly and easily using such tests.

Different researchers have been working on developing a simplified mechanistic model. Christensen and Bonaquist (2005) developed such a model based on the approach suggested by Kim et al. (2002), in which simplifications are made in the calculation of pseudo strain and in the idealization of the input conditions. Kutay and associates (2008) applied a form of the VECD model and showed that two different test protocols, controlled stress and controlled crosshead push-pull tests, yield the same damage characteristic relationship. Although these research efforts have shown positive results, it is felt that they have certain faults that limit their applications. Underwood (2009) at NCSU proposed a more rigorously accurate simplified model, which was able to correct the deficiencies in other models. The model was developed to characterize asphalt concrete mixtures using cyclic fatigue test.

The major objective of this research is to verify the simplified VECD model by applying it to various types of asphalt concrete mixtures under various conditions. Also, in the latter part of this thesis, different applications of the simplified fatigue model are discussed, and results are shown when using it to simulate and predict the fatigue performance of different asphalt concrete mixtures.

Chapter 2 Theoretical Background

2.1 Linear Viscoelasticity Theory

For linear elastic materials, the stress-strain relationship can be simply described using Hooke's Law, i.e. the stress and strain are linearly proportional to each other and the materials' response is affected only by the current input. For viscoelastic materials, which exhibit time dependent behavior, their response is not only affected by the current input, but also the past input history. For non-aging, linear viscoelastic material, the stress-strain relationship can be expressed by the following two convolution integrals.

$$\sigma = \int_0^t E(t-\tau) \frac{d\varepsilon}{d\tau} d\tau \quad (2.1)$$

$$\varepsilon = \int_0^t D(t-\tau) \frac{d\sigma}{d\tau} d\tau \quad (2.2)$$

where

$E(t)$ = relaxation modulus;

$D(t)$ = creep compliance; and

τ = integration variable.

2.2 Complex Modulus

Besides relaxation modulus ($E(t)$) and creep compliance ($D(t)$), complex modulus (E^*) is another important parameter that can capture the linear viscoelastic behavior of asphalt

concrete. Complex modulus is composed of two parts: storage modulus (E') representing the elastic portion, and loss modulus (E'') representing the viscous portion. In complex number notation, it can be written in the form of Equation (2.3), and in complex plane, it can be represented graphically as shown in Figure 2.1.

$$E^* = E' + iE'' \quad (2.3)$$

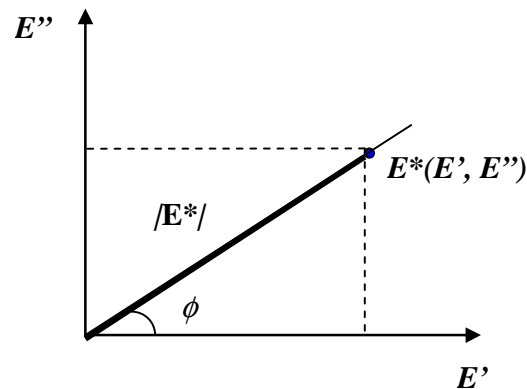


Figure 2.1 Graphical representation of complex modulus in complex plane

The important use of complex modulus involves in obtaining relaxation modulus and creep compliance by interconversion, and the details will be explained in Section 2.4.

2.3 Time-Temperature Superposition Principle

For viscoelastic material such as asphalt concrete, its stiffness is dependent on time (or rate of loading) and temperature. To capture the full range, stiffness tests need to be performed at multiple loading frequencies and temperatures. However, due to the limitation of machine capacity and testing time, such a task is always difficult to accomplish. The time-temperature

superposition (t-TS) principle can make great contribution here by reducing the required testing time significantly.

According to the principle, the same stiffness value can be obtained either at low test temperatures and long times or at high test temperatures but short times. In another word, the time and temperature effect can be combined into a single parameter. This process can be done by horizontally shifting modulus values at different temperatures to a certain reference temperature (Figure 2.2).

The shifted frequency is called reduced frequency, f_R , which can be obtained by multiplying the original frequency by a shift factor, as shown in Equations (2.4) and (2.5). A single mastercurve can then be obtained, and it can be represented by the sigmoidal function as Equation (2.6). A typical dynamic modulus mastercurve and a shift factor function curve are presented in Figure 2.3 and Figure 2.4. A material in which a single mastercurve can be formed by such shifting method is call thermorheologically simple (TRS) material.

$$f_R = f \times a_T \quad (2.4)$$

where

f = frequency in Hz; and

a_T = shift factor.

$$\log a_T = \alpha_1 T^2 + \alpha_2 T + \alpha_3 \quad (2.5)$$

where

α_1 , α_2 and α_3 = coefficients; and

T = temperature.

$$\log |E^*| = a + \frac{b}{1 + \frac{1}{e^{d+g \cdot \log f_R}}} \quad (2.6)$$

where

a, b, c and $d =$ coefficients; and

$f_R =$ reduced frequency.

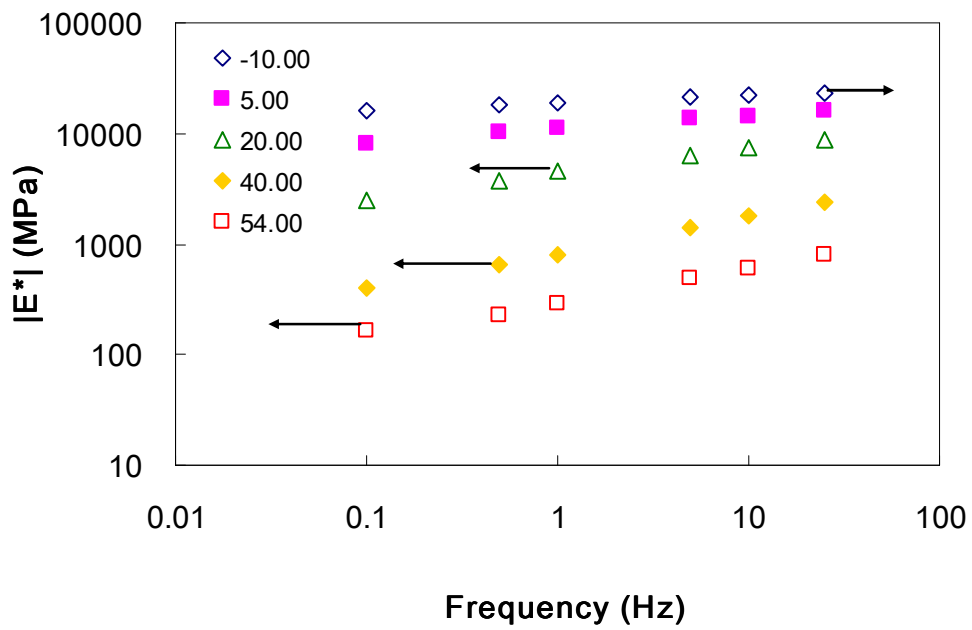


Figure 2.2 Horizontal shifting of $|E^*|$ value from different temperatures to reference temperature (5°C)

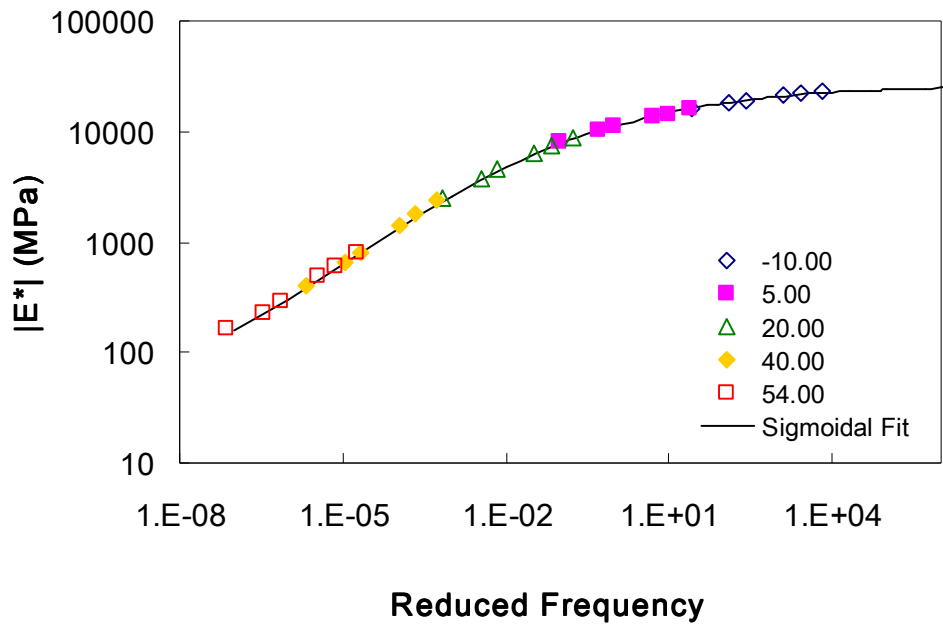


Figure 2.3 Shifted $|E^*|$ mastercurve

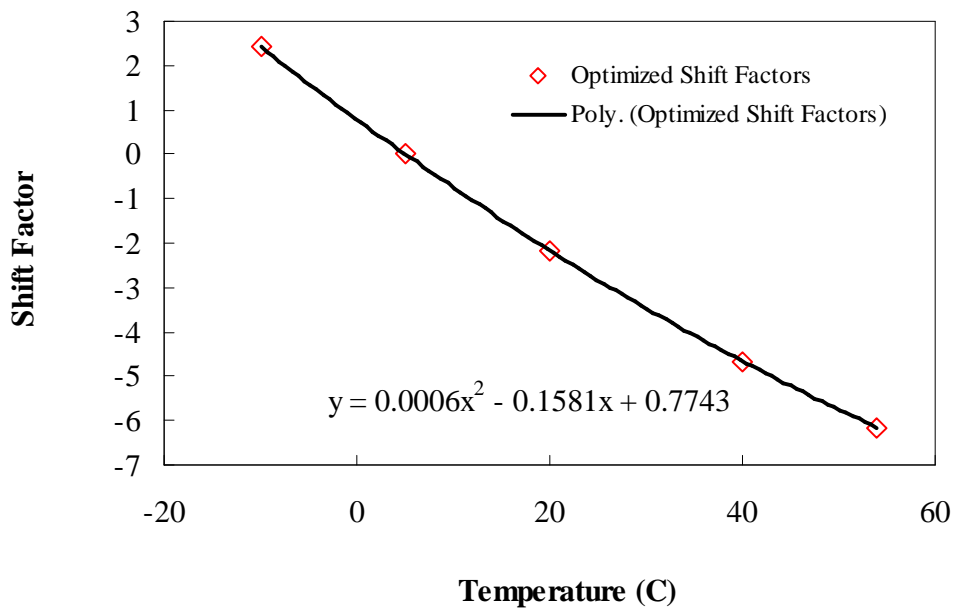


Figure 2.4 Example of time-temperature shift factor function curve

2.4 Interconversion between Unit Response Functions

Relaxation modulus ($E(t)$), creep compliance ($D(t)$), and complex modulus (E^*) are all called unit response functions, as they are equivalent to the output due to a certain type of unit input. For example, $E(t)$ is equivalent to the stress response due to a unit step strain input; and $D(t)$ is equivalent to the strain response due to a unit step stress input. These two unit response functions are not easy to obtain experimentally in time domain; however, they can be converted from complex modulus in frequency domain through linear viscoelastic theory. In the converting process, storage modulus (E') is first determined by Equation (2.7) and then expressed using Prony series representation in angular frequency domain as shown in Equation (2.8).

$$E' = |E^*| \cos \phi \quad (2.7)$$

$$E'(\omega) = E_\infty + \sum_{i=1}^m \frac{\omega^2 \rho_i^2 E_i}{\omega^2 \rho_i^2 + 1} \quad (2.8)$$

where

E_∞ = elastic modulus;

ω = angular frequency;

E_i = Prony coefficients; and

ρ_i = relaxation time.

Using experimentally obtained E' value and collocation method, Prony coefficients (E_i 's) can be determined. These coefficients are then used in Equation (2.9) to find out the relaxation modulus.

$$E(t) = E_\infty + \sum_{i=1}^m E_i e^{-\frac{t}{\rho_i}} \quad (2.9)$$

According to the theory of viscoelasticity, the exact relationship between relaxation modulus and creep compliance is given in Equation (2.10):

$$\int_0^t E(t-\tau) \frac{dD(\tau)}{d\tau} d\tau \quad (2.10)$$

Similar to relaxation modulus, the creep compliance can also be written in Prony series form as given in Equation (2.11):

$$D(t) = D_0 + \sum_{j=1}^n D_j \left(1 - e^{-\frac{t}{\tau_j}} \right) \quad (2.11)$$

If we substitute Equation (2.11), together with Equation (2.9) into Equation (2.10), after simplification and rearrangement, we can get a linear algebraic equation, Equation (2.12):

$$[A]\{D\} = [B] \quad (2.12)$$

where

$$[A] = \sum_{j=1}^M \left[\sum_{m=1}^N \frac{\rho_m E_m}{\rho_m - \tau_j} \left(e^{-\frac{t}{\rho_m}} - e^{-\frac{t}{\tau_j}} \right) + E_\infty \left(1 - e^{-\frac{t}{\tau_j}} \right) \right];$$

$$\{D\} = D_j; \text{ and}$$

$$[B] = 1 - \frac{1}{E_\infty + \sum_{m=1}^N E_m} \left(E_\infty + \sum_{m=1}^N E_m e^{-\frac{t}{\rho_m}} \right).$$

This equation can then be solved and the Prony coefficients D_j 's can be determined to find out the creep compliance.

2.5 Elastic-Viscoelastic Correspondence Principle

Schapery (1984) suggested that the constitutive equations for elastic media and viscoelastic media have identical forms, except that, for viscoelastic media, those stress and strain terms do not necessarily have any physical meanings. Instead, they are defined as pseudo variables in the form of convolution integrals. According to this correspondence principle, viscoelastic problems can be solved using elastic solutions when physical stress (or strain) is replaced by pseudo stress (strain). The formulation of pseudo strain is shown below as:

$$\varepsilon^R = \frac{1}{E_R} \int_0^t E(t-\tau) \frac{d\varepsilon}{d\tau} d\tau \quad (2.13)$$

where

ε^R = pseudo strain;

ε = actual strain;

E_R = reference modulus which is an arbitrary constant; and

$E(t)$ = relaxation modulus.

If we substitute Equation (2.13) into Equation (2.1), we will get

$$\sigma = E_R \varepsilon^R \quad (2.14)$$

It is very obvious that Equation (2.14) has a similar form as the Hooke's Law for elastic media, and a correspondence can be found between the elastic and viscoelastic stress-strain constitutive relationships.

Moreover, a very important implication of pseudo strain is that it is equal to the corresponding stress when we set $E_R = 1$. In other words, the value of pseudo strain equals to

the stress response of linear viscoelastic material due to a certain strain input. This important property can be easily visualized in the stress-pseudo strain plot for a monotonic tension test, as shown in Figure 2.5:

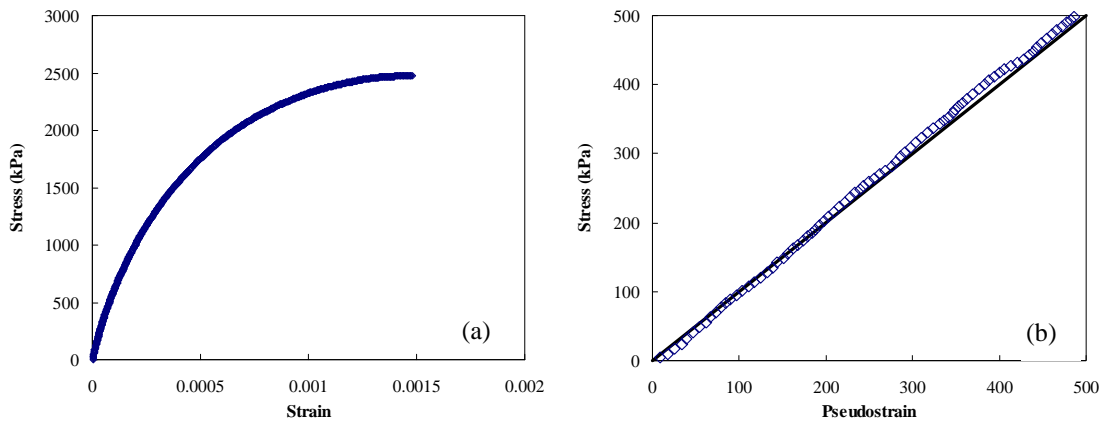


Figure 2.5 Typical test result from a constant crosshead rate tension test: (a) stress-strain plot; (b) stress-pseudo strain plot

In the stress-strain plot (Figure 2.5a), the nonlinear behavior starts at the onset of the test, which indicates damage occurs at that early stage. However, in fact, this nonlinearity is related to time effect only, which can be proved in the stress-pseudo strain plot, where the time effect is removed. The linear curve in Figure 2.5b suggests that no damage occurs at least until stress reaches 500 kPa.

2.6 Viscoelastic Continuum Damage Theory

Continuum damage theory ignores microscale behavior and characterizes material using macroscale observations. The two essential parameters that continuum damage theory tries to quantify are effective stiffness and damage. The effective stiffness, which represents the

material's structural integrity, can be easily assessed in the form of instantaneous secant modulus; while damage, on the hand, is difficult to quantify and generally relies on rigorous theories. One of the theories is the work potential theory developed by Schapery (1990) for elastic materials with growing damage based on the thermodynamics of irreversible process. In Schapery's theory, damage is quantified by an internal state variable (ISV) that accounts for microstructural changes in the material. By using the correspondence principle described in the previous Section 2.5, the work potential theory can then be extended to viscoelastic media. In summary, the viscoelastic continuum damage theory is composed of the following three basic equations:

1. Pseudo strain energy density function

$$W^R = f(\boldsymbol{\varepsilon}^R, S) \quad (2.15)$$

2. Stress-pseudo strain relationship

$$\boldsymbol{\sigma} = \frac{\partial W^R}{\partial \boldsymbol{\varepsilon}^R} \quad (2.16)$$

3. Damage evolution law

$$\frac{\partial S}{\partial t} = \left(-\frac{\partial W^R}{\partial S} \right)^\alpha \quad (2.17)$$

where

W^R = pseudo strain energy density;

$\boldsymbol{\varepsilon}^R$ = pseudo strain;

S = damage parameter (internal state variable); and

α = damage evolution rate.

Chapter 3 Specimen Preparation and Experimental Program

3.1 Materials

In this study, all the materials come from the NCDOT HWY-2007-7 MEPDG local calibration project, which are eleven different North Carolina local mixtures. The aggregates structures cover a wide range from 9.5 mm NMAS to 25 mm NMAS. The blended gradations are shown in Figure 3.1. The materials information (i.e. mix type, binder grade, binder & aggregate source, asphalt content) are listed in Table 3.1.

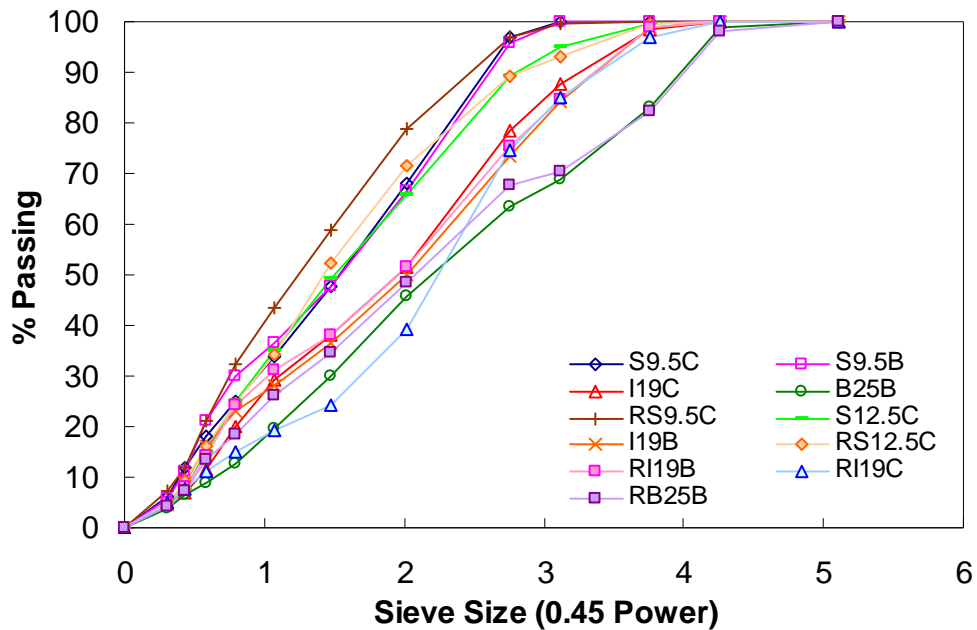


Figure 3.1 Mixture gradation chart

All the materials are acquired from the exact locations listed in Table 3.1. To verify if there is any difference between the actual gradation of acquired aggregates and that listed in the job mix formula (JMF), dry and wet sieve analysis are carried out on each stockpile of each mix. Also, the bulk specific gravity of aggregates is measured for each mix, and mix design verifications are carried out using optimum asphalt content and aggregate structure in the JMF before the start of specimen fabrication.

Table 3.1 Summary of the Eleven Most Popular Mixes in North Carolina

Mix Type	Binder	% AC	Binder Source	Aggregates Source
S9.5B	PG64-22	6.1	Associated Asphalt / Inman /SC #6	Vulcan - Morganton
S9.5C	PG70-22	5.2	Patriot Asphalt /Winston-Salem #21	Vulcan / N. - Winston Salem
RS9.5C	PG70-22	6.4	Citgo - Wilmington #31	Martin Marietta - Garner Rea Contractors - Garner
S12.5C	PG70-22	5.5	Citgo - Charlotte #11	Vulcan - Rockingham
I19.0B	PG64-22	4.8	Associated Asphalt / Inman /SC #6	Vulcan - Morganton
RI19.0B	PG64-22	4.4	Associated Asphalt / Inman /SC #6	Martin Marietta - Pomona
				Martin Marietta - Central Rock
				G.S Materials - Emery
				Blythe Construction - Greensboro
B25.0B	PG64-22	4.5	Associated Asphalt - Salisbury #12	Martin Marietta - Pomona
RB25.0B	PG64-22	4.2	Citgo - Wilmington #31	Martin Marietta - Garner
				S.T. Wooten Corp. - Clayton
RS12.5C	PG70-22	4.4	Citgo - Wilmington #31	Vulcan - Pineville
				Blythe Brothers - Charlotte
I19.0C	PG64-22	4.5	Citgo - Charlotte #11	Vulcan - Rockingham
				Rea Contractors - Graham
RI19.0C	PG64-22	4.3	Citgo - Wilmington #3	Vulcan - Pineville
				Blythe Construction - Pineville

3.2 Specimen Fabrication

All the specimens are compacted by Superpave gyratory compactor (SGC) to a diameter of 150 mm and a height of 178 mm. To obtain homogeneous specimen and at the same time fulfill the representative volume element (RVE) requirement, all the samples are cored and cut to a diameter of 75 mm and a height of 150 mm for testing. Before proceeding to testing, air void ratio is measured using the CoreLok method for each specimen. All the testing specimens used in this study have an air void ratio within the range of $5.5\pm 0.5\%$. To minimize the aging effect, specimens are sealed in plastic bag and stored carefully in the cabinet if they are not tested immediately after fabrication. No specimens are tested later than two weeks after they are cored and cut.

3.3 Test Set-up

All the specimens are glued to metal plates at both ends using epoxy, before they are set up in the machine for testing. Four loose core LVDTs are mounted around the side of specimen at an interval of 90 degree (Figure 3.2). The gauge length is 100 mm. MTS 810 closed loop servo-hydraulic machine is used for all the tests. For complex modulus tests, a 2 kip load cell is used, while for controlled crosshead cyclic tests, a 5 kip load cell is used. Test temperature is maintained by the environmental chamber, together with liquid nitrogen and a feedback system. During the tests, axial load, machine crosshead movement, and LVDT movement are recorded using National Instrument LabView software.



Figure 3.2 Test set-up

3.4 Test Methods

Two major types of tests are performed in this study: (1) complex modulus test; (2) controlled-crosshead cyclic test. Laboratory experiments are conducted according to the test protocols described below.

3.4.1 *Complex modulus test*

The tension-compression complex modulus tests are performed at five different temperatures (-10°, 5°, 20°, 40°, and 54°C) and six different frequencies (25, 10, 5, 1, 0.5, and 0.1 Hz). The testing order is from low to high temperatures and from high to low frequencies in order to minimize the damage to the specimens. A five-minute rest period is allowed between each

two adjacent different frequencies and at least two and half hours are waited after the testing temperature is changed for thermal equilibrium. The target strain level is within 50 to 70 microstrains. All tests are performed in stress-controlled mode according to AASHTO TP62-03. Complex modulus is obtained from the final six cycles of each loading series, i.e., when the material reaches steady state. Figure 3.3 shows the stress and strain history plot in a typical complex modulus test.

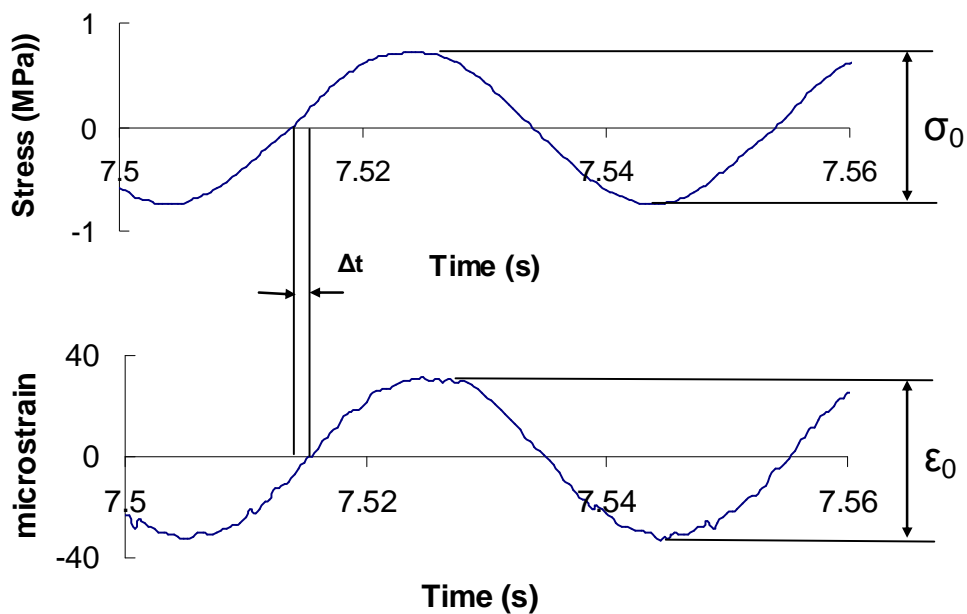


Figure 3.3 Stress and strain history plot in a typical tension-compression complex modulus test

The dynamic modulus and phase angle are calculated using Equation (3.1) and (3.2), respectively.

$$|E^*| = \frac{\sigma_0}{\epsilon_0} \quad (3.1)$$

where

σ_0 = steady state stress amplitude; and

ε_0 = steady state strain amplitude.

$$\phi = \Delta t \cdot 2\pi f \quad (3.2)$$

where

f = testing frequency.

3.4.2 *Controlled crosshead cyclic test*

Because a true controlled strain test using cylindrical specimens is difficult to run and can damage equipment if improperly performed, the controlled crosshead (CX) cyclic test is used for fatigue performance characterization, in which machine actuator's displacement is programmed to reach a constant peak level at each loading cycle. All the CX tests used in this study are conducted at a constant frequency of 10 Hz. Due to machine compliance issues, the actual on-specimen strain is significantly less than the programmed level, as shown in Figure 3.4a. Even though the on-specimen strains remain tensile, both tensile and compressive stresses are applied on the specimen, with a decreasing mean stress, as shown in Figure 3.4b.

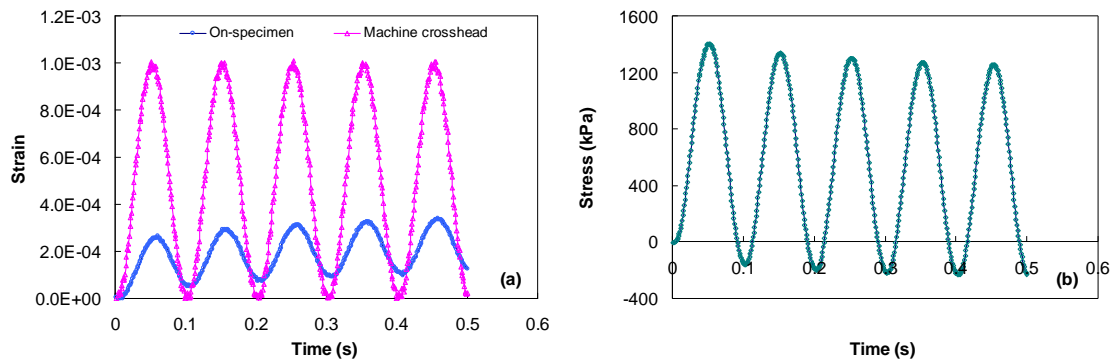


Figure 3.4 Strain and stress history for first five cycles of a typical CX test

This kind of test result in a mixed mode of loading that is neither controlled stress nor controlled strain. Christensen and Bonaquist (2005) have proposed systems that allow users to perform true controlled strain testing of cylindrical specimens. However, these researchers often do not allow the test to run to complete failure. In this study, the CX cyclic tests are performed to complete failure, and the failure criterion is discussed in the next section.

3.5 Failure Definition in Cyclic Test

In the CX cyclic test, dynamic modulus and phase angle are tracked throughout the entire fatigue life. Traditional fatigue analysis method determines failure as the point where the material's modulus drops to 50% of its initial value. However, this method is purely empirical, and a new approach suggested by Reese (1997) is used, whereby the cycle at which the phase angle shows a sharp decrease is defined as the number of cycle at failure (N_f). Figure 3.5 shows failure definition from a typical good CX cyclic test. This approach is strongly theoretically based, since it is believed that the drop of the phase angle is caused by macro crack localization, which is normally caused by the coalescence of micro cracks under

repeated cycles of loading. When macro cracks develop, all the work input is concentrated at the crack tip, the remaining body relaxes, and therefore the time dependence of the global stress-strain behavior reduces. This reduction in the time dependence causes the decrease in phase angle.

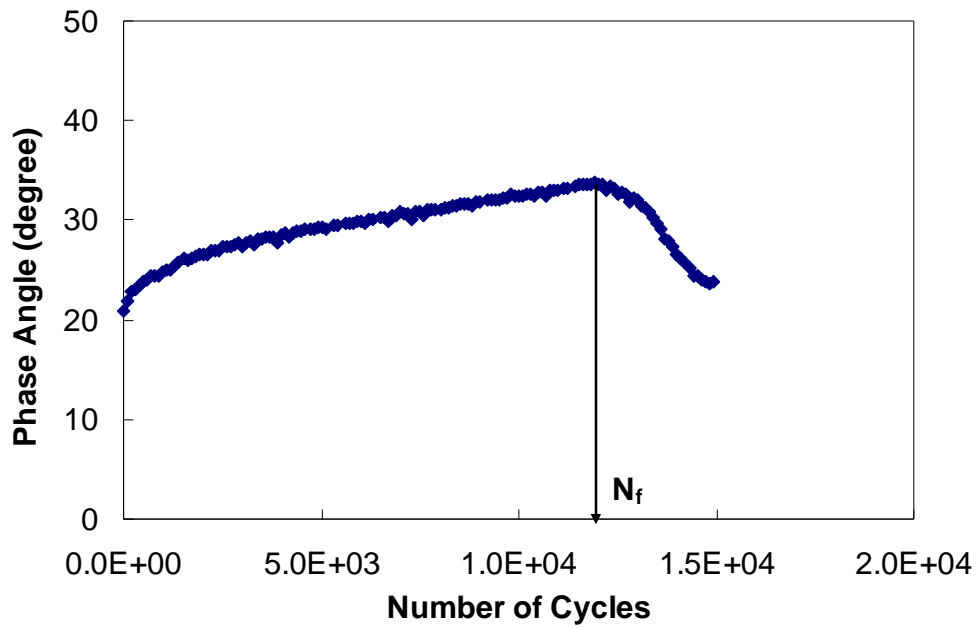


Figure 3.5 Fatigue life (N_f) definition of a typical good CX cyclic test

Chapter 4 Simplified VECD Model

4.1 Rigorous Modeling Approach

In the rigorous viscoelastic continuum damage modeling approach, material's effective stiffness is expressed as the secant modulus in stress-pseudo strain plot, Equation (4.1):

$$C = \frac{\sigma}{\varepsilon^R} \quad (4.1)$$

C is called pseudo stiffness, which is a function of damage S . For uniaxial mode of loading, the pseudo strain energy density function is given by Equation (4.2):

$$W^R = \frac{1}{2}(\varepsilon^R)^2 C \quad (4.2)$$

Because in Equation (4.2), only C is a function of damage S , when it is substituted into Equation (2.17), the damage evolution law becomes Equation (4.3):

$$\frac{\partial S}{\partial t} = \left(-\frac{1}{2}(\varepsilon^R)^2 \frac{\partial C}{\partial S} \right)^\alpha \quad (4.3)$$

Several different methods have been used by researchers to solve the above damage evolution law. The chain rule method proposed by Lee and Kim (1998) is used throughout the work presented in this thesis. This method utilizes the chain rule, Equation (4.4), by substituting it into Equation (4.3).

$$\frac{dC}{dS} = \frac{dC}{dt} \frac{dt}{dS} \quad (4.4)$$

After simplification, the damage calculation equation from this rigorous modeling approach is given in the Equation (4.5). Note that the time step term, Δt , is replaced by the reduced time interval, $\Delta \xi$, due to the verification of the time-temperature superposition principle with growing damage.

$$dS_i = \left(-\frac{1}{2} (\epsilon^R)_i^2 \Delta C_i \right)^{\frac{\alpha}{1+\alpha}} \cdot (\Delta \xi)_i^{\frac{1}{1+\alpha}} \quad (4.5)$$

This model is successfully applied to constant crosshead rate monotonic test data. However, if the rigorous approach is applied to cyclic data, then it requires the pseudo strain, pseudo stiffness, and damage to be calculated and tracked for the entire loading history. An average test with 30,000 cycles to failure and 100 data points per cycle (to gain good cycle pulse definition and avoid computational irregularities) would then require the analysis of 3,000,000 data points. Although this task is not impossible with modern computers, it is cumbersome even using advanced computational schemes. Further, experimental difficulties, such as data storage and electrical interference (noise and phase distortion), can lead to significant errors. The simplified VECD model used in this thesis is going to alleviate these shortcomings.

4.2 Simplified Modeling Approach

The simplified VECD model used in this research was developed by Underwood (2009). Before introducing the simplified modeling approach, a set of variable is defined based on the schematic view of controlled crosshead cyclic test, to distinguish from those used in monotonic test and rigorous approach. These variables are summarized in Figure 4.1.

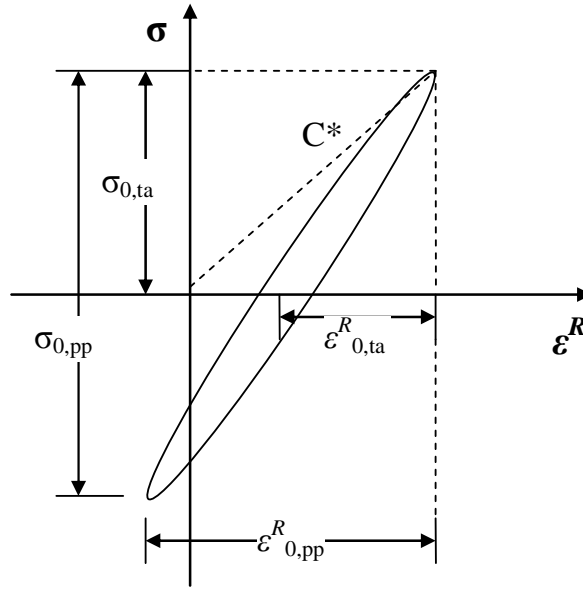


Figure 4.1 Schematic view of variables defined in simplified modeling approach for controlled crosshead cyclic test

As different from rigorous model, the pseudo stiffness term, C^* , used in cyclic test is a cyclic magnitude based value, which is equal to the ratio between tensile stress amplitude, $\sigma_{0,ta}$, and pseudo strain tension amplitude, $\varepsilon^R_{0,ta}$, for a given cycle, i . $\sigma_{0,pp}$ and $\varepsilon_{0,pp}$ stand for peak-to-peak stress and strain amplitude. These definitions will also affect the damage calculation, which will be introduced later in this chapter.

4.2.1 Defining Alpha

Through theoretical arguments that use the macrocracking phenomenon, the power, α , in the damage evolution law is found to relate to linear viscoelastic time dependence by Schapery (1990). Motivated by earlier work on this subject (Lee and Kim 1998a and b, Daniel and Kim 2002, Chehab et al. 2003, Underwood et al. 2006), here the maximum absolute value of the

log-log slope of the relaxation modulus, m , is taken to represent the linear viscoelastic response. According to Schapery's theory, if the material's fracture energy and failure stress are constant, then $\alpha = 1+1/m$, but if the fracture process zone size and fracture energy are constant, then $\alpha = 1/m$. Although different researchers have used differing α values, the general suggestion of Lee and Kim (1998a and b), which is that it is most appropriate to use $\alpha = 1+1/m$ for the CX tests, is adopted in this research. This approach is supported by the work of Daniel and Kim (2002) that uses the constant failure stress and energy criteria for the CX tests.

4.2.2 Identification of tensile loading time

Since crack growth is strongly related to tensile stress rather than compressive stress, it is critical to identify the actual time at which tensile loading starts and ends for a given cycle, as shown in Figure 4.2

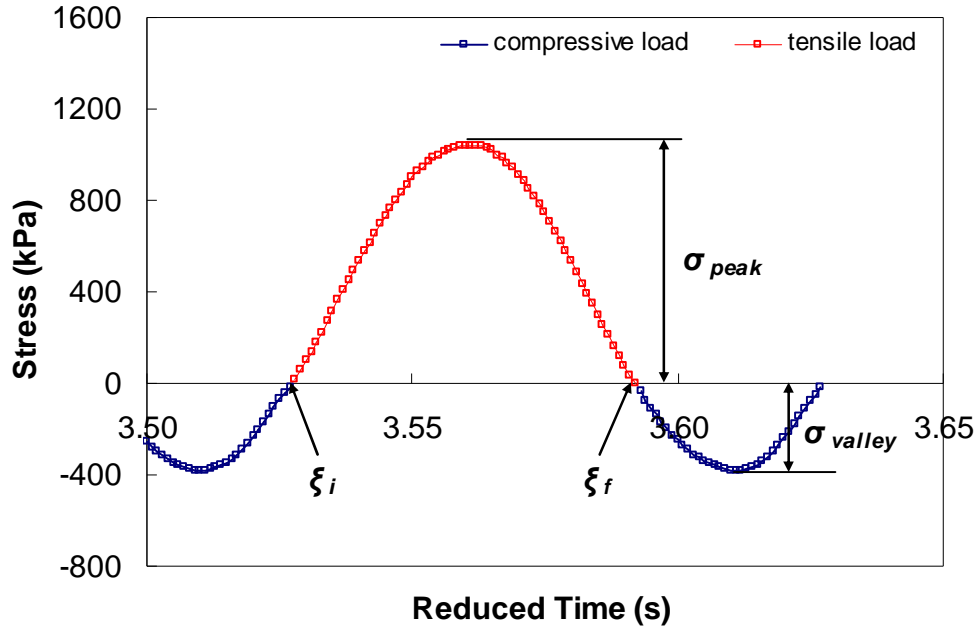


Figure 4.2 Loading history for a typical cycle during controlled crosshead cyclic test

In this research, the following analytical function, Equation (4.6), is used to describe the stress history for any given cycle.

$$\frac{\sigma(t)}{\sigma_{0,ia}} = (\beta - \cos(\omega t)) \frac{1}{\beta + 1} \quad (4.6)$$

where

ω = angular frequency; and

$$\beta_i = \frac{(\sigma_{peak})_i + (\sigma_{valley})_i}{|\sigma_{peak}|_i + |\sigma_{valley}|_i} \text{ for a given cycle } i.$$

When $\beta = 1$, the entire stress history for that given cycle is tensile; when $\beta = 0$, half of the stress history is under tensile loading; and when $\beta = -1$, the entire stress history is

compressive. As described before, in a general controlled-crosshead cyclic test, β value start from 1, then decrease and maintain around 0 as the number of loading cycle increases.

From Equation (4.6), the starting time of tensile load, ξ_i , and the end time, ξ_f , can be found for any given cycle, using the following two equations:

$$\xi_i = \frac{\pi}{\omega} - \frac{\pi - \cos^{-1}(\beta)}{\omega} \quad (4.7)$$

$$\xi_f = \frac{\pi}{\omega} + \frac{\pi - \cos^{-1}(\beta)}{\omega} \quad (4.8)$$

4.2.3 Simplification and adjustment factor

The simplification process starts with pseudo strain calculation. The rigorous approach solves the convolution integral, i.e., Equation (2.13), which provides a very accurate calculation of the pseudo strain magnitude and tracks any permanent pseudo strain during the test. However, this is not a practical way for cyclic test which can easily have over 10 million data points. A simplified calculation method is given by Equation (4.9), which helps save significant amount of computational time without introducing significant errors.

$$(\varepsilon_{0,ta}^R)_i = \frac{1}{E_R} \cdot \frac{\beta+1}{2} ((\varepsilon_{0,pp})_i \cdot E^* |_{LVE}) \quad (4.9)$$

The simplified approach used in this research assumes that Equation (4.10) can be used to simplify the more rigorous Equation (4.5) for damage calculation.

$$dS_i = \left(-\frac{1}{2} (\varepsilon_{0,ta}^R)_i^2 \Delta C_i^* \right)^{\frac{\alpha}{1+\alpha}} \cdot (\Delta \xi)_i^{\frac{1}{1+\alpha}} \cdot (K_1)^{\frac{1}{1+\alpha}} \quad (4.10)$$

As compared with Equation (4.5), Equation (4.10) replaces pseudo strain ε^R with pseudo strain tension amplitude $\varepsilon_{0,ta}^R$, pseudo stiffness C with cycle based value C^* , and time step $\Delta\xi$ with tensile loading time interval $\xi_i - \xi_f$. This simplified model implicitly assumes that pseudo strain is some constant value within a cycle. This flaw is corrected by adding an adjustment factor, K_I , which is a rigorously defined parameter dependent on the time history of loading, $f(\xi)$, only. For the assumption that the damage growth within an individual cycle is small, it can be shown that the factor K_I is given by Equation (4.11):

$$K_I = \frac{1}{\xi_f - \xi_i} \int_{\xi_i}^{\xi_f} (f(\xi))^{2\alpha} d\xi \quad (4.11)$$

Where $f(\xi)$ is the loading history function, which has the same formulation as Equation (4.6).

4.2.4 Specimen-to-specimen variability

In all the previous VECD model characterization process, the pseudo stiffness term is normalized for specimen-to-specimen variability by a factor, I , which is defined typically as the slope of stress-pseudo strain curve for a stress level up to 500 kPa. In this study, the dynamic modulus ratio (DMR) is used for all the normalization process, instead of I .

It is found that the damage curves collapse better when using DMR than I for all the North Carolina mixtures in this study, and the graphical comparisons are made in Appendix B.

To define DMR, firstly, the fingerprint test dynamic modulus value is computed using the final six cycles of the test, and denoted by $|E^*|_{test}$. Then, the LVE modulus for the particular temperature and frequency of that given fingerprint test is computed using the Prony coefficient function for the storage and loss moduli, as shown in Equations (4.12)-(4.14):

$$|E^*|_{LVE} = \sqrt{(E')^2 + (E'')^2} \quad (4.12)$$

where

$$E' = E_\infty + \sum_{i=1}^N \frac{E_i \rho_i^2 (2\pi f)^2}{\rho_i^2 (2\pi f)^2 + 1}; \quad \text{and} \quad (4.13)$$

$$E'' = \sum_{i=1}^N \frac{E_i \rho_i (2\pi f)}{\rho_i^2 (2\pi f)^2 + 1}. \quad (4.14)$$

After getting $|E^*|_{test}$ and $|E^*|_{LVE}$, DMR is computed as the ratio of these two numbers.

$$DMR = \frac{|E^*|_{test}}{|E^*|_{LVE}} \quad (4.15)$$

4.2.5 Model formulation

The simplified VECD model used in this study uses a combined approach, to take advantage of both rigorous approach and simplified approach. Within the model, it is suggested that pseudo strain should be calculated piecewise, whereby for the first loading path the rigorous calculation is used. This portion of the loading history is important because damage growth in this first loading path can be substantial. But for all other cycles, the simplified calculation is used, i.e., Equation (4.16). As a result of the piecewise definition of pseudo strain, the pseudo stiffness is also piecewise, as defined in Equation (4.17).

$$\varepsilon^R = \begin{cases} \varepsilon^R = \frac{1}{E_R} \int_0^\xi E(\xi - \tau) \frac{d\varepsilon}{d\tau} d\tau & \xi \leq \xi_p \\ (\varepsilon_{0,ta}^R)_{cycle\ i} = \frac{1}{E_R} \cdot \frac{\beta+1}{2} ((\varepsilon_{0,pp})_i \cdot |E^*|_{LVE}) & \xi > \xi_p \end{cases} \quad (4.16)$$

$$C = \begin{cases} C = \frac{\sigma}{\epsilon^R \cdot DMR} & \xi \leq \xi_p \\ C^* = \frac{\sigma_{0,ta}}{\epsilon_{0,ta}^R \cdot DMR} & \xi > \xi_p \end{cases} \quad (4.17)$$

For a similar reason and because significant damage can occur along the first loading path, the rigorous calculation shown in Equation (4.5) is used. After this time, however, the simplified calculation method is used. For lack of a clearer term, this portion of the damage calculation is referred to as the transient calculation and the remaining calculations as the cyclic calculations, i.e.,

$$dS = \begin{cases} (dS_{Transient})_{\text{timestep } j} = \left(-\frac{1}{2} (\epsilon^R)_j^2 \frac{\partial C}{\partial S} \right)^\alpha \cdot (d\xi)_j & \xi \leq \xi_p \\ (dS_{Cyclic})_{\text{cycle } i} = \left(-\frac{1}{2} (\epsilon_{0,ta}^R)_i^2 \frac{\partial C^*}{\partial S} \right)^\alpha \cdot (d\xi_p) \cdot (K_1) & \xi > \xi_p \end{cases} \quad (4.18)$$

Chapter 5 Test Results and Model Verification

5.1 Linear Viscoelastic Characterization

Three complex modulus tests are performed for each mix to obtain the linear viscoelastic properties. The results are then averaged to obtain a representative mastercurve for each mix. Figure 5.1 and Figure 5.2 show the average dynamic modulus mastercurves for all the eleven mixes plotted in semi-log and log-log scale, respectively. These figures suggest that, in general, surface mixes have low stiffness values, whereas intermediate mixes and base mixes show relatively high stiffness values. Also it can be seen that the dynamic moduli of the RAP mixes are higher than those of the non-RAP mixes, except for RB25B mix. Figure 5.3 and Figure 5.4 show the phase angle and shift factor test results, respectively, for all the eleven mixes.

The relaxation modulus and creep compliance are calculated from the complex modulus using linear viscoelastic theory. The slope of the dynamic modulus mastercurve in log-log space, m , is another important property, which is directly related to the damage evolution rate, α , in continuum damage model. These properties are further used for modeling work presented in the next section.

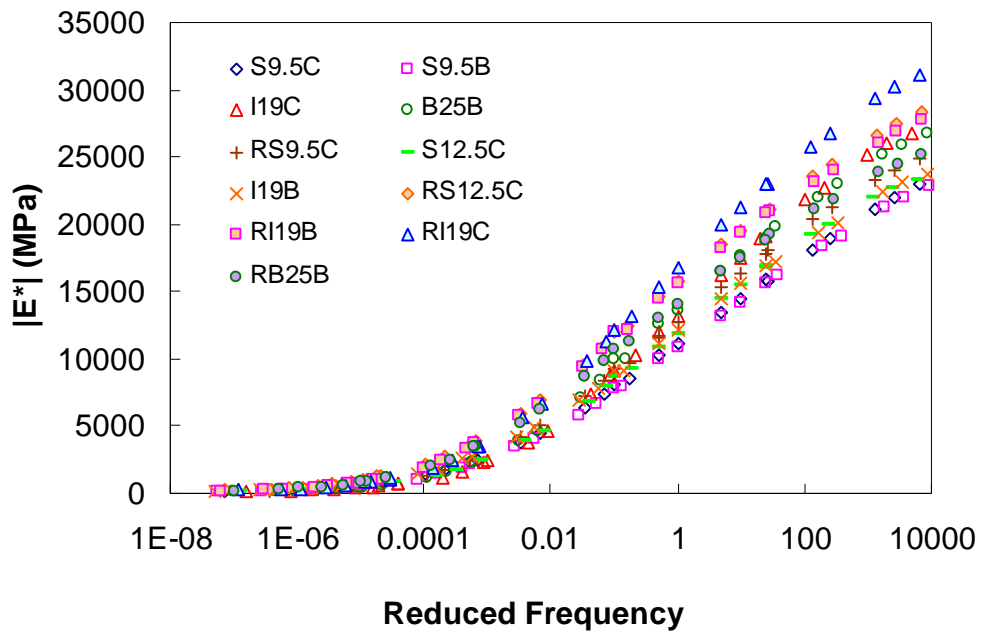


Figure 5.1 Average dynamic modulus mastercurves for all mixes (semi-log)

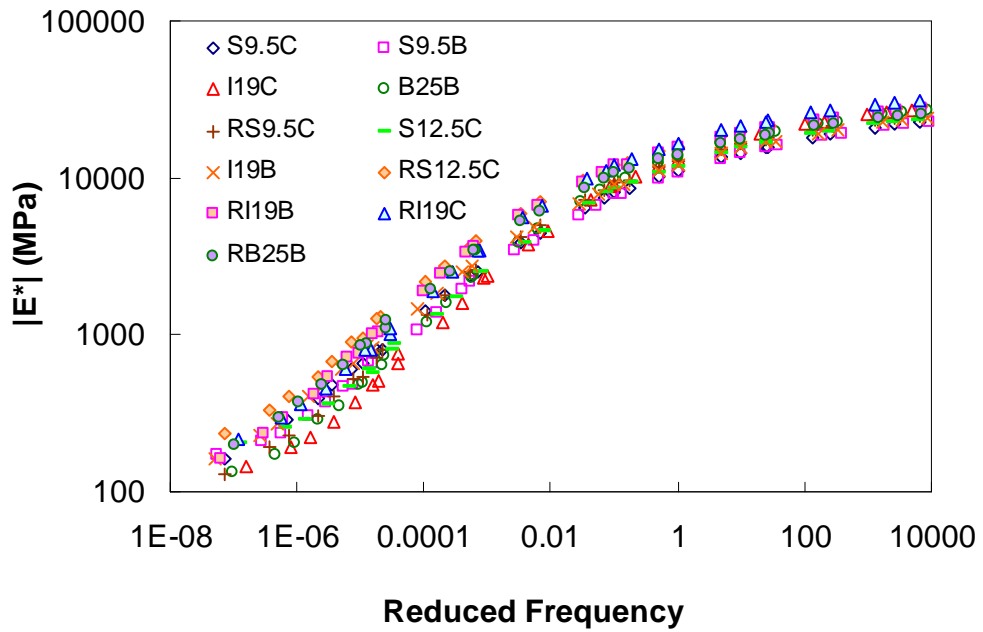


Figure 5.2 Average dynamic modulus mastercurves for all mixes (log-log)

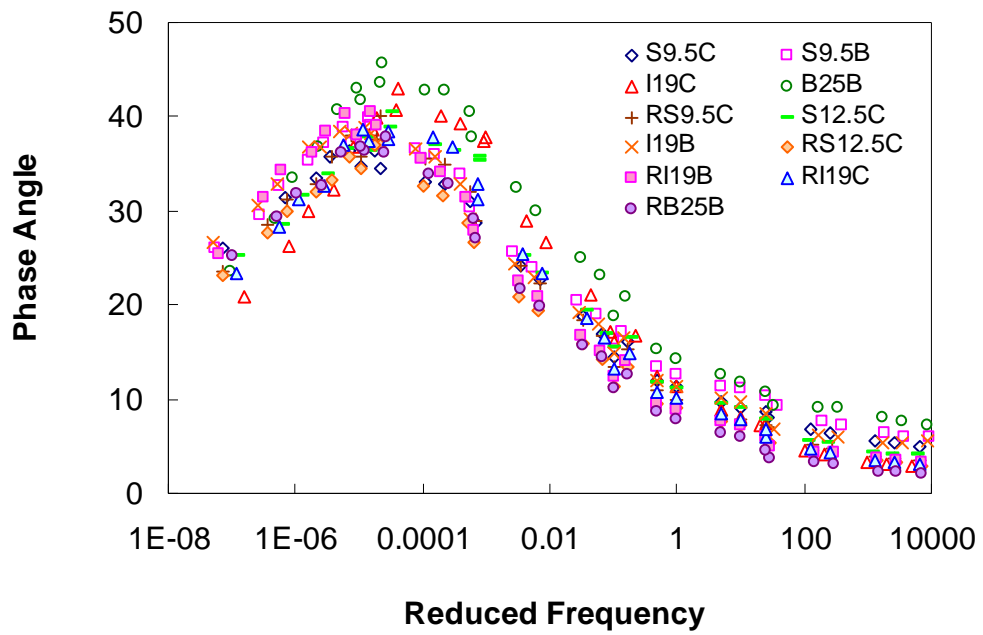


Figure 5.3 Average phase angle mastercurves for all mixes (semi-log)

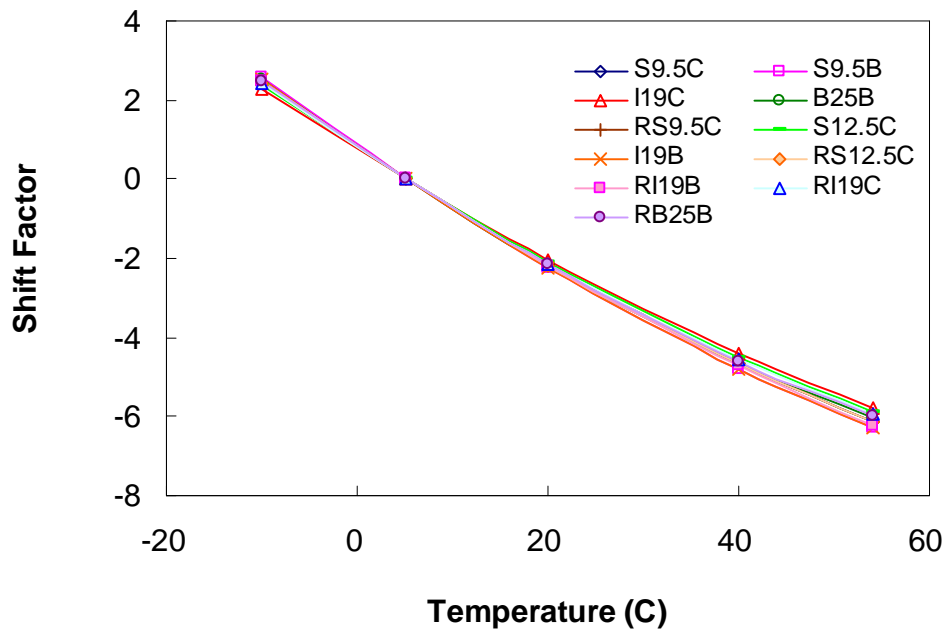


Figure 5.4 Shift factor functions for all mixes

5.2 Viscoelastic Damage Characterization

The viscoelastic damage characterizations are done by performing controlled-crosshead cyclic tests at different strain levels and different temperature conditions. The choices of crosshead strain magnitude are made based on experimental experiences, since the relationship between machine crosshead strain and actual on-specimen strain can vary with mix type and temperature. A proper determination of crosshead strain is very important, because it directly affects the on-specimen strain level and thus the fatigue life of the specimen.

Among the total eleven mixes, the S9.5C mix is chosen to be used for simplified VECD model development purpose, because of its fine graded nature and thus low testing variability. For this particular purpose, a total number of sixteen tests are performed on this mix. After the model is developed, it is verified by four other additional mixes, which cover a wide range of mix type. The four verification mixes used in this study are S9.5B, I19C, B25B and RS9.5C mixes. For each of these four mixes, six cyclic tests are performed at two different strain levels and three different temperatures. Once the model is verified, for the remaining mixes, it is no longer necessary to perform fatigue tests at so many different conditions as that for the first five mixes. Instead, only two different strain level fatigue tests (one at high level and the other at low level) are performed at a single temperature (19°C), and the fatigue behavior from other temperatures and strain levels are predicted using the simplified VECD model. Table 5.1 summarizes the cyclic test results for all the mixes used in this study. As

mentioned in Chapter 3, all tests are performed at a constant frequency of 10 Hz, and failure is defined as the point at which the phase angle starts to drop.

Table 5.1 Summary of controlled-crosshead cyclic test results

Material	Specimen Name	Crosshead Strain (me)	Test Designation	Initial Strain ^a (me)	Freq. (Hz)	Temperature (C)	N _f
S9.5C	S9.5C-28	1500	27-CX-VH	668	10	26.80	1600
	S9.5C-29	1500	27-CX-VH (2)	638	10	26.80	420
	S9.5C-30	1000	27-CX-H	437	10	26.80	17500
	S9.5C-31	750	27-CX-L	303	10	26.60	86100
	S9.5C-37	1200	27-CX-H2	520	10	26.95	780
	S9.5C-38	600	27-CX-VL2	247	10	26.80	165000
	S9.5C-43	550	27-CX-VL	225	10	27.40	190000
	S9.5C-13	1000	19-CX-H	240	10	19.05	45000
	S9.5C-14	750	19-CX-VL	190	10	19.00	311000
	S9.5C-22	1600	19-CX-VH	402	10	18.50	2280
	S9.5C-39	1500	19-CX-H3	425	10	18.70	3780
	S9.5C-40	1200	19-CX-H2	332	10	18.80	12100
	S9.5C-26	1100	5-CX-H	150	10	5.00	70000
	S9.5C-27	1000	5-CX-L	126	10	4.90	140000
	S9.5C-41	1400	5-CX-VH	213	10	4.60	1430
S9.5C-42	1200	5-CX-H2	189	10	5.30	1100	
S9.5B	S9.5B-4	950	27-CX-H	500	10	27.40	12100
	S9.5B-5	1200	19-CX-H	363	10	19.20	4570
	S9.5B-6	850	19-CX-L	266	10	19.30	47000
	S9.5B-7	750	27-CX-L	353	10	27.30	87900
	S9.5B-8	1150	5-CX-H	200	10	5.50	4600
	S9.5B-9	950	5-CX-L	166	10	5.50	198000
I19C	I19C-4	1000	19-CX-H	252	10	19.15	6500
	I19C-6	700	27-CX-H	264	10	27.40	19900
	I19C-7	550	27-CX-L	236	10	27.40	217000
	I19C-8	800	5-CX-VL-not fail	106	10	5.40	>277200 ^b
	I19C-9	700	19-CX-L	232	10	19.50	27000
	I19C-10	950	5-CX-H	133	10	5.15	16600

Table 5.1 Continued

Material	Specimen Name	Crosshead Strain (me)	Test Designation	Initial Strain ^a (me)	Freq. (Hz)	Temperature (C)	N _f
B25B	B25B-5	1000	19-CX-H	240	10	19.10	4780
	B25B-11	730	19-CX-L	186	10	19.10	7160
	B25B-14	1000	5-CX-H	122	10	5.40	11000
	B25B-18	725	5-CX-L	112	10	5.15	73800
	B25B-20	400	27-CX-L	162	10	27.50	75000
	B25B-22	500	27-CX-H	256	10	27.40	11000
RS9.5C	RS9.5C-5	1100	19-CX-H	287	10	19.40	44000
	RS9.5C-6	950	19-CX-L	232	10	19.60	148000
	RS9.5C-7	900	27-CX-H	355	10	27.30	27500
	RS9.5C-8	1100	5-CX-VL-not fail	155	10	5.15	>168000 ^b
	RS9.5C-9	800	27-CX-L	318	10	27.35	79000
	RS9.5C-10	1200	5-CX-H	174	10	5.35	41000
S12.5C	S12.5C-4	1150	19-CX-H	312	10	19.20	1250
	S12.5C-5	750	19-CX-L	192	10	19.20	74100
I19B	I19B-5	1000	19-CX-H	306	10	19.00	800
	I19B-6	650	19-CX-L	181	10	19.20	19000
RS12.5C	RS12.5C-4	900	19-CX-H	186	10	19.10	9330
	RS12.5C-5	750	19-CX-L	156	10	19.00	220000
RI19B	RI19B-4	900	19-CX-H	187	10	19.45	6000
	RI19B-5	650	19-CX-L	141	10	19.50	23700
RI19C	RI19C-4	900	19-CX-H	180	10	19.35	3450
	RI19C-6	700	19-CX-L	122	10	19.20	68900
RB25B	RB25B-4	700	19-CX-H	175	10	19.20	950
	RB25B-7	600	19-CX-L	133	10	19.20	7550

^a On-specimen strain at the 50th loading cycle

^b Test stopped at that number of loading cycle and specimen didn't fail

After each fatigue test, the pseudo stiffness (C^*) and damage (S) are computed according to the method proposed in Section 4.2.5. Figure 5.5 shows the damage curves (C^* versus S) for the S9.5C, S9.5B, I19C, B25B, and RS9.5C mixes. As mentioned before, these five mixes

are used for model development and verification, which require a large amount of tests at various testing conditions.

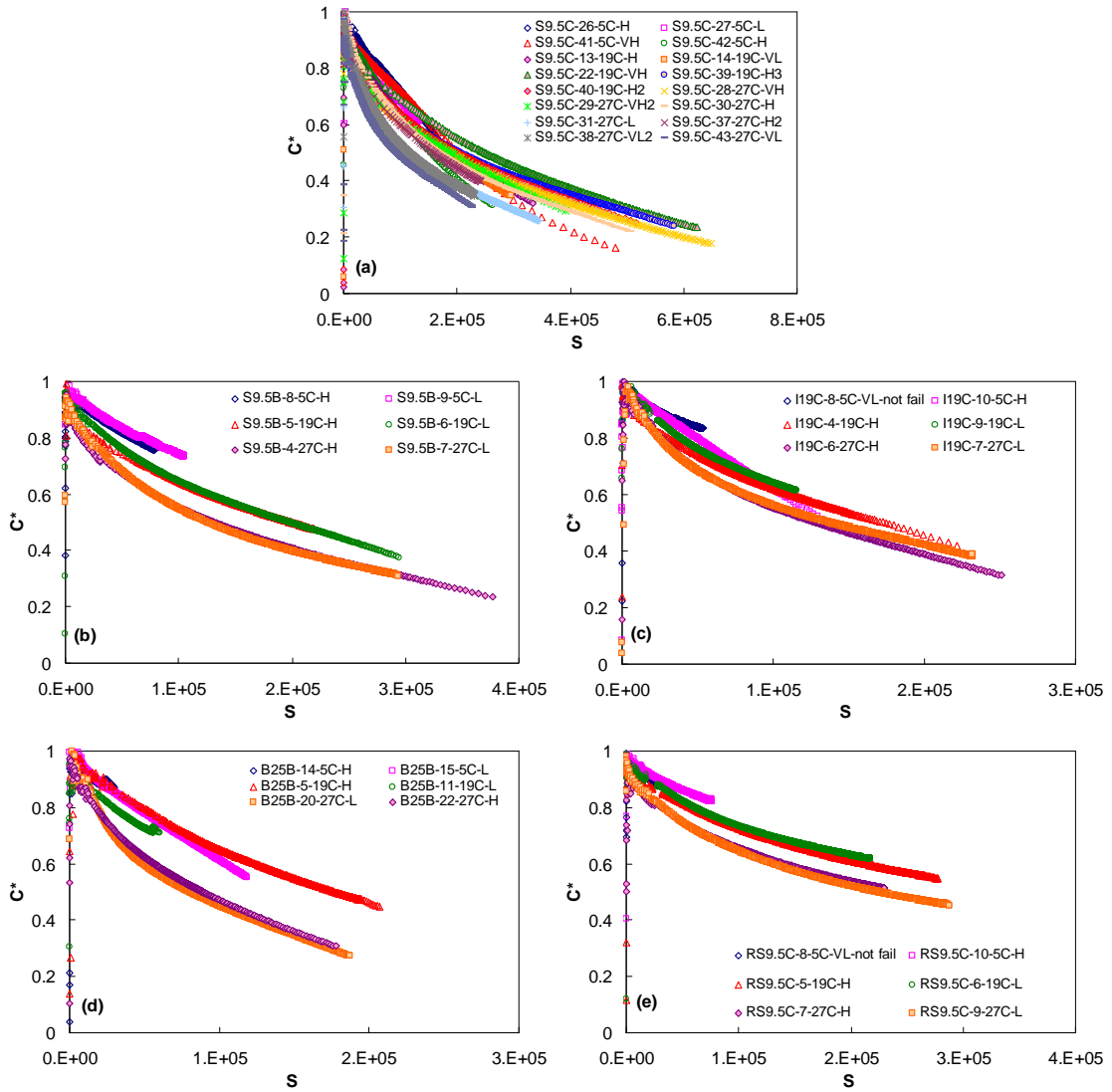


Figure 5.5 Damage curves for (a) S9.5C; (b) S9.5B; (c) I19C; (d) B25B; (e) RS9.5C mix.

The results in Figure 5.5 show that most of the 5°C and 19°C curves collapse well within each mix, except the S9.5B mix, for which the 5°C curves stay above the 19°C ones. And in general, the 5°C curves are relatively shorter which is caused by the brittle behavior of material at low temperature. Another observation from the above graphs is that all the 27°C curves stay at the bottom. This phenomenon is consistent with those observed in low strain rate or high temperature monotonic tests by other researchers, which can be explained by viscoplasticity. Due to these reasons, the intermediate temperature, 19°C, is chosen as the testing temperature for the remaining mixes after the model has been verified. It is believed that 19°C is a suitable temperature for material's viscoelastic damage characterization whereas the material is not as brittle as at low temperature and meanwhile the effect of viscoplasticity is negligible. Figure 5.6 shows the damage curves for the other six mixes, i.e., S12.5C, I19B, RS12.5C, RI19B, RI19C, and RB25B.

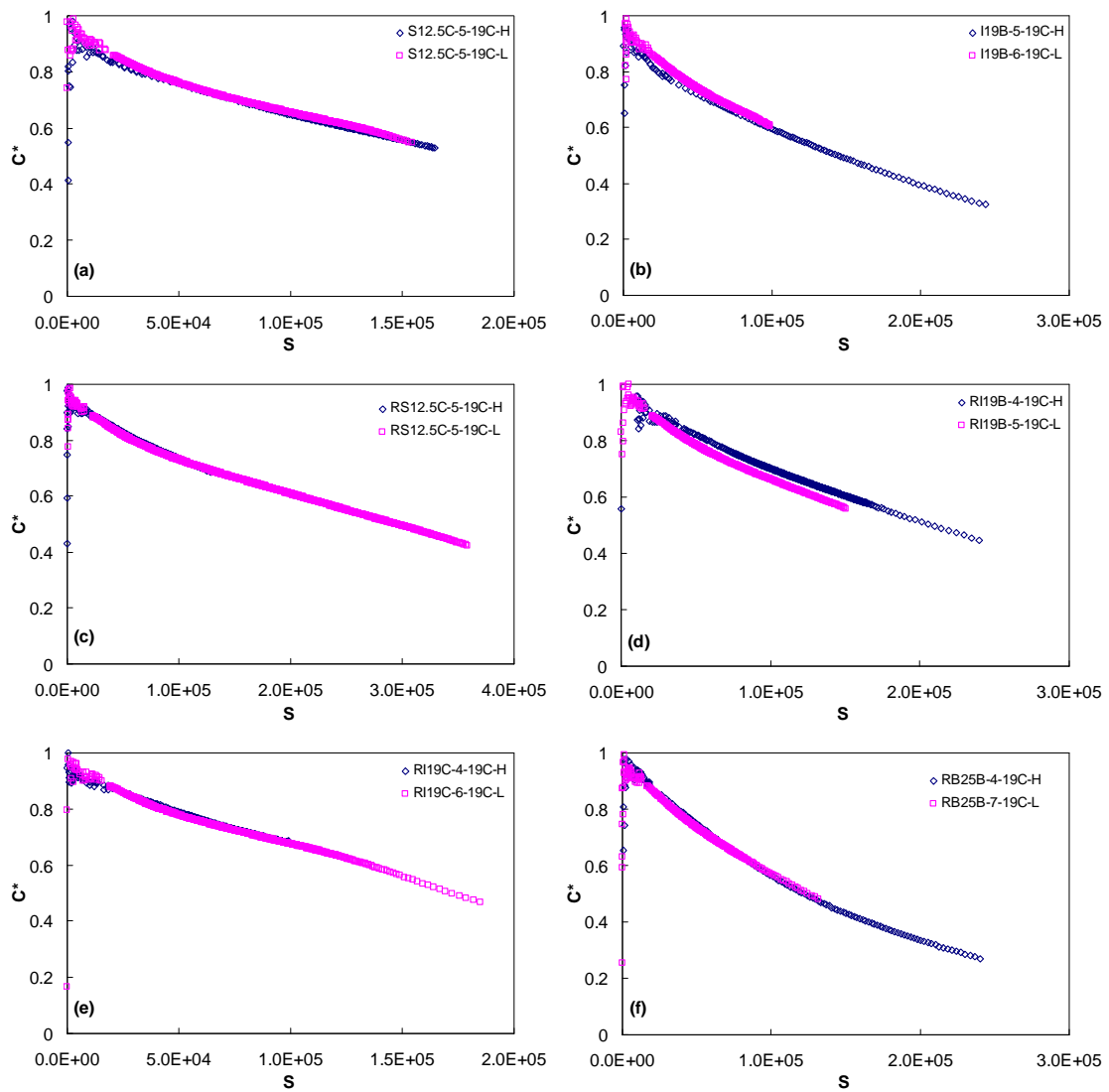


Figure 5.6 Damage curves for (a) S12.5C; (b) I19B; (c) RS12.5C; (d) RI19B; (e) RI19C; (f) RB25B mix.

These graphs show that, for all the mixes, the two curves, obtained from two distinct cyclic tests (one at a low strain level and the other at a high strain level), collapse very well.

It should be noted that there are two types of failure patterns (mid-failure and end-failure) of all the CX tests used in this study as illustrated in Figure 5.7.

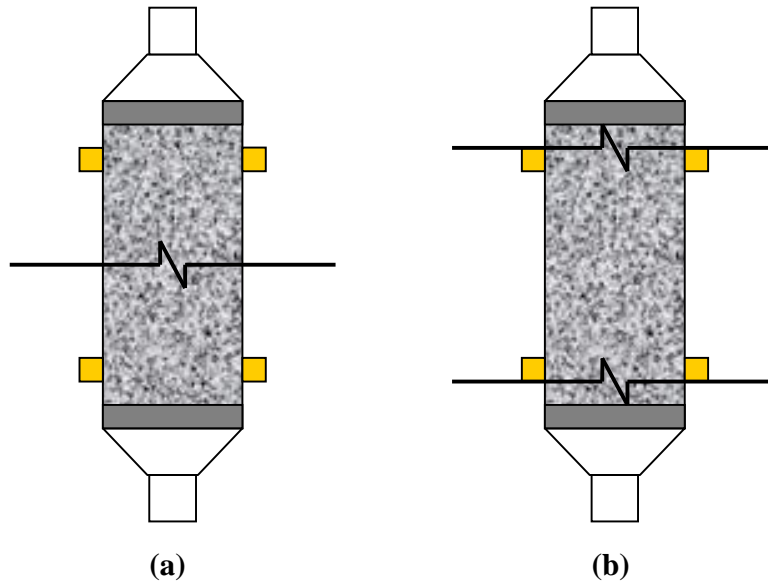


Figure 5.7 Failure locations of CX cyclic tests: (a) mid-failure; (b) end-failure

Mid-failure tests are considered as good tests, because the LVDTs are able to capture the major damage throughout the entire test. End-failure tests are not as good as the mid-failure, since macrocrack localizes beyond the experimental measurement range. For this reason, material's stiffness cannot be calculated accurately, at least, at the late stage of the test. The failure locations of all the CX cyclic tests are summarized in Table 5.2.

Table 5.2 Summary of failure locations for all CX cyclic tests

Specimen Name	Failure Location	Specimen Name	Failure Location	Specimen Name	Failure Location
S9.5C-28	middle	S9.5B-5	end	RS9.5C-6	end
S9.5C-29	middle	S9.5B-6	middle	RS9.5C-7	end
S9.5C-30	middle	S9.5B-7	middle	RS9.5C-9	end
S9.5C-31	middle	S9.5B-8	end	RS9.5C-10	end
S9.5C-37	middle	S9.5B-9	end	S12.5C-4	end
S9.5C-38	end	I19C-4	middle	S12.5C-5	end
S9.5C-43	middle	I19C-6	middle	I19B-5	middle
S9.5C-13	middle	I19C-7	end	I19B-6	end
S9.5C-14	middle	I19C-9	end	RS12.5C-4	end
S9.5C-22	middle	I19C-10	middle	RS12.5C-5	middle
S9.5C-39	middle	B25B-5	end	RI19B-4	middle
S9.5C-40	middle	B25B-11	end	RI19B-5	middle
S9.5C-26	middle	B25B-14	end	RI19C-4	end
S9.5C-27	middle	B25B-18	middle	RI19C-6	middle
S9.5C-41	middle	B25B-20	middle	RB25B-4	middle
S9.5C-42	middle	B25B-22	middle	RB25B-7	middle
S9.5B-4	middle	RS9.5C-5	end		

For damage characterization purpose, end-failure test results are still considered as valid, and this conclusion is substantiated by Figure 5.8 that shows 19°C damage curves generated from both mid-failure and end-failure tests for several different mixes. It is observed from these graphs that end-failure test has a shorter damage curve than the mid-failure one; in other words, the end-failure test has a higher measured pseudo stiffness value at failure. This can be explained by the macrocrack localization phenomenon as stated earlier in this section. However, this does not affect the damage characterization, as the end-failure (short) curves follow the trend of mid-failure (long) curves very well. Thus, it is proved that the material's

damage curve can be characterized by uniaxial CX cyclic tests, regardless of their failure locations.

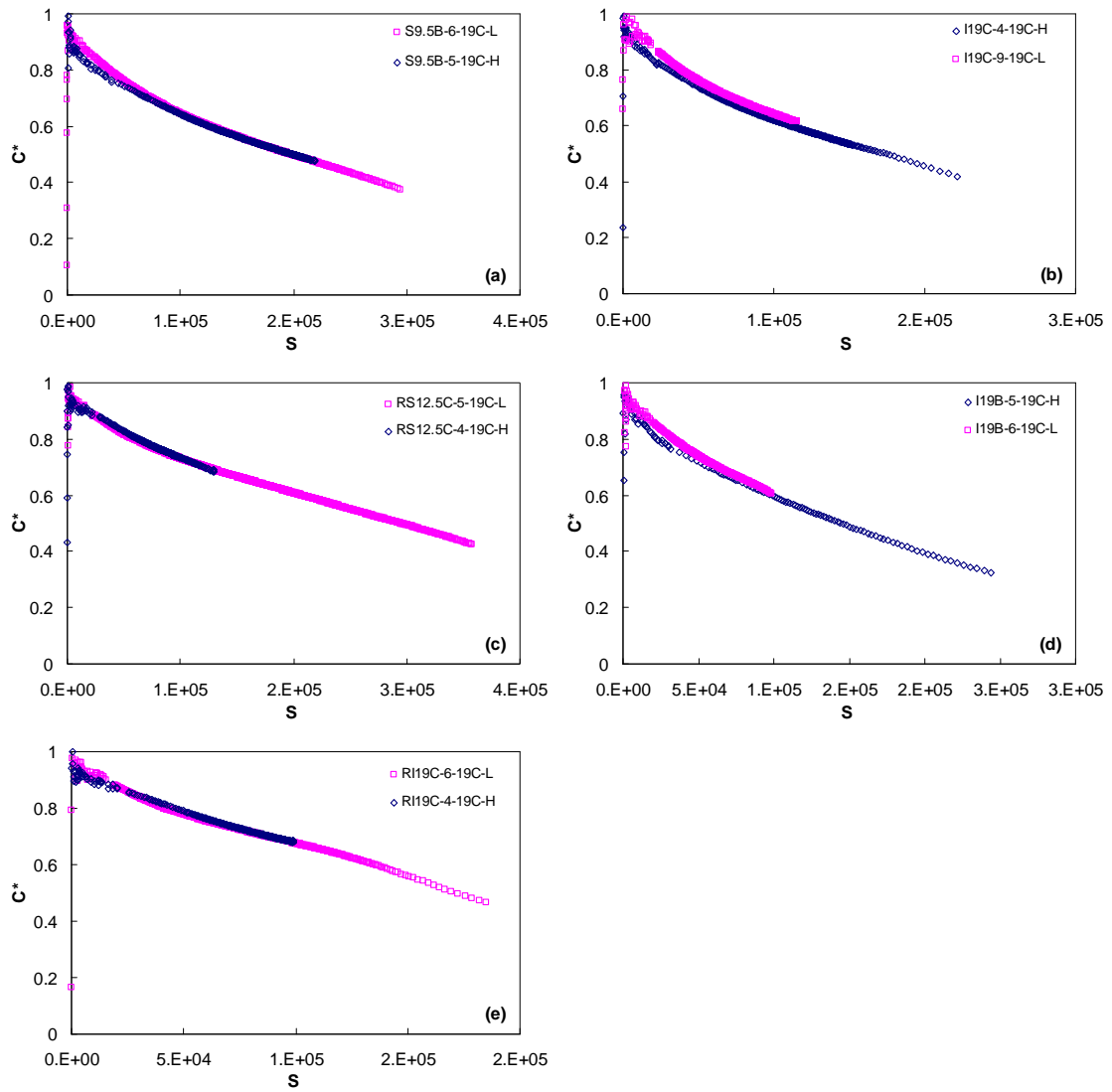


Figure 5.8 Damage curves for CX cyclic tests with different failure locations: (a) S9.5B; (b) I19C; (c) RS12.5C; (d) I19B; (e) RI19C.

All the 19°C test curves are fitted to analytical forms to obtain the damage characteristic curves for each mix, which will be used for predicting fatigue performance. The power law function (Equation (5.1)) suggested by Lee and Kim (1998) is found to fit the experimental results better than the exponential function (Equation (5.2)) used by Underwood (2005). The fitted damage characteristic curves for all eleven mixes are shown in a single graph as Figure 5.9.

$$C^* = 1 - C_{11} S^{C_{12}} \quad (5.1)$$

$$C^* = e^{aS^b} \quad (5.2)$$

The damage characteristic curves for all eleven mixtures are plotted together in Figure 5.9. It depicts mixture's resistance to damage. However, it is impossible to compare mixtures' fatigue performances by simply looking at the damage characteristic curves. Such comparison can be achieved by fatigue test simulation which will be discussed in Chapter 6.

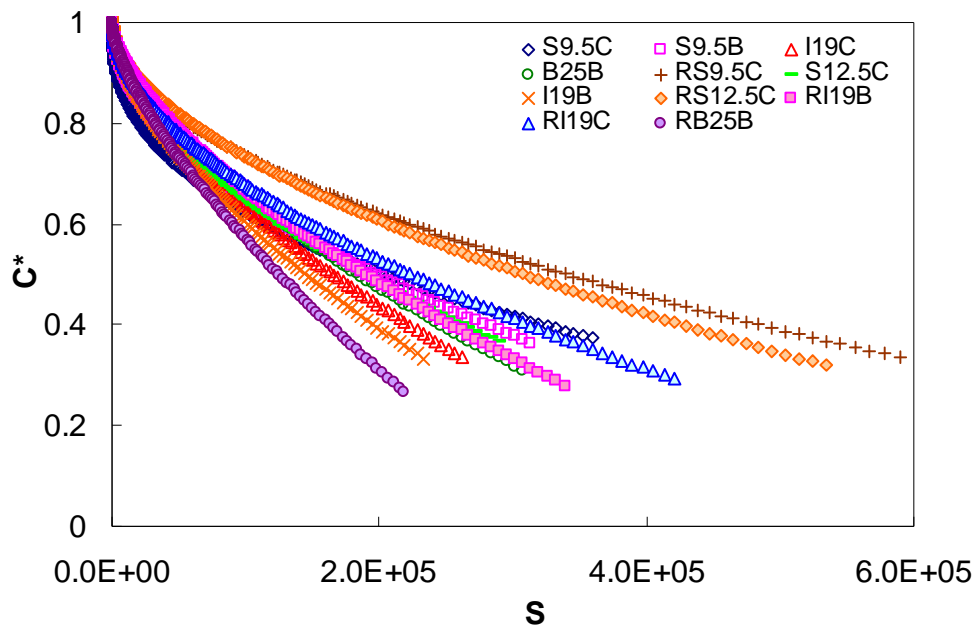


Figure 5.9 Damage characteristic curves for all mixtures

Chapter 6 Model Application

6.1 Simulation Failure Envelope

The simplified fatigue model does not account for changing time dependency and, therefore, it is not possible to observe a sudden decrease of the phase angle in simulation, which is used to define failure in the measured tests. For this reason, an empirical observation of all the tested mixtures is used to determine the failure criterion. The observation is shown in Figure 6.1 where the pseudo stiffness at failure is plotted against test reduced frequency for multiple mixtures. Note that only mid-failure test results are used here, since the measured stiffness values are not reliable for end-failure tests as explained in the previous chapter.

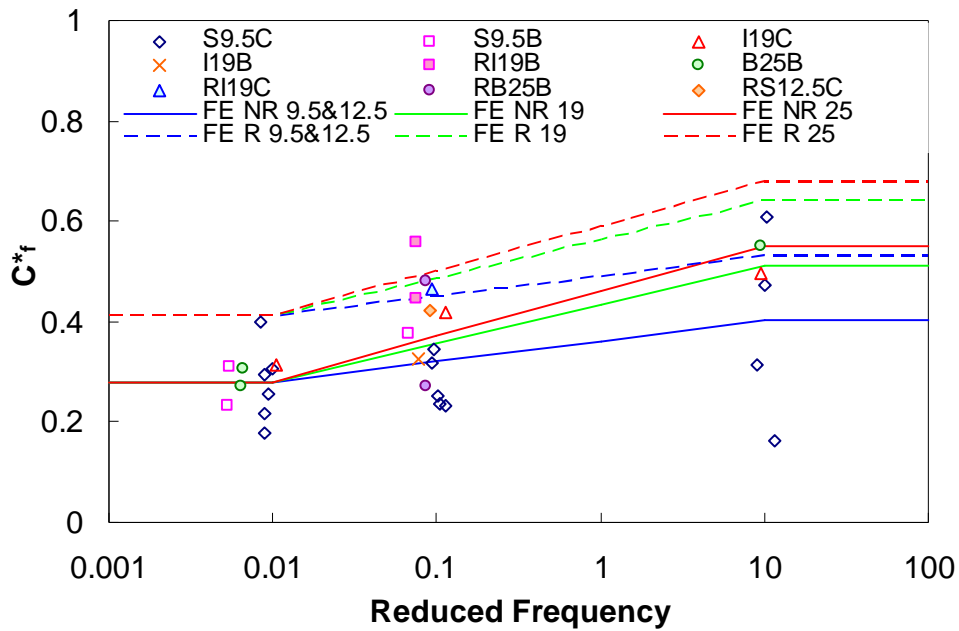


Figure 6.1 Failure envelope for fatigue test simulation

It is found from Figure 6.1 that the pseudo stiffness at failure increases with the reduced frequency. For non-RAP mixtures, when the reduced frequency is below 0.01 which corresponds to approximately 27°C at 10 Hz, failure for the cyclic tests occurs at a pseudo stiffness of approximately 0.28, a value similar to that observed by Daniel and Kim (2002) for their tests, which were performed at 25°C. As the reduced frequency increases, failure tends to occur at a higher level of pseudo stiffness. It is also observed that the rate of this increment is aggregate size dependent; that is, as N_{MAS} increases, the rate of change in the pseudo stiffness at failure as a function of reduced frequency increases. Further, from the data around a reduced frequency of 0.1, it is found RAP mixtures have a higher failure pseudo stiffness value than non-RAP mixtures. So in summary, a piecewise fitting function

given in Equation (6.1) is applied for failure criterion development. Note that because calibration data are not available when reduced frequency is greater than 10 or less than 0.01, it is assumed that the failure pseudo stiffness neither increases nor decreases beyond this range. The failure envelope within this range is a linear function in semi-log space, whereas the slope is a function of NMAS and the intercept is affected by the inclusion of RAP in mixture. The coefficients of the fitting function are listed in Table 6.1.

$$C_f^* = \begin{cases} a \cdot \log(0.01) + b & f_R \leq 0.01 \\ a \cdot \log(f_R) + b & 0.01 < f_R < 10 \\ a \cdot \log(10) + b & f_R \geq 10 \end{cases} \quad (6.1)$$

where

f_R = reduced frequency; and

a and b = coefficients.

Table 6.1 Coefficients for failure envelope

	NMAS	a	b
Non-RAP	9.5&12.5	0.040538	0.361945
	19	0.076546	0.433962
	25	0.090027	0.460924
RAP	9.5&12.5	0.040538	0.490049
	19	0.076546	0.562066
	25	0.090027	0.589027

6.2 Fatigue Test Prediction

Once the simplified VECD model is calibrated, i.e., C_{11} and C_{12} coefficients in Equation (5.1) are found for each mix, the analytical function of damage characteristic curve can be substituted into Equation (4.18) for simulation purpose. So the amount of damage can be

calculated for a known pseudo strain history by assuming an initial damage value, e.g., 0.1.

The predicted damage for a prescribed pseudo strain history is then as follows:

$$S_{i+1} = S_i + \left(\frac{1}{2} (\epsilon_{0,ta}^R)^2 C_{11} C_{12} S^{C_{12}-1} \right)^\alpha K_1 (d\xi) \quad (6.2)$$

The corresponding pseudo stiffness history can then be predicted if the damage history is determined according to Equation (5.1). The predicted and measured pseudo stiffness values for a typical good prediction are shown in Figure 6.2, and results from a typical bad prediction are shown in Figure 6.3. Finally, by applying the failure criterion developed in the previous section, the fatigue life can be predicted for that particular cyclic test with a known pseudo strain history. By comparing the measured and predicted fatigue test results in strain versus fatigue life plots (Figure 6.4 and Figure 6.5), it can be seen that the model does a reasonable job of predicting the failure performance at all temperatures.

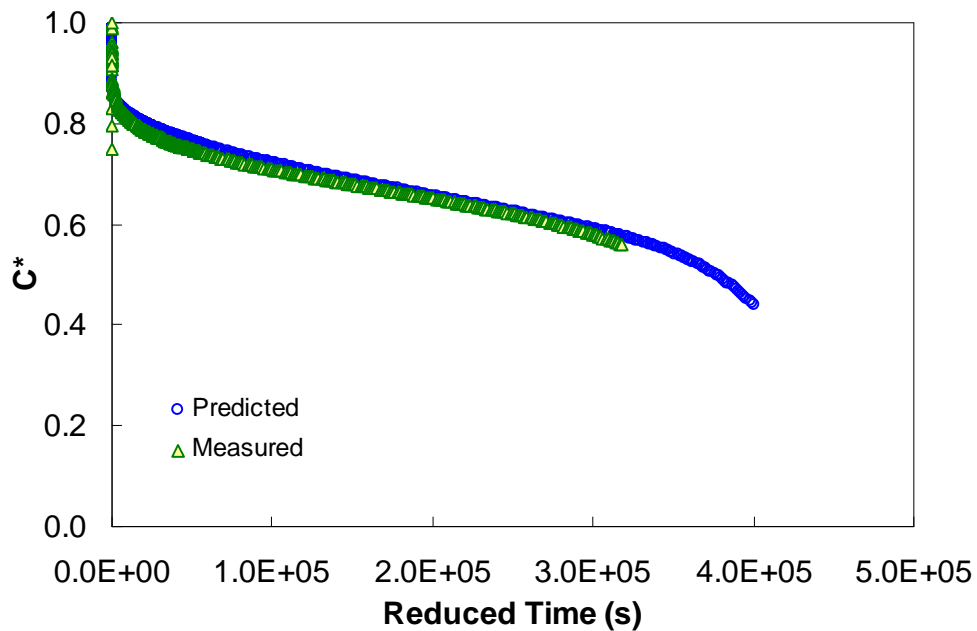


Figure 6.2 Typical good pseudo stiffness prediction (RI19B-5)

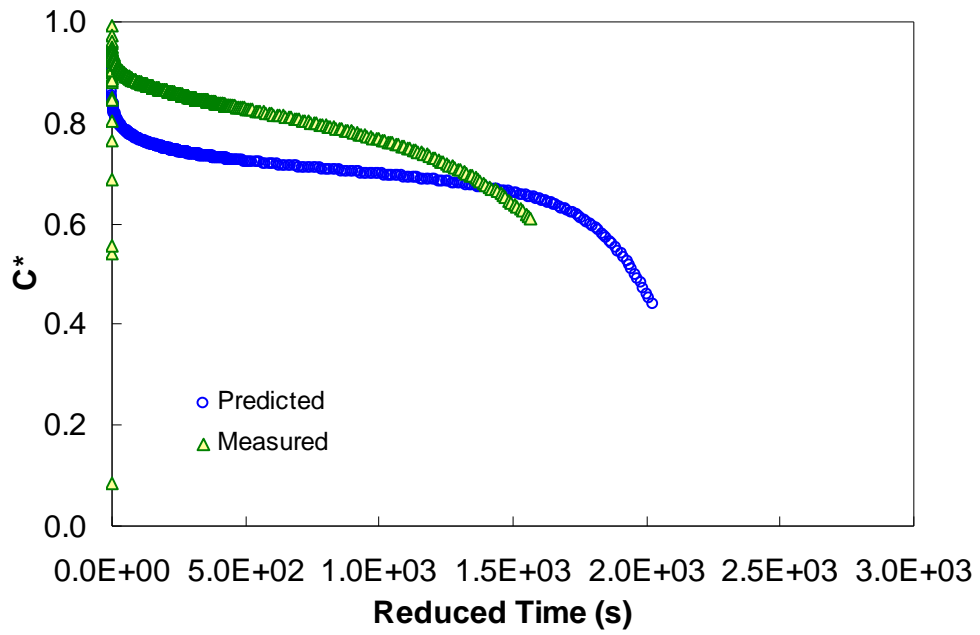


Figure 6.3 Typical bad pseudo stiffness prediction (I19C-10)

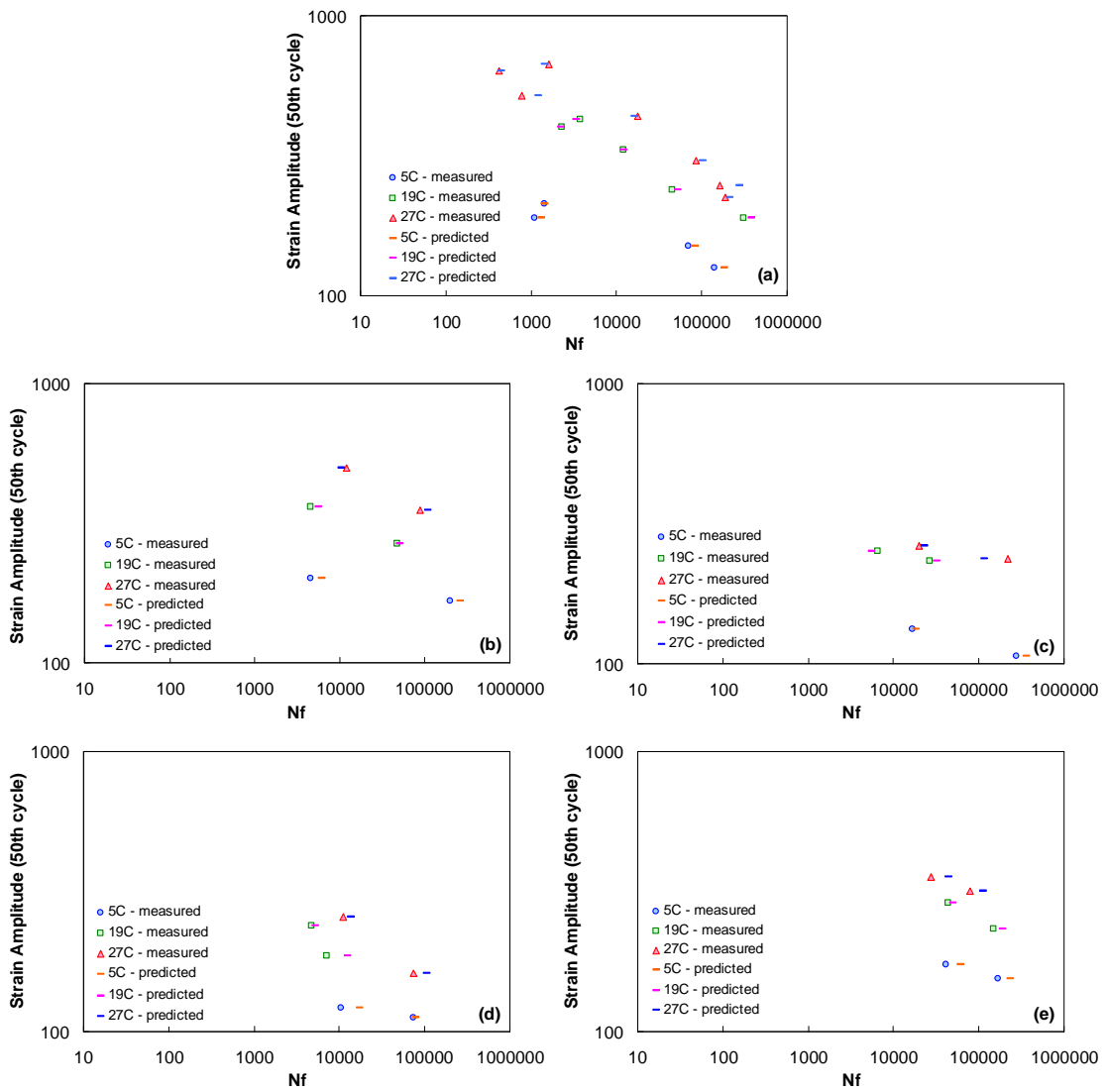


Figure 6.4 Controlled-crosshead cyclic test simulation results for (a) S9.5C; (b) S9.5B; (c) I19C; (d) B25B; (e) RS9.5C mix.

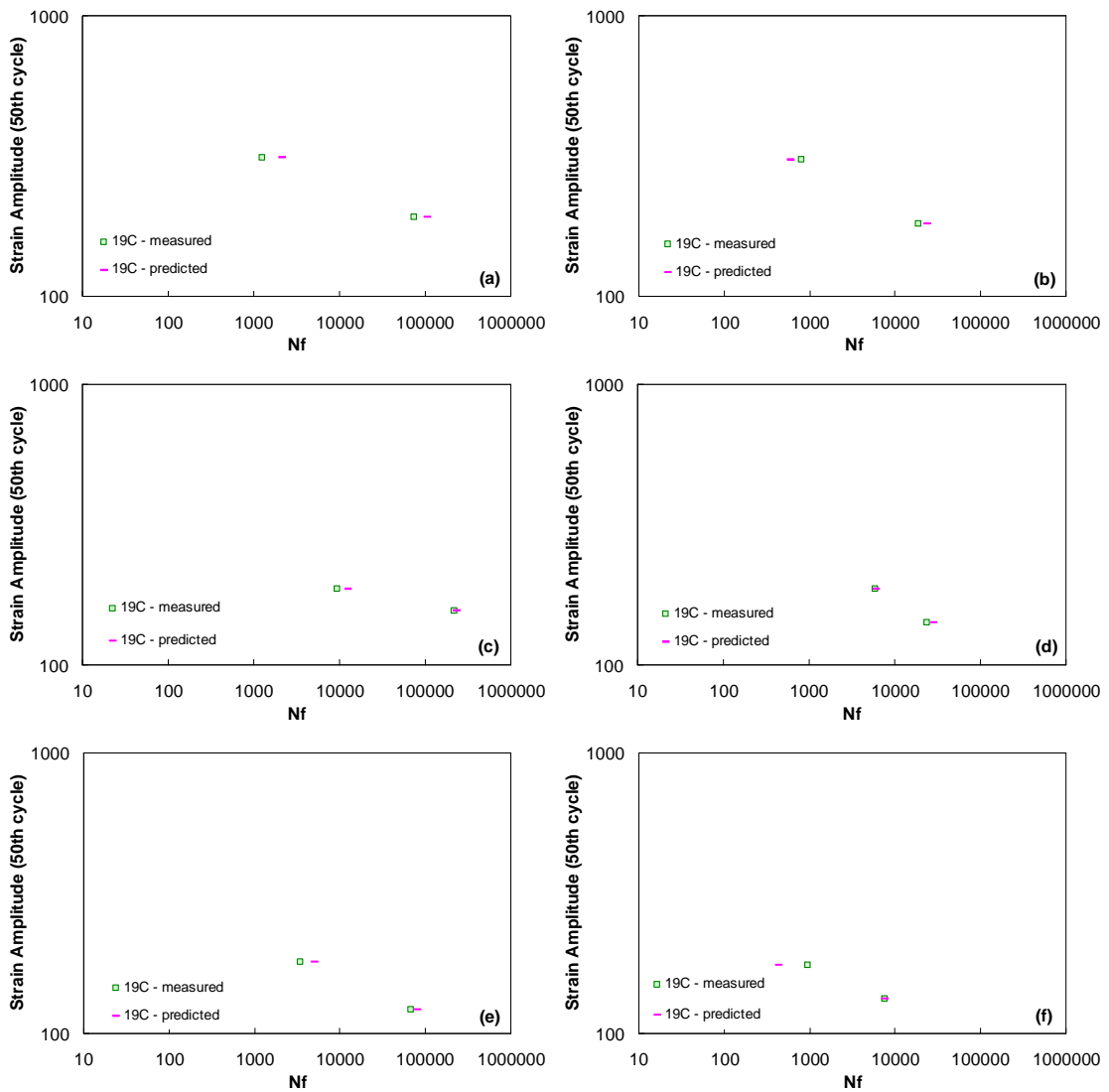


Figure 6.5 Controlled-crosshead cyclic test simulation results for (a) S12.5C; (b) I19B; (c) RS12.5C; (d) RI19B; (e) RI19C; (f) RB25B mix.

By looking at the comparison of measured and predicted fatigue life (Figure 6.6), it is found that there is a slight tendency to overestimate the fatigue life.

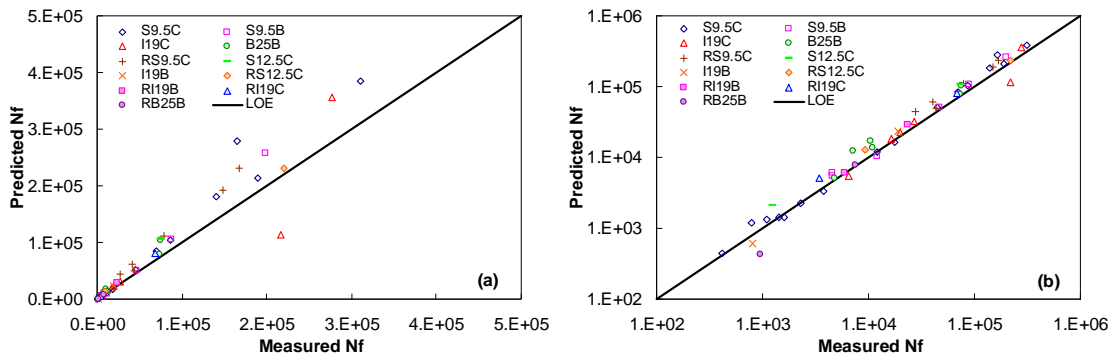


Figure 6.6 Comparison of measured and predicted fatigue life for all mixtures in (a) arithmetic scale; (b) log scale

The overestimation can be caused by the following reasons:

- (1) The power law function does not fit well with experimental damage curves. Some mixtures, like RS12.5C and RI19C, have a rapid decrease in pseudo stiffness when specimen is close to failure.
- (2) End-failure specimens, e.g., all the tests of RS9.5C and S12.5C mix, fail at a high pseudo stiffness value, while the simulation failure envelope is calibrated using mid-failure test results only.
- (3) Most of the 27°C test curves stay below the calibrated damage characteristic curve due to viscoplasticity. When using the damage characteristic curve to predict 27°C tests, it over predicts the pseudo stiffness, and eventually over predicts the fatigue life.

6.3 Further Development of Failure Envelope Using Optimization Technique

One approach to make fatigue test prediction results better is to come up with a new failure envelope, which can reduce the difference between measured and predicted fatigue life. For this reason, a general study on failure envelope development is made based on mid-failure cyclic test data using optimization technique.

Based on observation, the desired shape of failure envelope is similar to that developed in Section 6.1, and the equation is shown as follows:

$$C_f^* = \begin{cases} b & f_R < 0.01 \\ a \cdot (\log(f_R) - \log(0.01)) + b & 0.01 \leq f_R < 10 \end{cases} \quad (6.3)$$

where a is a function of NMA5; and b is a function of RAP mixture versus non-RAP mixture. The shape of failure envelope is unknown when the reduced frequency is greater than 10 Hz, due to the availability of data points. The optimization process is done by Evolver, which is a genetic algorithm optimization add-in for Microsoft Excel. Two different objective functions are used: (a) the total prediction error in arithmetic scale; and (b) in log scale. By changing the values of coefficients in Equation (6.3), the sums of square of errors are minimized, and the prediction results after optimization are shown in Figure 6.8 and Figure 6.8.

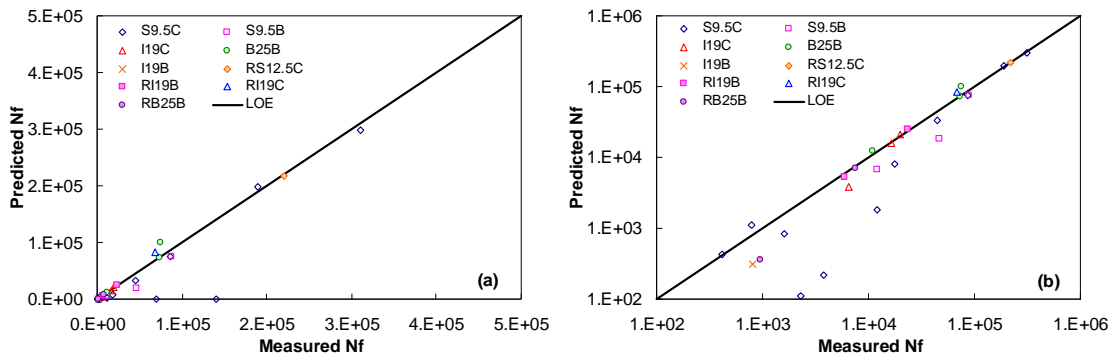


Figure 6.7 Fatigue life prediction result in (a) arithmetic; (b) log scale after minimizing total prediction error in arithmetic scale

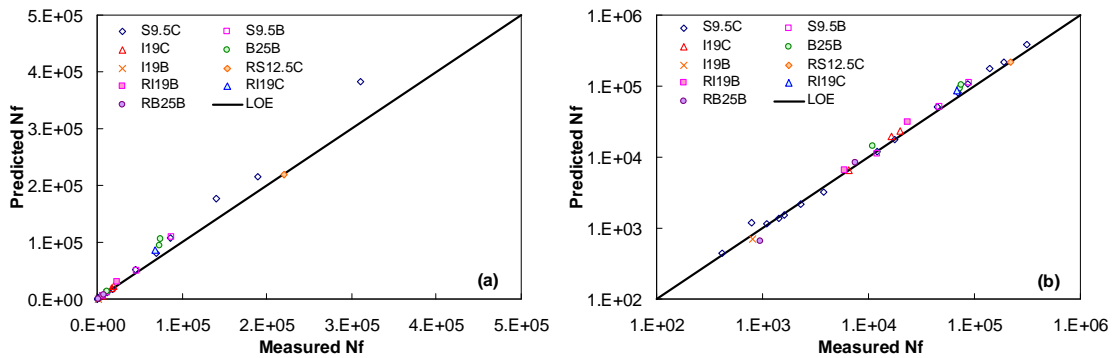


Figure 6.8 Fatigue life prediction result in (a) arithmetic; (b) log scale after minimizing total prediction error in log scale

By comparing the results after optimization using those two different objective functions, it is found that minimizing the total prediction error in log scale gives better overall prediction results, so all the further findings are based on using this objective function. The optimization yields a group of coefficients, which are listed in Table 6.2, and the resulting failure envelope is presented in Figure 6.9.

Table 6.2 Optimized failure envelope coefficients

Coefficient		Value
a	NMAS 9.5	0.073018
	NMAS 12.5	0.185247
	NMAS 19	0.033746
	NMAS 25	0.002675
b	Non-RAP	0.258598
	RAP	0.301445

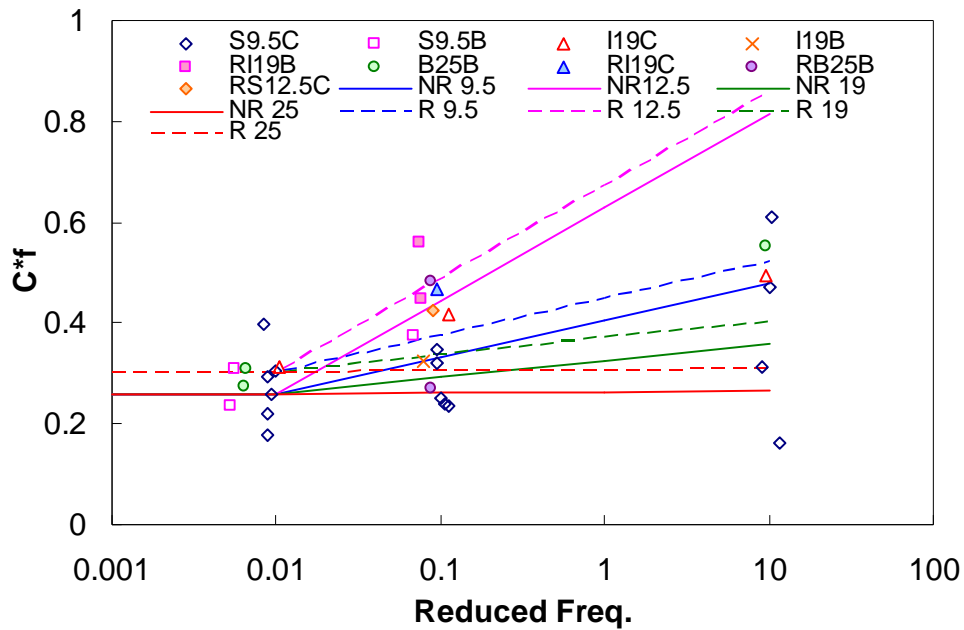


Figure 6.9 Optimized failure envelope

The result in Figure 6.9 shows that the optimized failure envelope matches with the experimental data points. The value of intercept coefficient, b , for RAP mixtures is greater than that for Non-RAP mixtures. The value of slope coefficient, a , decreases with the increment of NMAS, except for 12.5mm mixture, which has a much greater value than all other aggregate sizes. This phenomenon can be caused by the lack of sufficient experimental

data points of 12.5 mm mixtures, as we can see there is only one RS12.5C data point used in the optimization process.

A closer look of relationship between slope coefficient and NMAAS is presented in Figure 6.10, and a linear regression line is generated in the same graph. Note that due to the availability of experimental data, the result for 12.5 mm mixture is not considered as reliable, and therefore it is not included in the regression analysis.

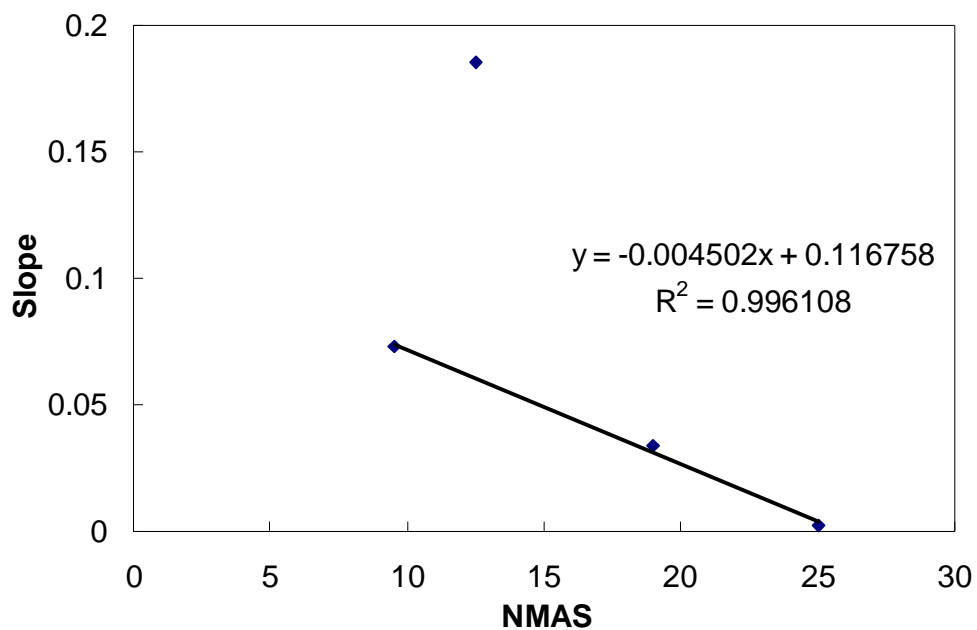


Figure 6.10 Optimized slope coefficients versus NMAAS

A final version of failure envelope is proposed in Equation (6.4), and its graphical representation is illustrated in Figure 6.11. As a conclusion, this failure envelope covers a range of cyclic tests whose reduced frequencies are less than 10 Hz. It uses the pseudo

stiffness value as the criterion to define failure. The value is assumed to be constant when the reduced frequency is less than 0.01 Hz, while it starts to increase as the reduced frequency goes beyond 0.01 Hz. In addition, the increasing rate is dependent on mixture's NMAS. For mixtures with a same NMAS tested at a certain reduced frequency, the value of pseudo stiffness at failure for RAP mixture is greater than Non-RAP mixture. This final failure envelope is then applied to predict fatigue life for mid-failure cyclic tests, and the result is presented in Figure 6.12.

$$C_f^* = \begin{cases} b & f_R < 0.01 \\ a \cdot (\log(f_R) - \log(0.01)) + b & 0.01 \leq f_R < 10 \end{cases} \quad (6.4)$$

where

$$a = -0.004502NMAS + 0.116758; \text{ and}$$

$$b = \begin{cases} 0.258598 & RAP \\ 0.301445 & non-RAP \end{cases}$$

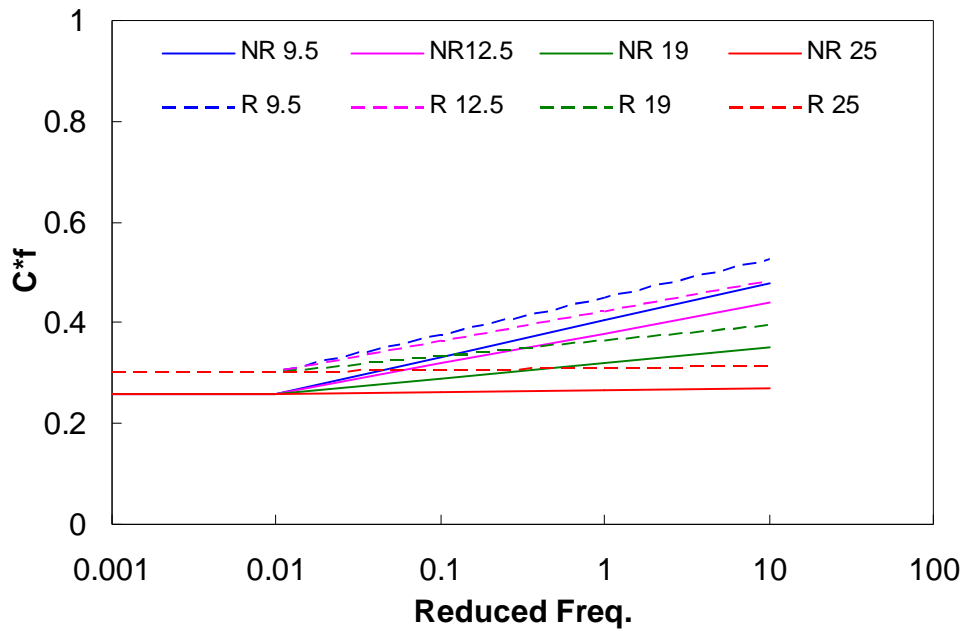


Figure 6.11 Final failure envelope

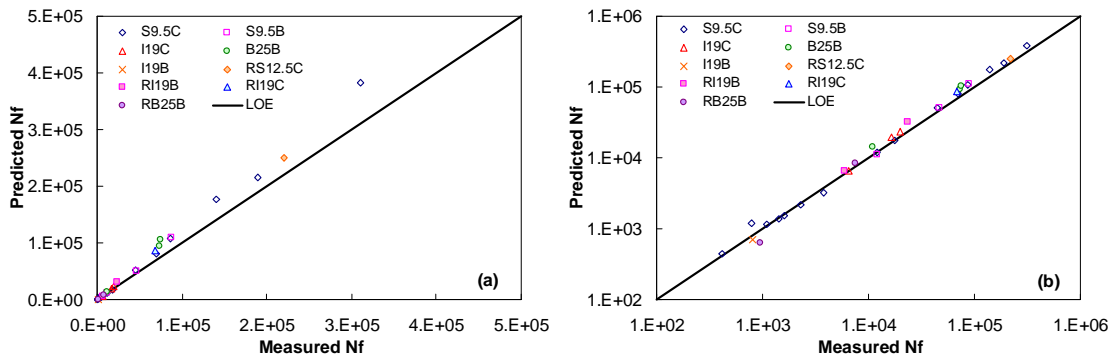


Figure 6.12 Fatigue life prediction result using final failure envelope

It is seen from Figure 6.12 that prediction error is further reduced by applying the new failure envelope as compared with Figure 6.6, and the over prediction problem is alleviated by ignoring the end-failure tests. It should be noted that this failure envelope has not been

validated yet due to the insufficiency of experimental data. Validation and improvement of the current failure envelope is part of the further research work.

6.4 Direct Tension Fatigue Simulation

One application of the simplified VECD model is to simulate purely strain controlled direct tension cyclic test. The theoretical background is described by the following equation derivations.

First, the damage calculation equation (Equation (4.18)) can be rewritten with respect to loading cycle, N , as follows:

$$dS = \left(-\frac{1}{2} (\varepsilon_{0,ta}^R)^2 \frac{\partial C^*}{\partial S} \right)^\alpha K_1 \left(\frac{dN}{f_{red}} \right) \quad (6.5)$$

where f_{red} is the reduced frequency of loading in Hz. The relationship between pseudo stiffness and damage is known as the power law function in Equation (5.1), and the derivative of pseudo stiffness with respect to damage is:

$$\frac{\partial C^*}{\partial S} = -C_{11} C_{12} S^{C_{12}-1} \quad (6.6)$$

Substituting Equation (6.6) into Equation (6.5) and isolating the terms relating to damage:

$$dS = \left(\frac{1}{2} (\varepsilon_{0,ta}^R)^2 C_{11} C_{12} \right)^\alpha K_1 \left(\frac{dN}{f_{red}} \right) (S^{(C_{12}-1)})^\alpha \quad (6.7)$$

and thus:

$$(S^{(C_{12}-1)})^{-\alpha} dS = \left(\frac{1}{2} (\varepsilon_{0,ta}^R)^2 C_{11} C_{12} \right)^\alpha K_1 \left(\frac{1}{f_{red}} \right) dN \quad (6.8)$$

Integrating Equation (6.8) on both sides:

$$\int_{S_{mi}}^{S_f} (S^{(C_{12}-1)})^{-\alpha} dS = \int_1^{N_f} \left(\frac{1}{2} (\epsilon_{0,ta}^R)^2 C_{11} C_{12} \right)^\alpha K_1 \left(\frac{1}{f_{red}} \right) dN \quad (6.9)$$

$$\frac{S^{\alpha-\alpha C_{12}+1}}{\alpha-\alpha C_{12}+1} \Big|_{S_{mi}}^{S_f} = \left(\frac{1}{2} (\epsilon_{0,ta}^R)^2 C_{11} C_{12} \right)^\alpha K_1 \left(\frac{1}{f_{red}} \right) (N_f - 1) \quad (6.10)$$

$$\frac{S_f^{\alpha-\alpha C_{12}+1}}{\alpha-\alpha C_{12}+1} - \frac{S_{mi}^{\alpha-\alpha C_{12}+1}}{\alpha-\alpha C_{12}+1} = \left(\frac{1}{2} (\epsilon_{0,ta}^R)^2 C_{11} C_{12} \right)^\alpha K_1 \left(\frac{1}{f_{red}} \right) (N_f - 1) \quad (6.11)$$

Assuming that $S_{mi} \ll S_f$ and that $N_f \gg 1$, Equation (6.11) is simplified to:

$$\frac{S_f^{\alpha-\alpha C_{12}+1}}{\alpha-\alpha C_{12}+1} = \left(\frac{1}{2} (\epsilon_{0,ta}^R)^2 C_{11} C_{12} \right)^\alpha K_1 \left(\frac{1}{f_{red}} \right) (N_f) \quad (6.12)$$

Rearranging Equation (6.12), the fatigue life, N_f , is given as follows:

$$N_f = \frac{(f_{red})(2^\alpha) S_f^{\alpha-\alpha C_{12}+1}}{(\alpha-\alpha C_{12}+1)(C_{11} C_{12})^\alpha (\epsilon_{0,ta}^R)^{2\alpha} K_1} \quad (6.13)$$

Substituting the cyclic portion of pseudo strain in Equation (4.16) into Equation (6.13) and recognizing that $E_R = 1$:

$$N_f = \frac{(f_{red})(2^\alpha) S_f^{\alpha-\alpha C_{12}+1}}{(\alpha-\alpha C_{12}+1)(C_{11} C_{12})^\alpha [(\beta+1)(\epsilon_{0,pp})(|E^*|_{LVE})]^{2\alpha} K_1} \quad (6.14)$$

For different strain amplitude, loading frequency and temperature, different fatigue life can be obtained using the above equation. The simulation results can then be fitted by the empirical model (Equation (1.3)). Figure 6.13 and Figure 6.14 show the simulation results of strain controlled direct tension cyclic tests for all the eleven mixes at 5, 19 and 27°C. Note

that all the simulated tests are in a zero mean strain condition, i.e., $\beta=0$, and the loading frequency is 10 Hz. The failure criterion used in simulation is the same as the one developed in Section 6.3, i.e., S_f is calculated from C_f^* through the power law function. Table 6.3 summarizes the regression coefficients of empirical model for all the mixes from direct tension fatigue test simulation.

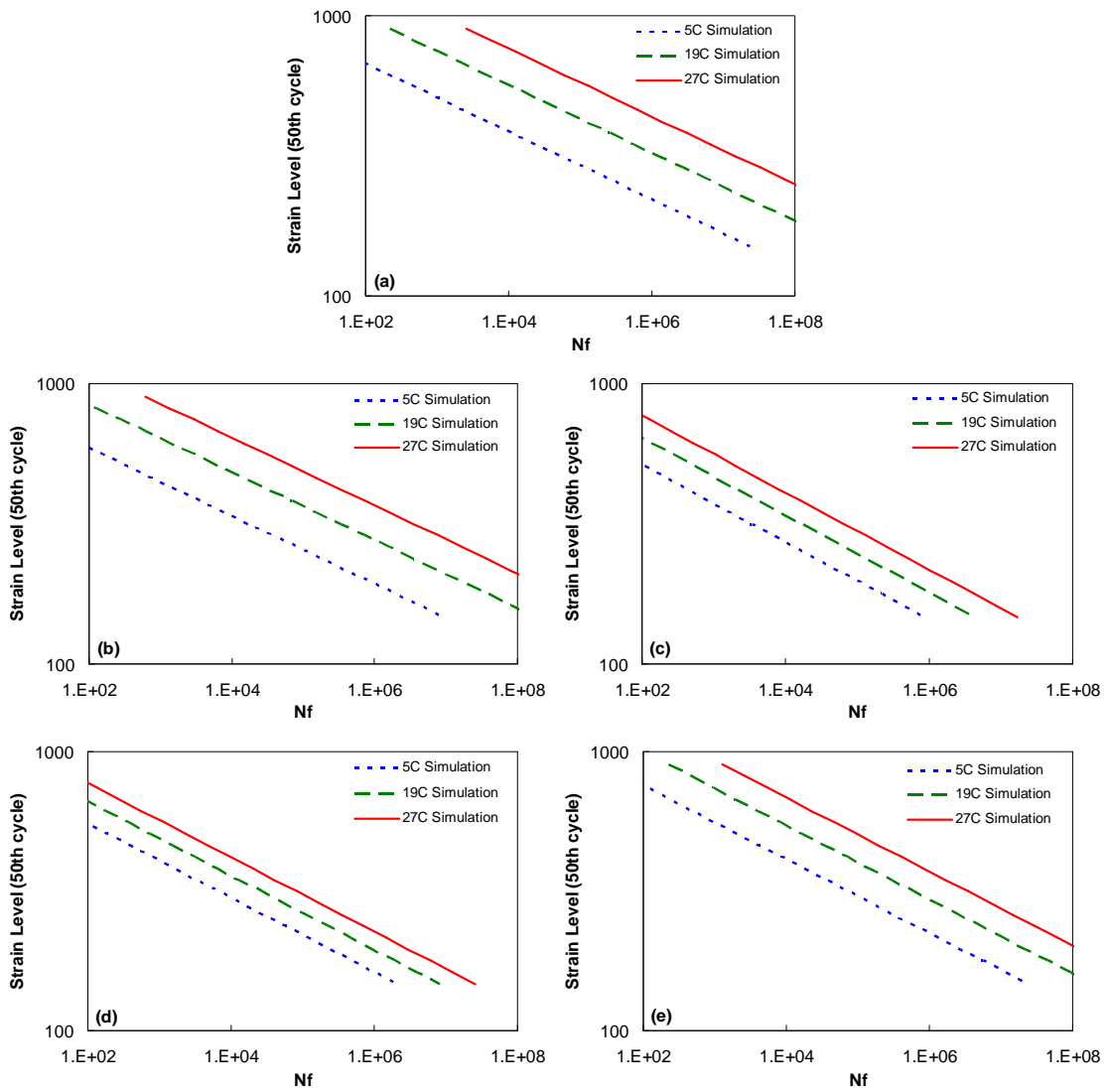


Figure 6.13 Strain controlled direct tension fatigue test simulation results for (a) S9.5C; (b) S9.5B; (c) I19C; (d) B25B and (e) RS9.5C.

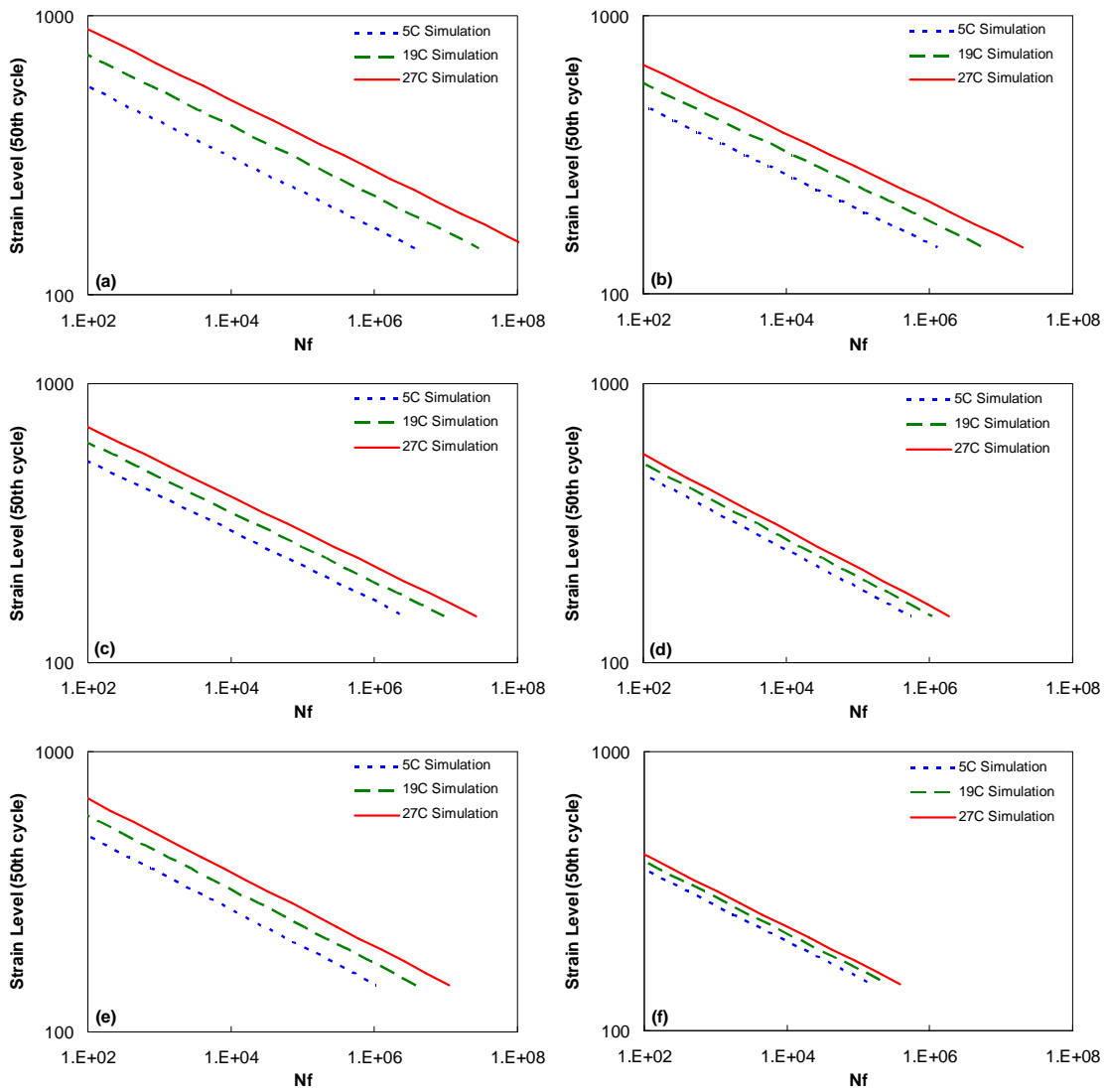


Figure 6.14 Strain controlled direct tension fatigue test simulation results for (a) S12.5C; (b) I19B; (c) RS12.5C; (d) RI19B; (e) RI19C and (f) RB25B.

Table 6.3 Summary of regression coefficients for empirical model from direct tension fatigue simulation

mixture	k_1	k_2	k_3
S9.5C	2.396E+10	8.253	-4.821
S9.5B	4.885E+04	8.253	-4.099
I19C	8.860E-06	7.275	-2.327
B25B	4.752E-09	7.510	-1.951
RS9.5C	1.017E+02	7.547	-3.262
S12.5C	1.514E-01	7.902	-3.180
I19B	7.212E-09	8.090	-2.329
RS12.5C	5.828E-09	8.000	-2.191
RI19B	5.068E-15	7.391	-1.135
RI19C	9.159E-09	7.609	-2.056
RB25B	1.134E-18	7.762	-0.913

Comparisons of simulation results at different temperatures (5, 19 and 27°C) are made through Figure 6.15 to Figure 6.17. It is seen that at all three temperatures, mixture's fatigue performance drops as its nominal maximum aggregate size increases, i.e., the 9.5 mm mixtures exhibit most fatigue resistance, while the 25 mm mixtures are the most prone to fatigue damage. Also, it is observed that, in general, non-RAP mixtures are more fatigue resistant than RAP mixtures at all temperatures, except that at 5°C the RS9.5C mix has a better performance than the S9.5C mix. In addition, the difference in fatigue performance between different mixtures increases with the test temperature. In other words, at a higher temperature like 27°C, asphalt mixtures fatigue performance is more mixture type dependent than that at a lower temperature.

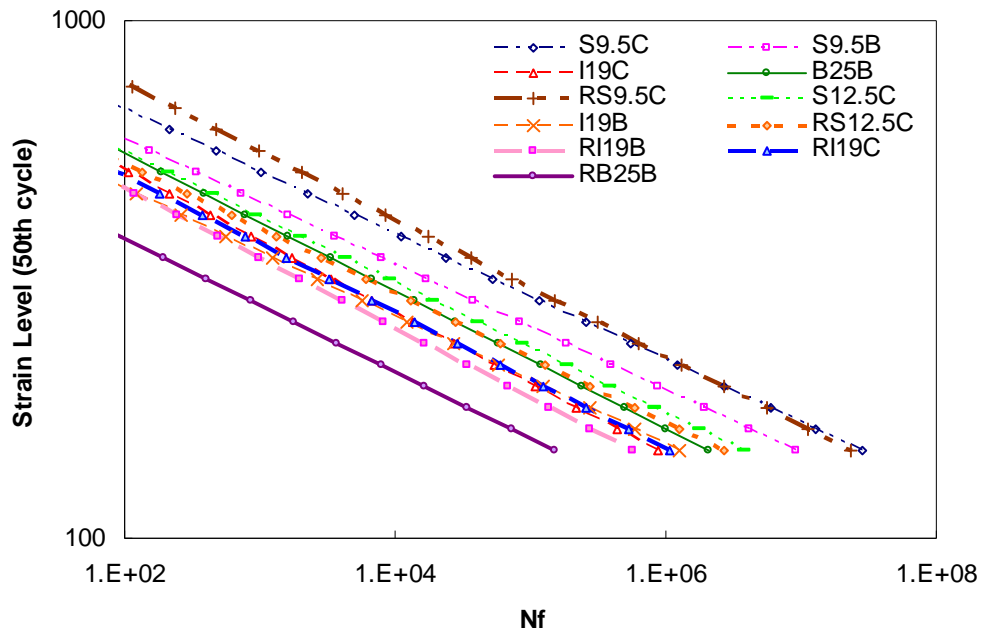


Figure 6.15 5°C strain controlled direct tension fatigue test simulations for all mixtures

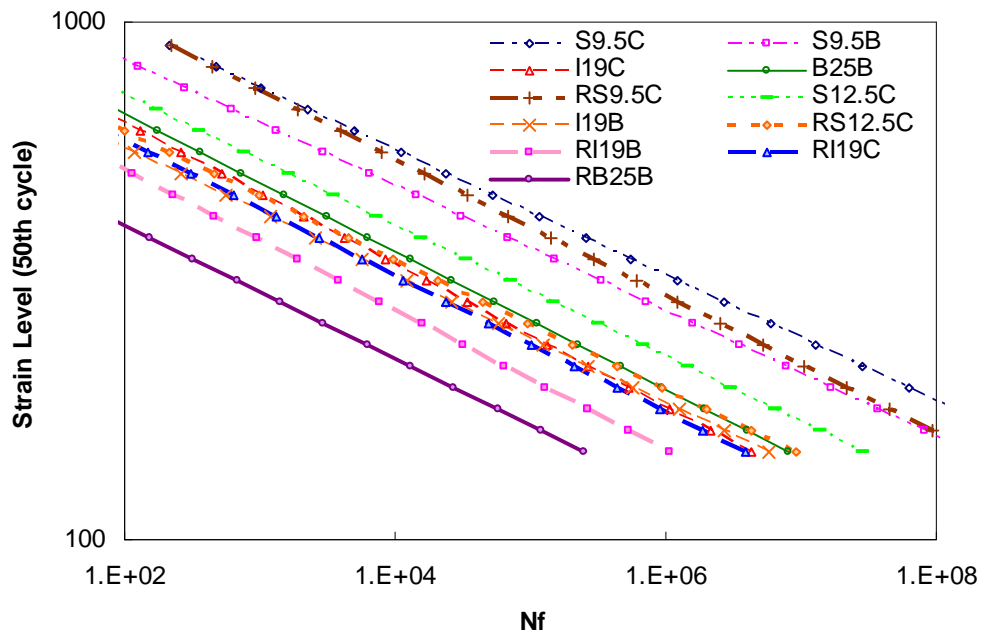


Figure 6.16 19°C strain controlled direct tension fatigue test simulations for all mixtures

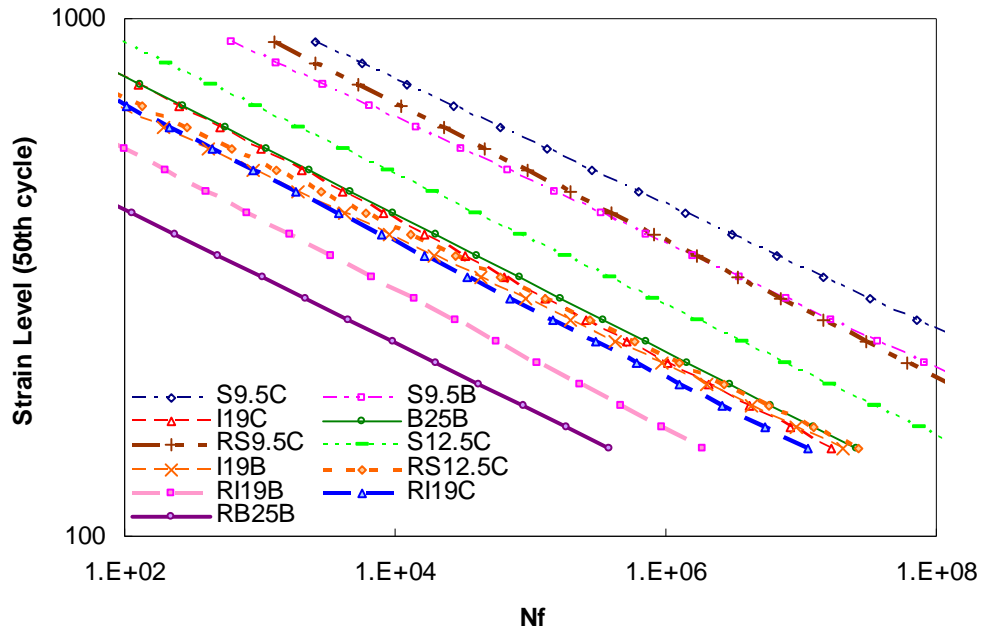


Figure 6.17 27°C strain controlled direct tension fatigue test simulations for all mixtures

6.5 Beam Fatigue Simulation

Another important application of the simplified VECD model is to simulate the traditional beam fatigue test. In this study, the method proposed by Christensen and Bonaquist (2005) is used. During the analysis, the standard beam is divided into ten equal layers from top to bottom, each with a thickness of 5 mm. The test is simulated to be performed in a strain controlled mode, i.e. the tensile strain amplitude at the bottom of the beam reaches a constant peak value during each cycle and back to zero at the end of each cycle. The entire loading history is divided into logarithmically spaced intervals, and the accumulated damage during each interval is calculated using Equation (6.7) for each layer. The cyclic portion of pseudo strain calculation in Equation (4.16) is used. Note that β is equal to 1 in this case. The

resulting pseudo stiffness can then be calculated at the end of each loading interval. The modulus of each layer is assumed not to change during the test, however, however, the effective width of each layer is adjusted proportional to the pseudo stiffness due to the damaged caused in the previous interval, as Equation (6.15).

$$(w_{eff})_i = (w_{ini})_i \cdot C_i^* \quad (6.15)$$

where

w_{eff} = effective width;

w_{ini} = initial width; and

i = layer index.

A new moment of inertia and neutral axis is then calculated based on the new beam dimension. Note that damage only occurs below the neutral axis, for the layers which are above the neutral axis, their effective widths remain constant as they are subjected to compressive stresses only. The simulation process is illustrated graphically in Figure 6.18.

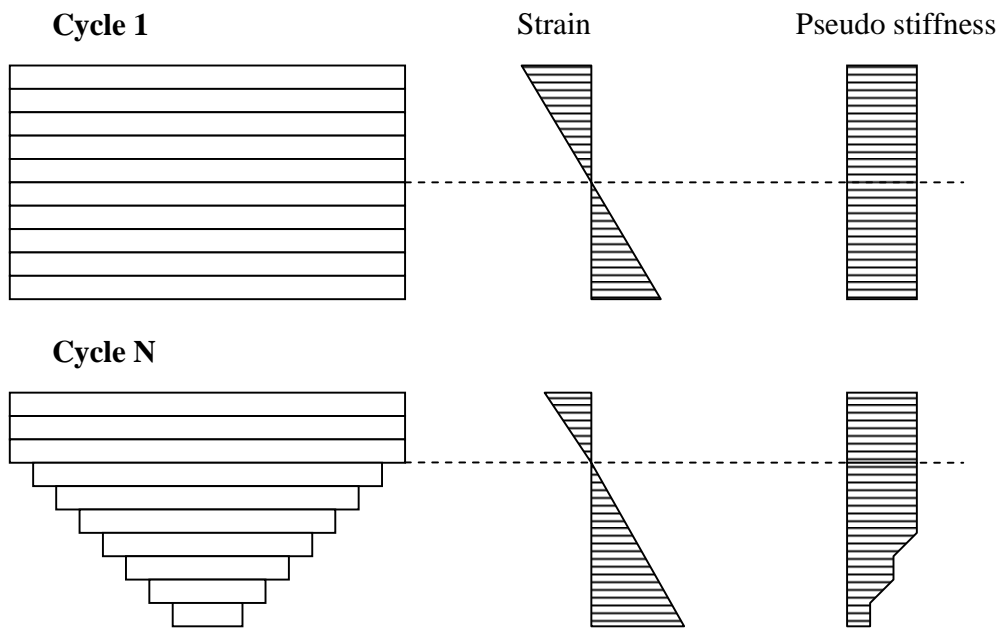


Figure 6.18 Beam fatigue test simulation process

For each layer, when its pseudo stiffness touches the failure envelope described in Section 6.3, its effective width is assumed to be zero for the rest of the analysis. For the entire beam structure, failure is defined by the 50% stiffness reduction criterion, of which the stiffness ratio at cycle, N , is calculated by:

$$S(N) = \frac{I_N}{I_{ini}} \quad (6.16)$$

where I_{ini} and I_N are moment of inertia at the 50th and N^{th} loading cycle, respectively. Figure 6.19 shows an example of beam fatigue simulation result

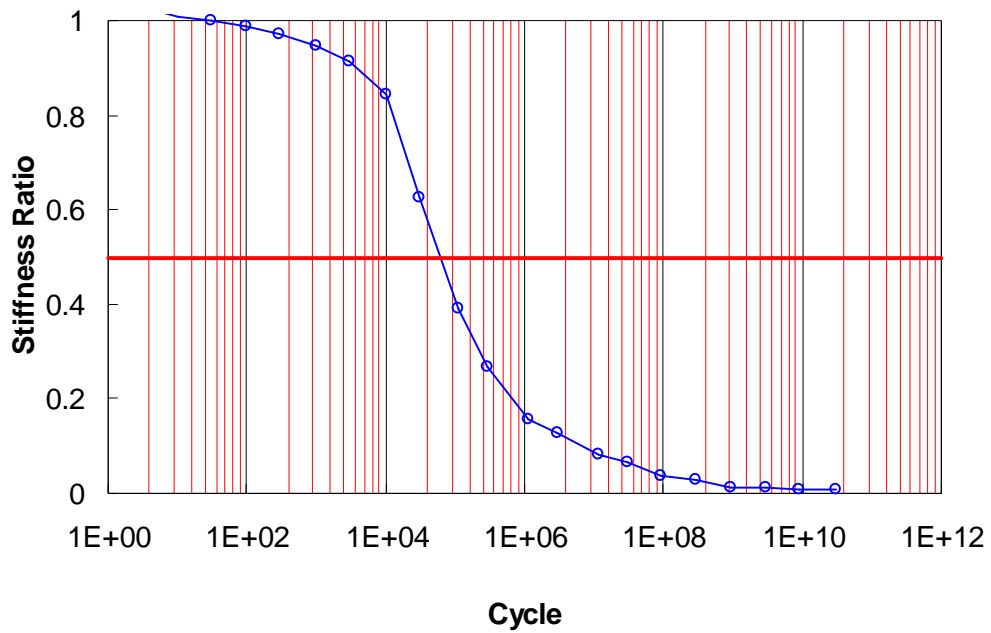


Figure 6.19 Example of beam fatigue simulation result

Similar as that has been done in direct tension fatigue simulation, beam fatigue tests subjected to different strain levels are simulated to give different fatigue lives. Those results are then fitted by the empirical model. Figure 6.20 and Figure 6.21 show the simulation results at 5, 19 and 27°C for all the eleven mixes. And the regression coefficients for the empirical model are summarized in Table 6.4.

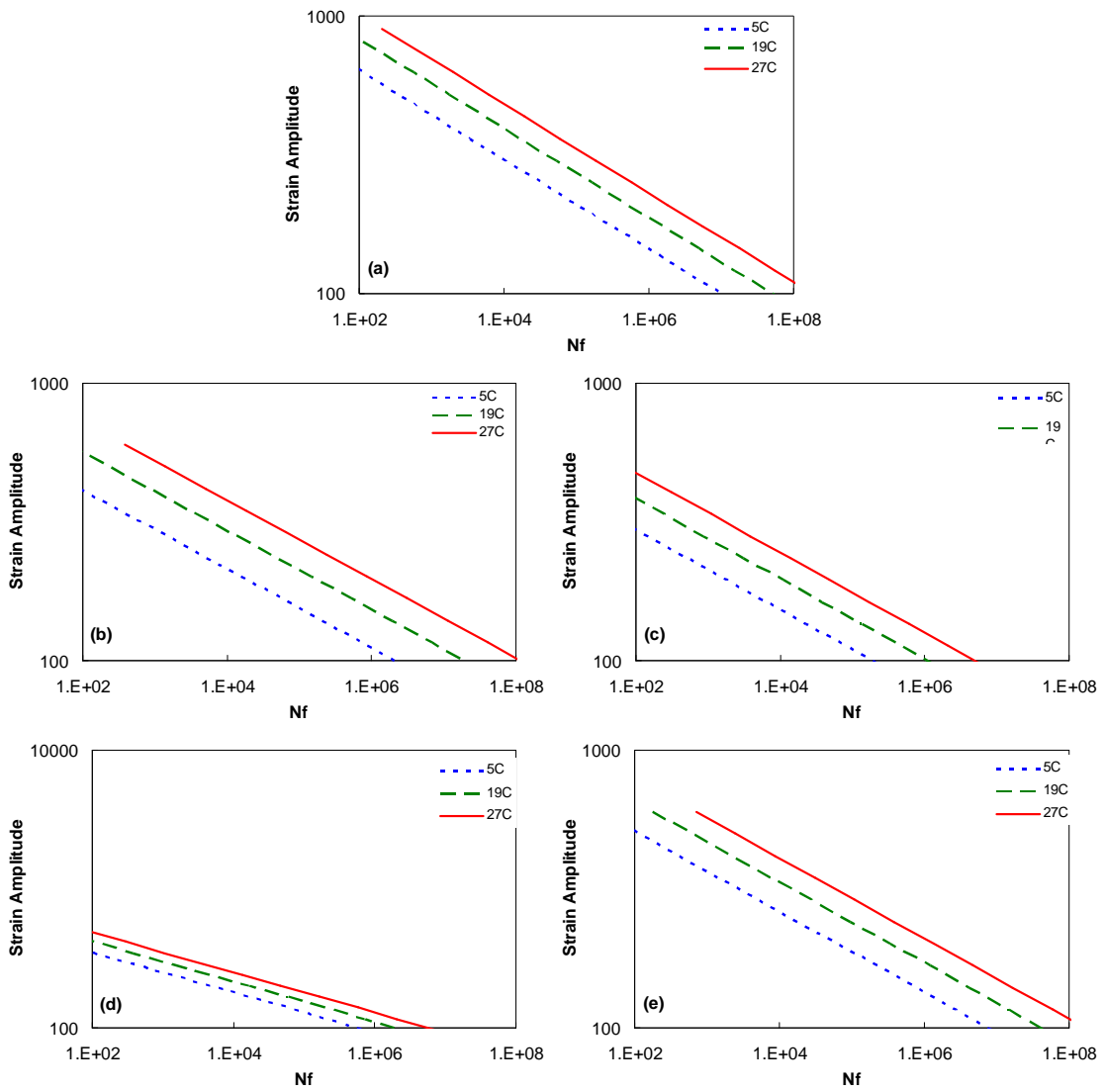


Figure 6.20 Beam fatigue test simulation results for (a) S9.5C; (b) S9.5B; (c) I19C; (d) B25B and (e) RS9.5C.

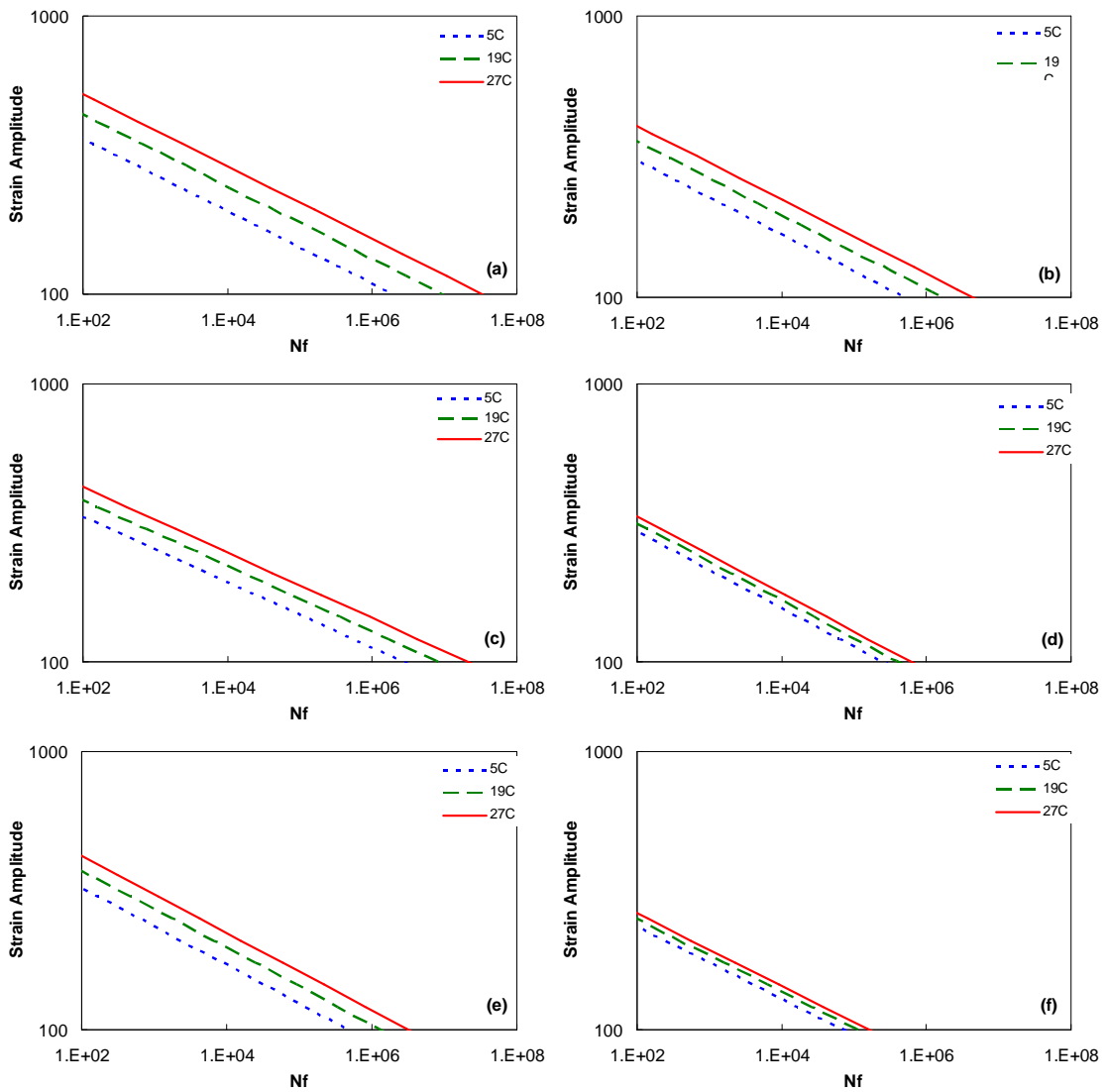


Figure 6.21 Beam fatigue test simulation results for (a) S12.5C; (b) I19B; (c) RS12.5C; (d) RI19B; (e) RI19C and (f) RB25B.

Table 6.4 Summary of regression coefficients for empirical model from beam fatigue simulation

mixture	k_1	k_2	k_3
S9.5C	6.958E-01	6.235	-2.481
S9.5B	1.834E+00	7.056	-3.096
I19C	2.708E-04	6.916	-2.595
B25B	1.059E-09	6.919	-1.784
RS9.5C	1.193E-02	6.914	-2.609
S12.5C	1.056E-07	7.688	-2.430
I19B	2.647E-12	7.609	-1.829
RS12.5C	1.685E-13	8.454	-2.002
RI19B	5.452E-18	7.231	-0.859
RI19C	1.873E-11	7.203	-1.691
RB25B	1.011E-20	7.675	-0.807

Similar to what has been done in the direct tension fatigue simulation, comparisons of fatigue performance between different mixtures at three different temperatures (5, 19 and 27°C) are made in Figure 6.22 to Figure 6.24. The conclusions are consistent with those drawn from direct tension fatigue simulation, i.e., mixture's fatigue resistance decreases as the nominal maximum aggregate size increase, and non-RAP mixtures have better fatigue performance than RAP mixtures.

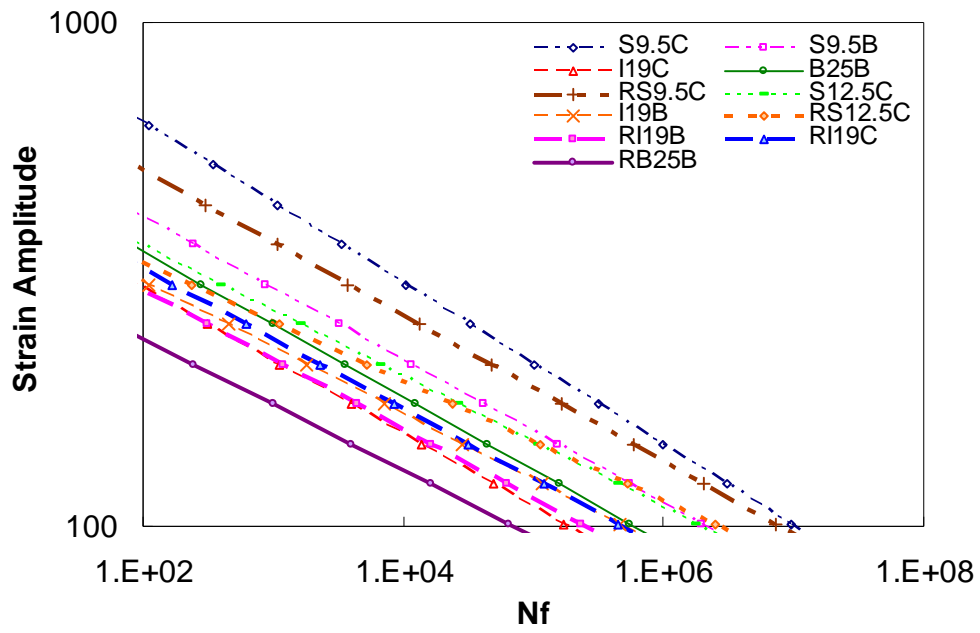


Figure 6.22 5°C beam fatigue test simulations for all mixtures

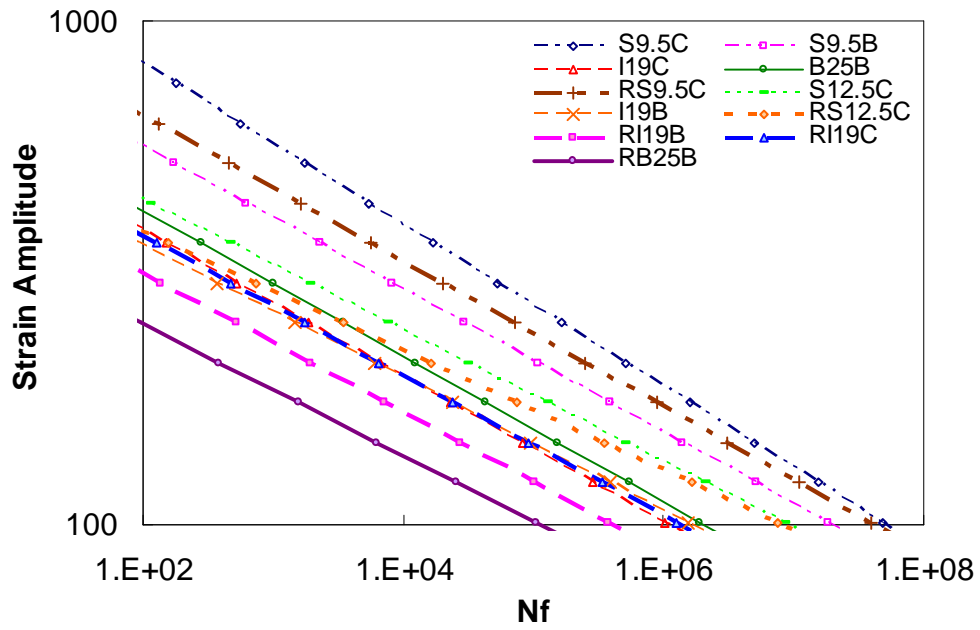


Figure 6.23 19°C beam fatigue test simulations for all mixtures

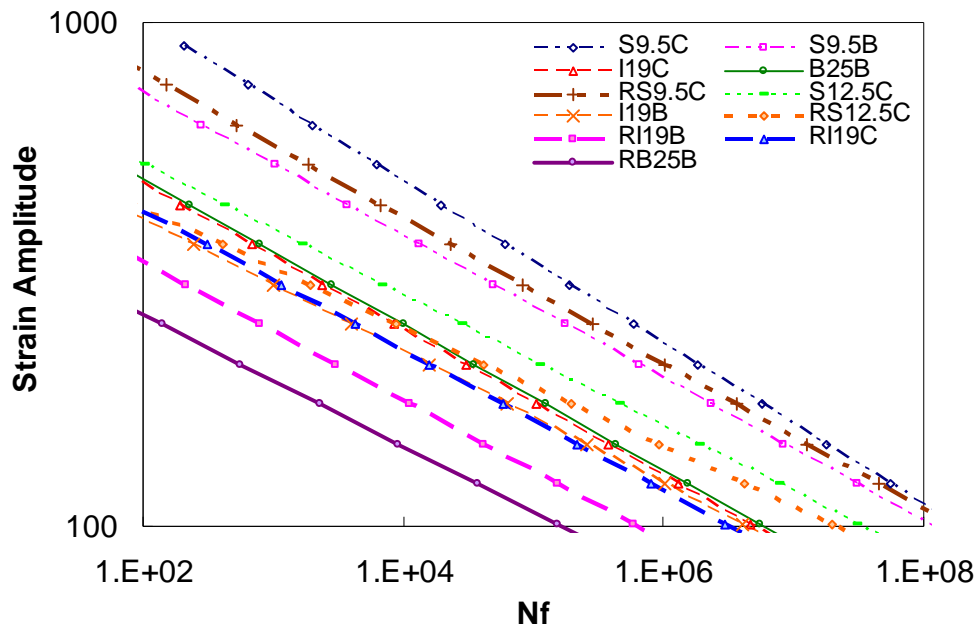


Figure 6.24 27°C beam fatigue test simulations for all mixtures

It is found that the slopes of the fatigue envelopes for the different mixtures are quite close to each other for both the direct tension and beam fatigue tests. So, by comparing the positions of those straight lines, it is easy to rank the fatigue life of the different mixtures under the same loading condition. The fatigue performance rankings from both the direct tension and beam fatigue simulations are summarized in Table 6.5. The findings are encouraging that those two different simulation approaches give similar mixture performance rankings under different test conditions.

Table 6.5 Summary of fatigue performance ranking

Mixture	Fatigue Resistance Rank from Direct Tension Fatigue Simulation			Fatigue Resistance Rank from Direct Tension Fatigue Simulation		
	5°C	19°C	27°C	5°C	19°C	27°C
S9.5C	2	1	1	1	1	1
S9.5B	3	3	3	3	3	3
I19C	8	7	6	10	7	7
B25B	5	6	5	6	6	5
RS9.5C	1	2	2	2	2	2
S12.5C	4	4	4	4	4	4
I19B	9	8	8	8	8	8
RS12.5C	6	5	7	5	5	6
RI19B	10	10	10	9	10	10
RI19C	7	9	9	7	9	9
RB25B	11	11	11	11	11	11

Chapter 7 Conclusions and Future Research Recommendations

In this study, a simplified form of VECD model is derived, which is capable of utilizing cyclic fatigue test data at multiple temperatures and strain magnitudes. The advantage of this simplified model over the rigorous model is that it can characterize HMA's fatigue performance quickly using cyclic data without computing at each time step. This advantage is extremely important for the newly released AMPT testing equipment, which has a load level limitation to perform constant rate tension test. The model is verified by characterizing different asphalt concrete mixtures in the North Carolina MEPDG local calibration project. The results show that the model can be applied to accurately predict the fatigue life of asphalt concrete under cyclic loading at multiple temperatures and strain levels. The model is also applied to simulate both strain controlled direct tension cyclic test and beam fatigue test.

There are a few areas where there is room to improve in the future. The failure criterion incorporated in predicting fatigue life is empirical and contains certain shortcomings. A more theoretically-based failure criterion is needed to improve the accuracy of fatigue performance prediction. The simulated direct tension and beam fatigue results using the simplified VECD model have not yet been verified by real experiments. The relationship between the simulated results and experimental results would be a valuable research topic for the future.

References

AASHTO T 321 Standard Method of Test for Determining the Fatigue Life of Compacted Hot-Mix Asphalt (HMA) Subjected to Repeated Flexural Bending (2008). AASHTO, Washington D.C.

AASHTO TP 62 Standard Method of Test for Determining Dynamic Modulus of Hot-Mix Asphalt Concrete Mixtures (2004). AASHTO, Washington D.C.

Chehab, G., Y. R. Kim, R. A. Schapery, M. Witzack, R. Bonaquist (2002). "Time-Temperature Superposition Principle for Asphalt Concrete Mixtures with Growing Damage in Tension State." *Journal of Association of Asphalt Paving Technologists*, Vol. 71, pp: 559-593.

Chehab, G., Y.R. Kim, R.A. Schapery, M. Witzack, R. Bonaquist (2003). "Characterization of Asphalt Concrete in Uniaxial Tension Using a Viscoelastoplastic Model." *Journal of Association of Asphalt Paving Technologists*, Vol. 72, pp: 315-355.

Christensen, D.W. and R. Bonaquist (2005). "Practical Application of Continuum Damage Theory to Fatigue Phenomena in Asphalt Concrete Mixtures." *Journal of the Association of Asphalt Paving Technologists*, Vol. 74, pp: 963-1002.

Daniel, J.S. and Y. R. Kim (2002). "Development of a Simplified Fatigue Test and Analysis Procedure Using a Viscoelastic Continuum Damage Model." *Journal of Association of Asphalt Paving Technologists*, Vol. 71, pp: 619-650.

Kim, Y.R., and D.N. Little (1990). "One-Dimensional Constitutive Modeling of Asphalt Concrete." *ASCE Journal of Engineering Mechanics*, Vol. 116, No. 4, pp. 751-772.

Kutay, M.E., N. Gibson, and J. Youtcheff (2008). "Conventional and Viscoelastic Continuum Damage (VECD) Based Fatigue Analysis of Polymer Modified Asphalt Pavements." *Journal of Association of Asphalt Paving Technologists*, Vol. 77. In Press.

Lee, H.J. and Y.R. Kim (1998a). "A Uniaxial Viscoelastic Constitutive Model for Asphalt Concrete under Cyclic Loading." *ASCE Journal of Engineering Mechanics*, Vol. 124, No. 1, pp: 32-40.

Lee, H.J. and Y.R. Kim (1998b). "A Viscoelastic Continuum Damage Model of Asphalt Concrete with Healing." *ASCE Journal of Engineering Mechanics*, Vol. 124, No. 11, pp: 1224-1232.

Monismith, C. L., Epps, J. A., and Finn, F. N. (1985). "Improved asphalt mix design." *Journal of Association of Asphalt Paving Technologists*, Vol. 54, pp: 347–391.

Reese, R. (1997). "Properties of Aged Asphalt Binder Related to Asphalt Concrete Fatigue Life." *Journal of the Association of Asphalt Paving Technologists*, Vol. 66, pp: 604-632.

Schapery, R.A. (1984). "Correspondence principles and a Generalized J-integral for Large Deformation and Fracture Analysis of Viscoelastic Media." *Int. J. Fract.*, Vol. 25, pp: 195-223.

Schapery, R.A. (1990). "A Theory of Mechanical Behavior of Elastic Media with Growing Damage and Other Changes in Structure" *J. Mech. Phys. Solids*, Vol. 38, pp: 215-253.

Schapery, R.A.(1981). "On Viscoelastic Deformation and Failure Behavior of Composite Materials with Distributed Flaws." *Advances in Aerospace Structures and Materials*, AD-01, ASME, New York, pp. 5-20.

Strategic Highway Research Program (SHRP) (1994). "Fatigue response of asphalt-aggregate mixes." SHRP-A-404, National Research Council, Washington, D.C.

Tayebali, A. T., J. A. Deacon, and C. L. Monismith (1995). "Development and Evaluation of Surrogate Fatigue Models for SHRP A-003A Abridged Mix Design Procedure," *Journal of the Association of Asphalt Paving Technologists*, Vol. 64, pp: 340-364.

Underwood, B. S., Y. R. Kim, and M. N. Guddati (2005). "Characterization and Performance Prediction of ALF Mixtures Using a Viscoelastoplastic Continuum Damage Model." *Journal of Association of Asphalt Paving Technologists*, Vol. 75, pp: 577-636.

Underwood. B.S., Y.R. Kim, S. Savadatti, S. Thirunavukkarasu, and M.N. Guddati. (2009). "Response and Fatigue Performance Modeling of ALF Pavements Using 3-D Finite Element Analysis and a Simplified Viscoelastic Continuum Damage Model," *Journal of the Association of Asphalt Paving Technologists*. In Press.

Underwood, B.S., Y.R. Kim, and M.N. Guddati. (2009). "Improved Calculation Method of Damage Parameter in Viscoelastic Continuum Damage Model," *International Journal of Pavement Engineering*. Under Review.

Appendices

Appendix A Complex Modulus Test Data

Table A.1 Summary of sigmoidal coefficients and shift factor coefficients for all mixtures

Mixture	Sigmoidal Coefficients				Shift Factor Function Coefficients		
	<i>a</i>	<i>b</i>	<i>d</i>	<i>g</i>	α_1	α_2	α_3
S9.5C	1.532122	2.875487	1.586880	0.456310	0.000553	-0.158166	0.777001
S9.5B	1.676516	2.714347	1.955035	0.473981	0.000691	-0.168455	0.825009
I19C	1.810291	2.627181	1.540542	0.605129	0.000550	-0.150735	0.739928
B25B	1.507309	2.945305	2.152708	0.509385	0.000714	-0.165149	0.807893
RS9.5C	1.553675	2.860244	1.733648	0.521016	0.000572	-0.158831	0.779866
S12.5C	1.918581	2.455040	1.567928	0.579862	0.000608	-0.155955	0.764562
I19B	1.561657	2.846584	1.691287	0.473519	0.000629	-0.165659	0.812579
RS12.5C	1.778298	2.687005	1.832713	0.511607	0.000588	-0.159986	0.785233
RI19B	1.623906	2.820031	1.953727	0.540356	0.000580	-0.161039	0.790686
RI19C	1.908373	2.589046	1.720861	0.574218	0.000614	-0.157423	0.771772
RB25B	1.659233	2.755876	1.870465	0.518901	0.000659	-0.160955	0.788299

Table A.2 Complex Modulus Test Result Data for S9.5C Mixture

Temperature (C)	Frequency (Hz)	Average E* (MPa)	Average Phase Angle (deg)
-10	25	22926	5.0
	10	21936	5.3
	5	21103	5.5
	1	18975	6.5
	0.5	18067	6.8
	0.1	15808	8.1
5	25	15856	8.7
	10	14491	9.2
	5	13507	9.7
	1	11182	11.3
	0.5	10241	11.9
	0.1	8149	14.5
20	25	8593	16.2
	10	7377	17.0
	5	6418	18.7
	1	4499	22.7
	0.5	3814	24.1
	0.1	2500	28.8
40	25	2386	30.9
	10	1771	32.7
	5	1420	33.1
	1	800	34.5
	0.5	655	34.7
	0.1	397	33.5
54	25	810	36.4
	10	606	36.4
	5	487	35.8
	1	289	31.4
	0.5	228	30.5
	0.1	162	26.1

Table A.3 Complex Modulus Test Result Data for S9.5B Mixture

Temperature (C)	Frequency (Hz)	Average E* (MPa)	Average Phase Angle (deg)
-10	25	22801	6.0
	10	22007	6.1
	5	21308	6.4
	1	19151	7.2
	0.5	18351	7.7
	0.1	16189	9.2
5	25	15618	10.3
	10	14190	11.2
	5	13231	11.3
	1	10872	12.6
	0.5	9981	13.4
	0.1	7868	16.4
20	25	7922	17.1
	10	6715	18.9
	5	5840	20.4
	1	4014	24.1
	0.5	3421	25.6
	0.1	2192	30.3
40	25	1937	33.8
	10	1376	36.0
	5	1063	36.5
	1	659	39.0
	0.5	485	37.3
	0.1	308	35.4
54	25	677	40.0
	10	473	38.9
	5	376	37.2
	1	234	32.6
	0.5	209	29.5
	0.1	171	26.0

Table A.4 Complex Modulus Test Result Data for I19C Mixture

Temperature (C)	Frequency (Hz)	Average E* (MPa)	Average Phase Angle (deg)
-10	25	26807	2.9
	10	25964	3.1
	5	25118	3.3
	1	22747	4.2
	0.5	21808	4.6
	0.1	19001	7.2
5	25	19066	7.4
	10	17503	8.2
	5	16262	8.9
	1	13159	11.3
	0.5	11970	12.4
	0.1	9076	16.1
20	25	10286	16.7
	10	8773	17.2
	5	7304	21.0
	1	4639	26.7
	0.5	3780	28.9
	0.1	2283	37.4
40	25	2393	37.7
	10	1610	39.2
	5	1202	40.0
	1	661	40.8
	0.5	508	39.8
	0.1	279	32.3
54	25	749	42.9
	10	476	38.7
	5	376	36.8
	1	225	30.0
	0.5	193	26.3
	0.1	143	20.8

Table A.5 Complex Modulus Test Result Data for B25B Mixture

Temperature (C)	Frequency (Hz)	Average E* (MPa)	Average Phase Angle (deg)
-10	25	26784	7.1
	10	25951	7.7
	5	25204	8.0
	1	22952	9.0
	0.5	22031	9.0
	0.1	19848	9.2
5	25	19010	10.7
	10	17587	11.9
	5	16457	12.5
	1	13644	14.3
	0.5	12521	15.3
	0.1	9988	18.8
20	25	9919	20.8
	10	8379	23.1
	5	7124	25.0
	1	4696	30.0
	0.5	3904	32.4
	0.1	2349	37.8
40	25	2298	40.5
	10	1591	42.7
	5	1206	42.7
	1	635	43.6
	0.5	501	41.8
	0.1	290	36.8
54	25	742	45.6
	10	480	42.9
	5	351	40.7
	1	207	33.5
	0.5	172	29.1
	0.1	134	23.5

Table A.6 Complex Modulus Test Result Data for RS9.5C Mixture

Temperature (C)	Frequency (Hz)	Average E* (MPa)	Average Phase Angle (deg)
-10	25	24854	3.4
	10	24050	3.8
	5	23269	4.0
	1	21190	4.8
	0.5	20327	5.1
	0.1	18109	7.0
5	25	17749	7.1
	10	16381	7.9
	5	15266	8.3
	1	12735	9.9
	0.5	11656	10.9
	0.1	9279	13.4
20	25	9758	15.2
	10	8375	16.6
	5	7281	18.3
	1	4996	22.4
	0.5	4211	24.2
	0.1	2604	28.8
40	25	2500	32.0
	10	1772	34.9
	5	1353	35.6
	1	812	40.1
	0.5	539	35.8
	0.1	304	32.8
54	25	722	37.6
	10	528	38.1
	5	400	35.8
	1	230	31.2
	0.5	191	28.5
	0.1	129	23.6

Table A.7 Complex Modulus Test Result Data for S12.5C Mixture

Temperature (C)	Frequency (Hz)	Average E* (MPa)	Average Phase Angle (deg)
-10	25	23301	4.1
	10	22640	4.2
	5	21963	4.4
	1	19918	5.4
	0.5	19185	5.6
	0.1	16854	7.8
5	25	16770	7.9
	10	15502	9.2
	5	14465	9.6
	1	11908	11.2
	0.5	10917	11.8
	0.1	8612	15.5
20	25	9275	16.6
	10	7999	16.9
	5	6849	19.3
	1	4618	23.4
	0.5	3902	25.2
	0.1	2498	35.3
40	25	2507	35.7
	10	1751	36.3
	5	1346	37.0
	1	805	38.9
	0.5	576	36.5
	0.1	357	33.9
54	25	879	40.4
	10	600	37.7
	5	473	36.6
	1	291	31.6
	0.5	257	28.5
	0.1	203	25.1

Table A.8 Complex Modulus Test Result Data for I19B Mixture

Temperature (C)	Frequency (Hz)	Average E* (MPa)	Average Phase Angle (deg)
-10	25	23712	5.6
	10	23086	5.3
	5	22375	5.4
	1	20152	6.1
	0.5	19347	6.3
	0.1	17249	6.8
5	25	16923	8.5
	10	15549	9.8
	5	14527	10.1
	1	12130	11.4
	0.5	11196	12.0
	0.1	9042	14.9
20	25	9113	16.6
	10	7836	17.9
	5	6900	19.3
	1	4863	22.9
	0.5	4160	24.4
	0.1	2720	29.2
40	25	2545	32.9
	10	1864	35.8
	5	1472	36.7
	1	816	38.1
	0.5	666	38.2
	0.1	406	36.8
54	25	861	38.9
	10	600	38.4
	5	465	36.8
	1	272	32.8
	0.5	229	30.6
	0.1	161	26.7

Table A.9 Complex Modulus Test Result Data for RS12.5C Mixture

Temperature (C)	Frequency (Hz)	Average E* (MPa)	Average Phase Angle (deg)
-10	25	28303	3.0
	10	27436	3.3
	5	26672	3.6
	1	24456	4.4
	0.5	23566	4.6
	0.1	21115	5.4
5	25	21042	6.2
	10	19549	7.3
	5	18462	7.7
	1	15696	9.0
	0.5	14592	9.5
	0.1	11991	11.4
20	25	12367	13.4
	10	10838	14.3
	5	9586	15.9
	1	6945	19.3
	0.5	5959	20.9
	0.1	3951	26.6
40	25	3673	28.7
	10	2756	31.6
	5	2155	32.7
	1	1309	37.0
	0.5	963	34.5
	0.1	541	32.1
54	25	1280	37.0
	10	899	35.8
	5	683	33.2
	1	405	30.1
	0.5	332	27.7
	0.1	237	23.1

Table A.10 Complex Modulus Test Result Data for RI19B Mixture

Temperature (C)	Frequency (Hz)	Average E* (MPa)	Average Phase Angle (deg)
-10	25	27737	3.3
	10	26836	3.5
	5	26045	3.7
	1	23985	4.3
	0.5	23119	4.4
	0.1	20910	5.0
5	25	20786	6.0
	10	19353	7.3
	5	18272	7.6
	1	15580	8.8
	0.5	14529	9.5
	0.1	11941	12.3
20	25	12152	14.0
	10	10666	15.1
	5	9404	16.8
	1	6663	20.9
	0.5	5752	22.6
	0.1	3693	27.8
40	25	3379	31.4
	10	2420	34.1
	5	1879	35.5
	1	1041	39.0
	0.5	761	38.1
	0.1	417	36.1
54	25	1021	40.4
	10	711	40.2
	5	532	38.5
	1	295	34.3
	0.5	237	31.5
	0.1	163	25.5

Table A.11 Complex Modulus Test Result Data for RI19C Mixture

Temperature (C)	Frequency (Hz)	Average E* (MPa)	Average Phase Angle (deg)
-10	25	31110	3.0
	10	30162	3.3
	5	29326	3.5
	1	26815	4.4
	0.5	25812	4.7
	0.1	23035	6.1
5	25	22951	6.9
	10	21283	7.9
	5	19964	8.4
	1	16707	10.0
	0.5	15380	10.8
	0.1	12203	13.1
20	25	13095	14.8
	10	11255	16.4
	5	9805	18.6
	1	6662	23.4
	0.5	5588	25.3
	0.1	3459	31.2
40	25	3491	32.9
	10	2489	36.8
	5	1909	37.9
	1	1013	37.6
	0.5	802	37.4
	0.1	454	32.6
54	25	1105	38.4
	10	799	38.7
	5	609	37.0
	1	361	31.1
	0.5	298	28.3
	0.1	218	23.4

Table A.12 Complex Modulus Test Result Data for RB25B Mixture

Temperature (C)	Frequency (Hz)	Average E* (MPa)	Average Phase Angle (deg)
-10	25	25220	2.0
	10	24469	2.2
	5	23818	2.3
	1	21907	3.1
	0.5	21148	3.3
	0.1	19276	3.7
5	25	18824	4.6
	10	17460	6.0
	5	16456	6.5
	1	14048	7.9
	0.5	13028	8.7
	0.1	10672	11.2
20	25	11299	12.5
	10	9766	14.5
	5	8649	15.8
	1	6178	19.8
	0.5	5274	21.6
	0.1	3479	27.0
40	25	3437	29.1
	10	2523	32.8
	5	1965	33.9
	1	1100	36.1
	0.5	883	36.3
	0.1	474	32.7
54	25	1217	37.8
	10	843	36.7
	5	648	36.1
	1	370	31.8
	0.5	297	29.3
	0.1	199	25.2

Appendix B Comparison of DMR and I

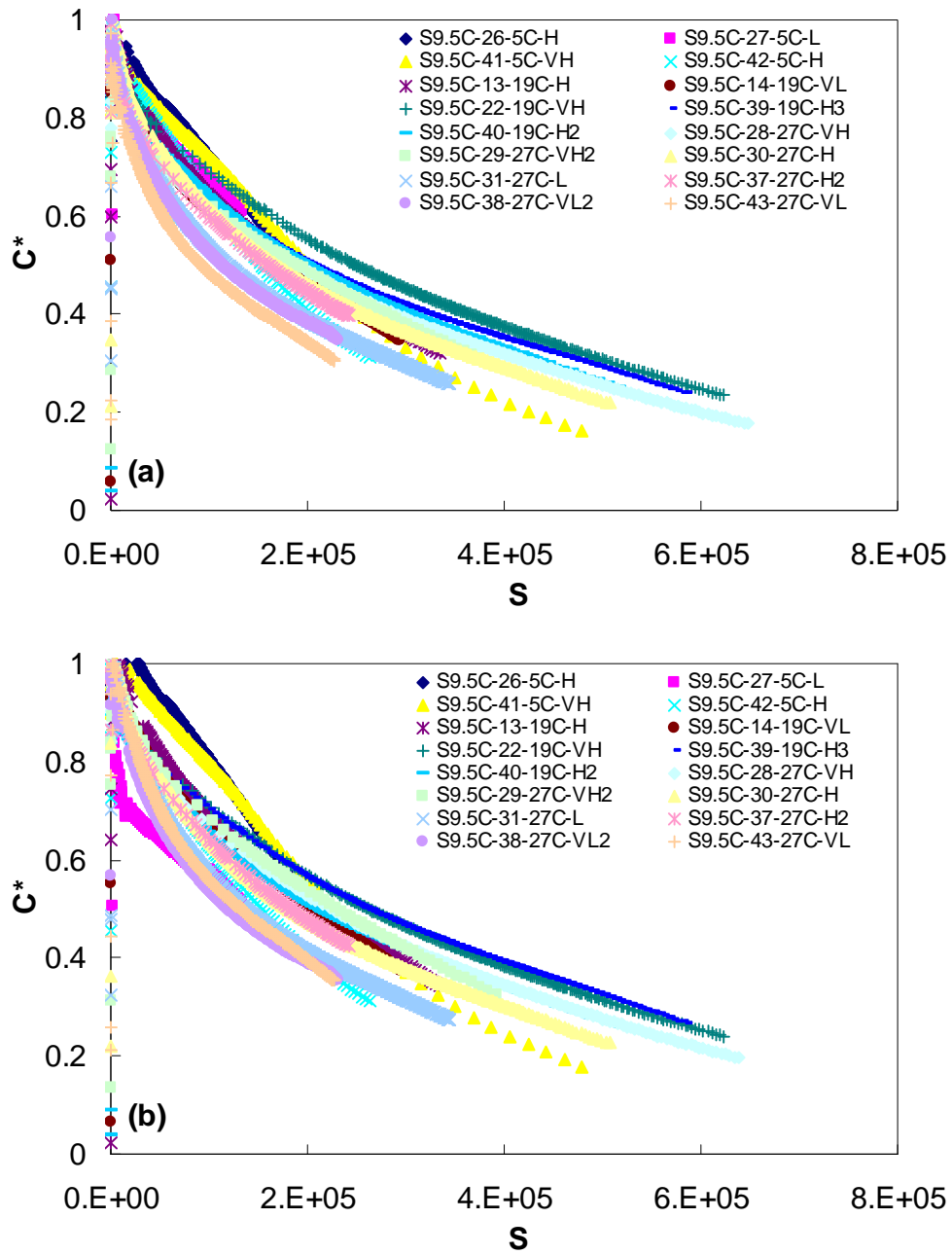


Figure B. 1 Damage curves for S9.5C mixture using (a) DMR and (b) I as specimen-to-specimen variability factor

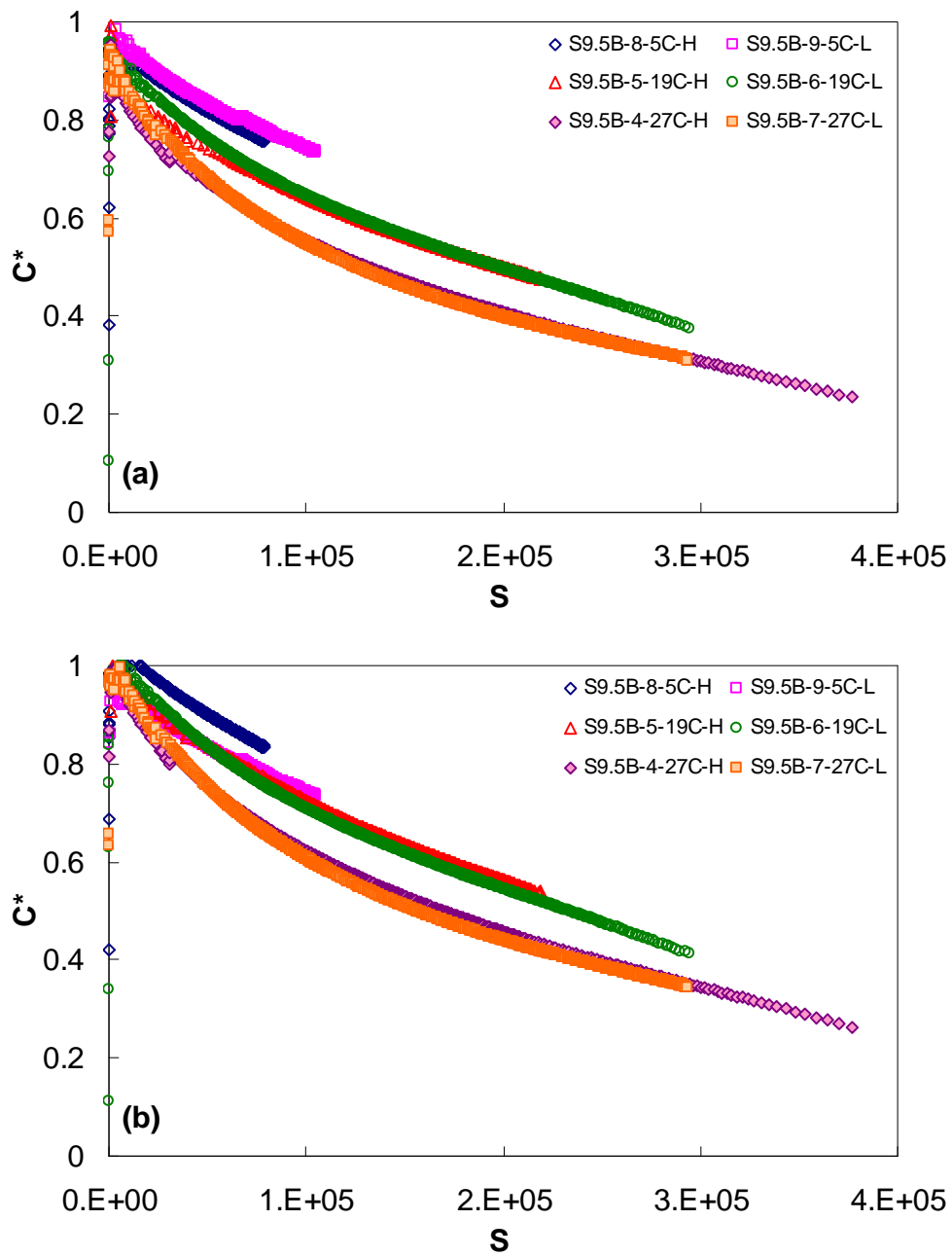


Figure B. 2 Damage curves for S9.5B mixture using (a) DMR and (b) I as specimen-to-specimen variability factor

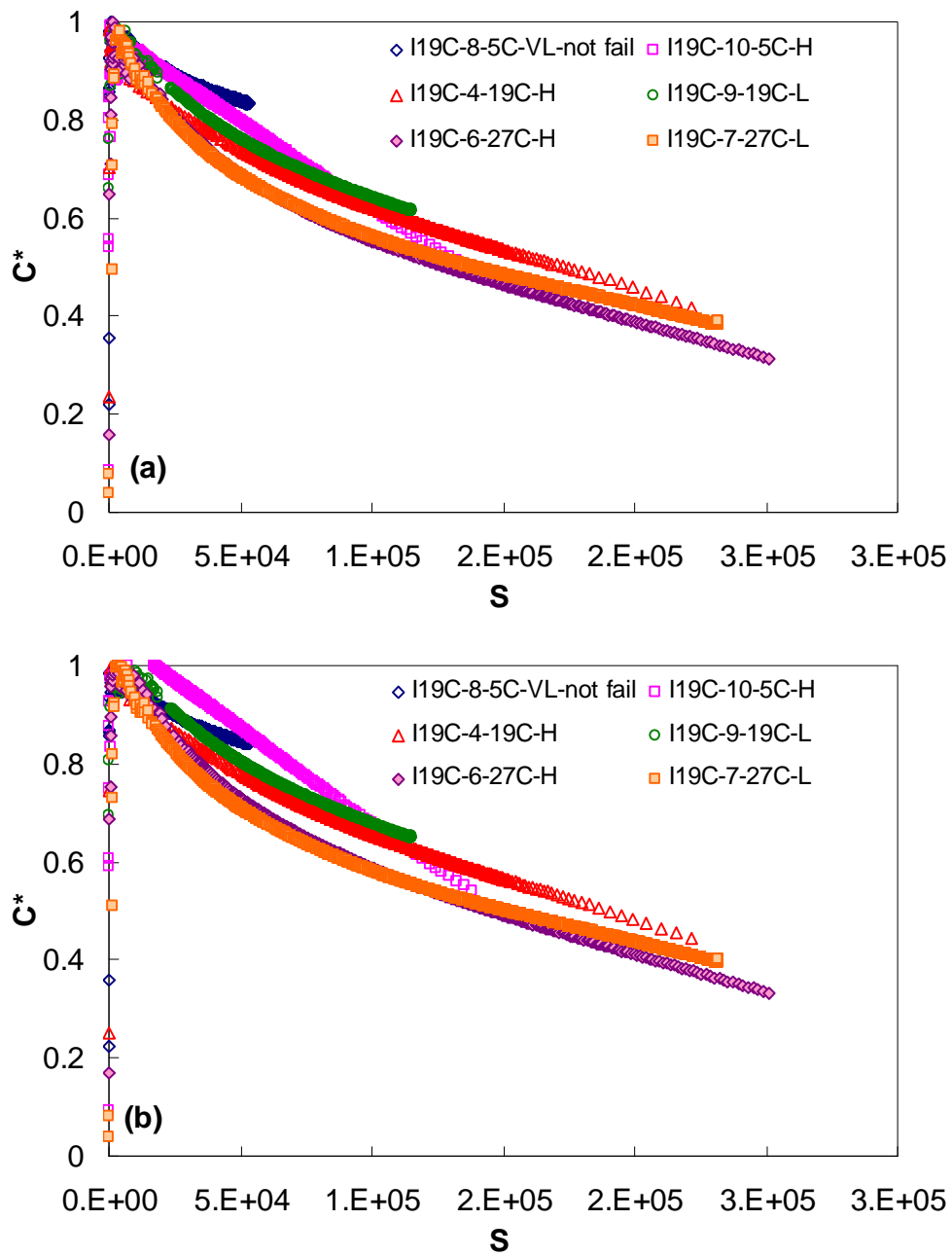


Figure B. 3 Damage curves for I19C mixture using (a) DMR and (b) I as specimen-to-specimen variability factor

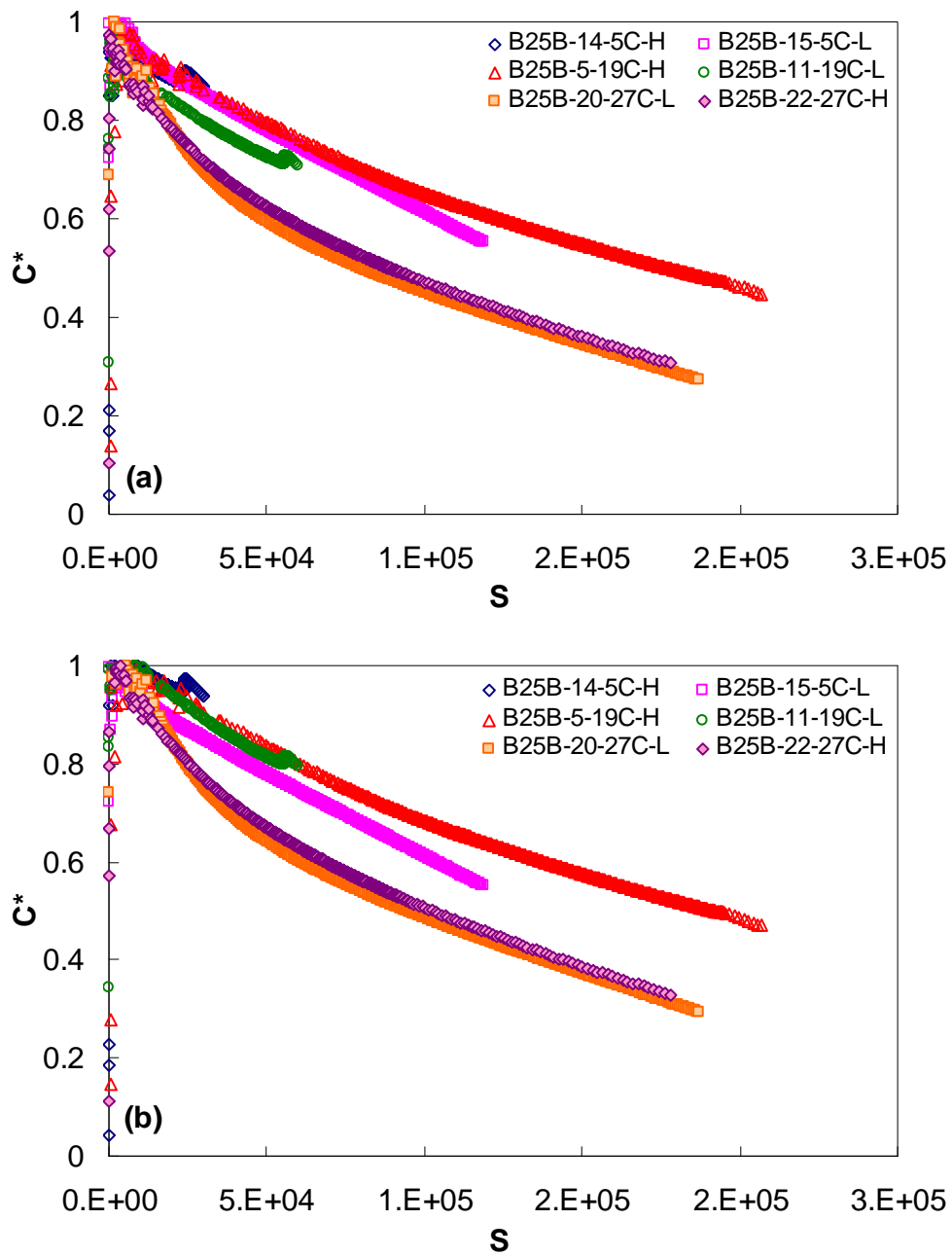


Figure B. 4 Damage curves for B25B mixture using (a) DMR and (b) I as specimen-to-specimen variability factor

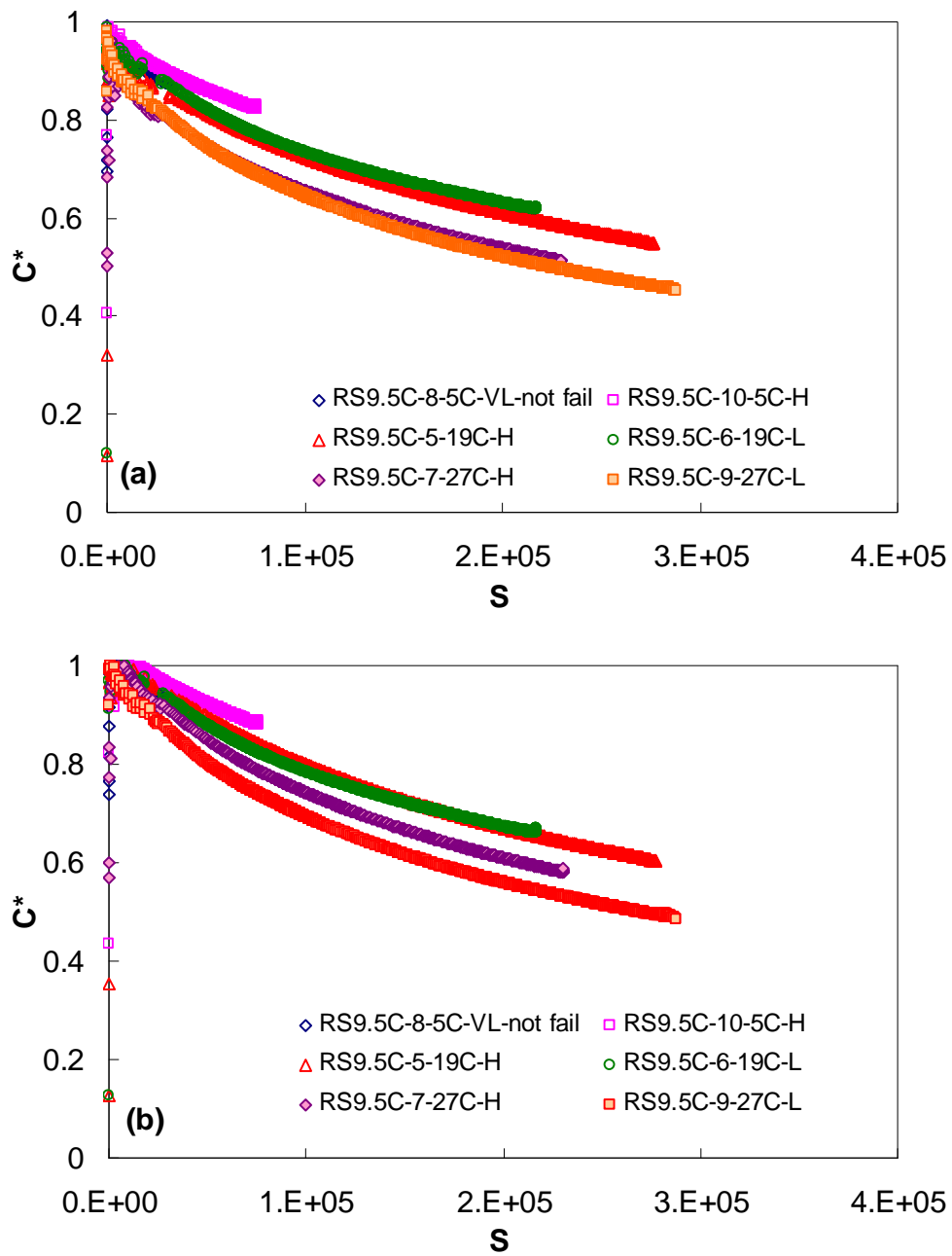


Figure B. 5 Damage curves for RS9.5C mixture using (a) DMR and (b) I as specimen-to-specimen variability factor

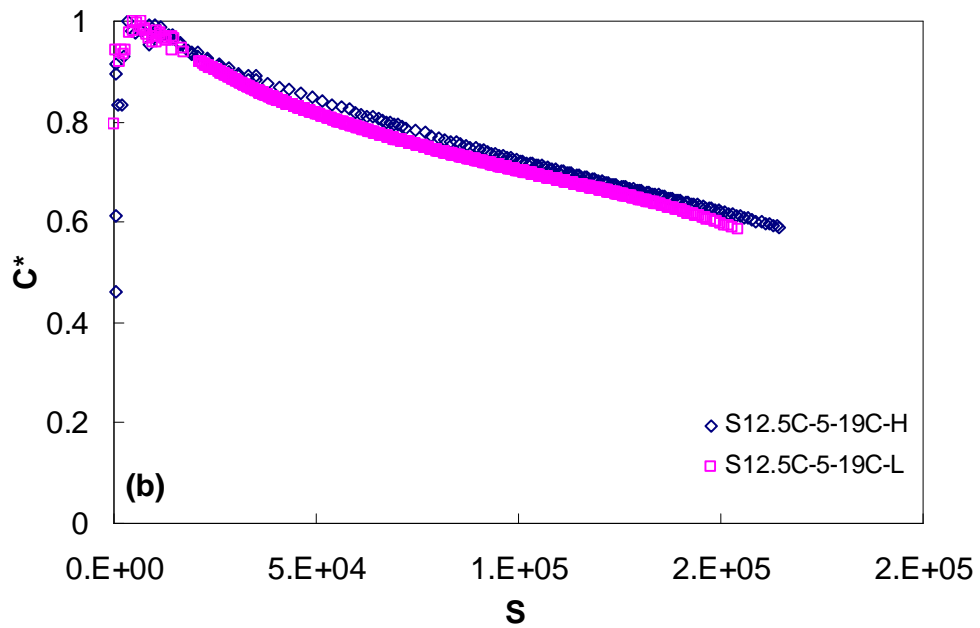
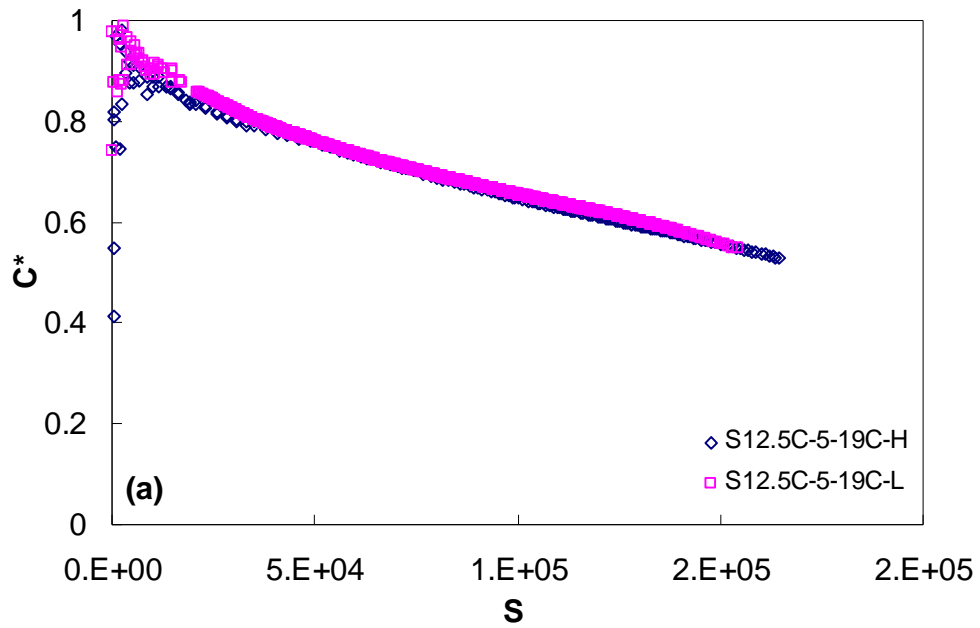


Figure B. 6 Damage curves for S12.5C mixture using (a) DMR and (b) I as specimen-to-specimen variability factor

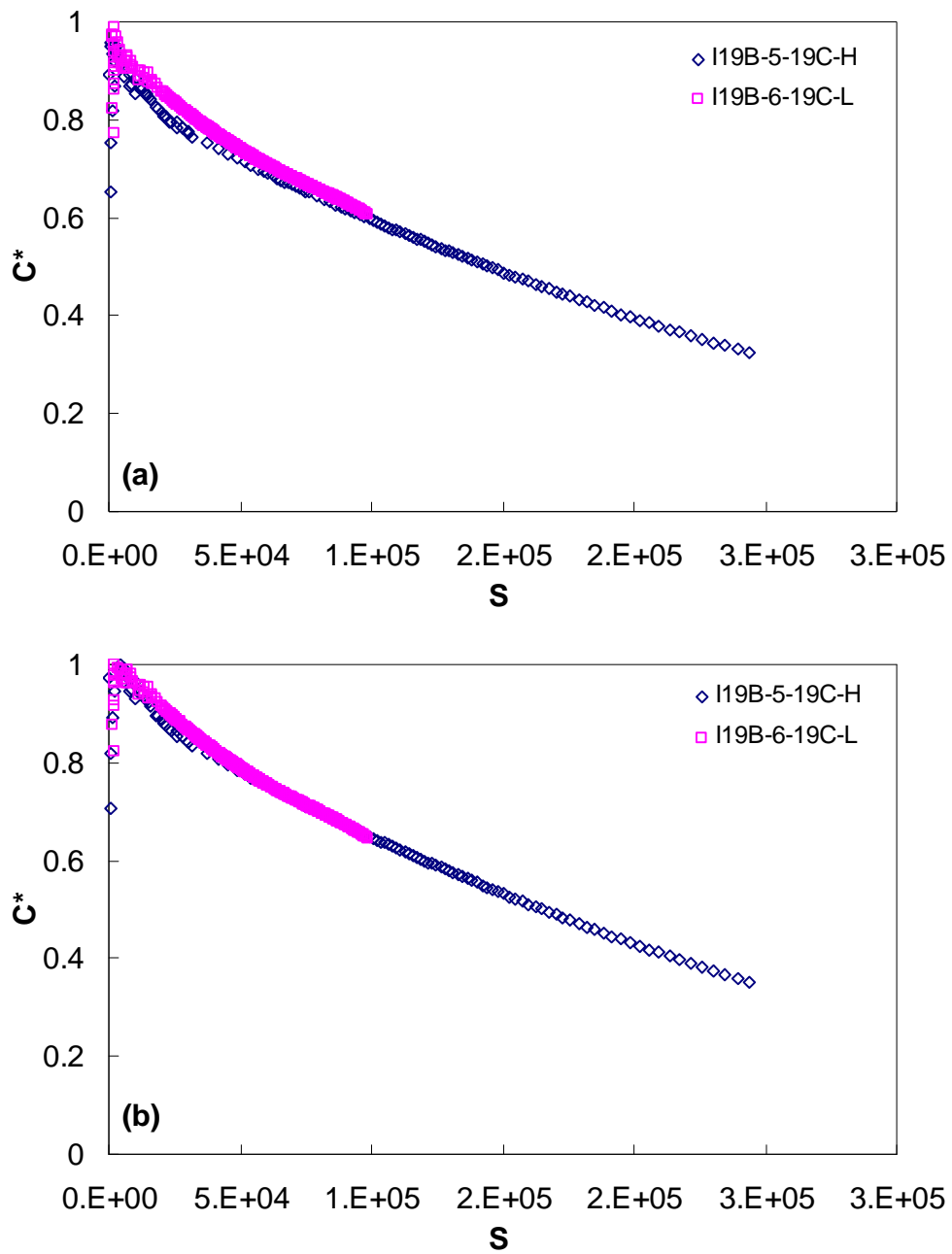


Figure B. 7 Damage curves for I19B mixture using (a) DMR and (b) I as specimen-to-specimen variability factor

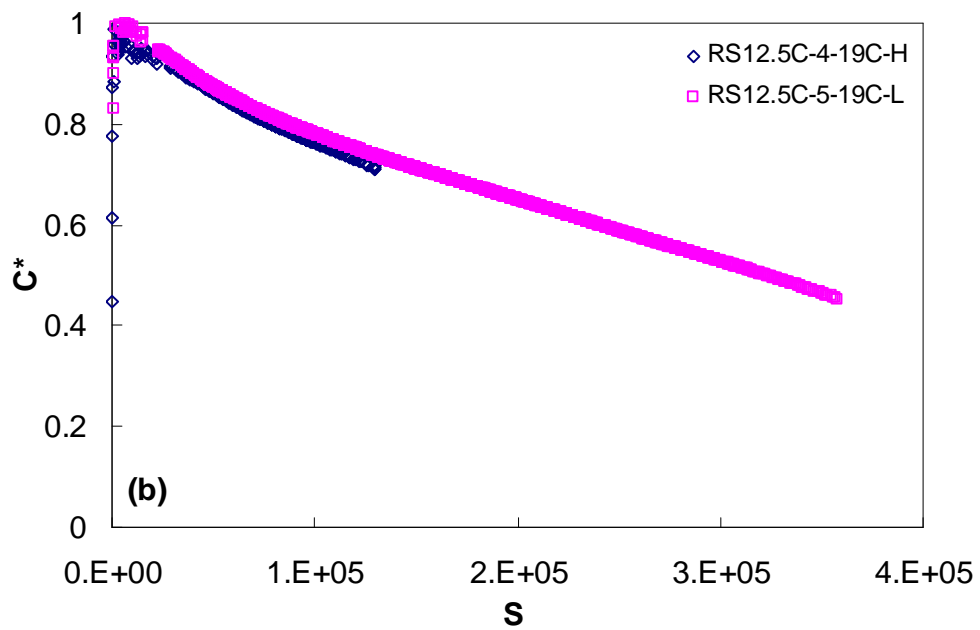
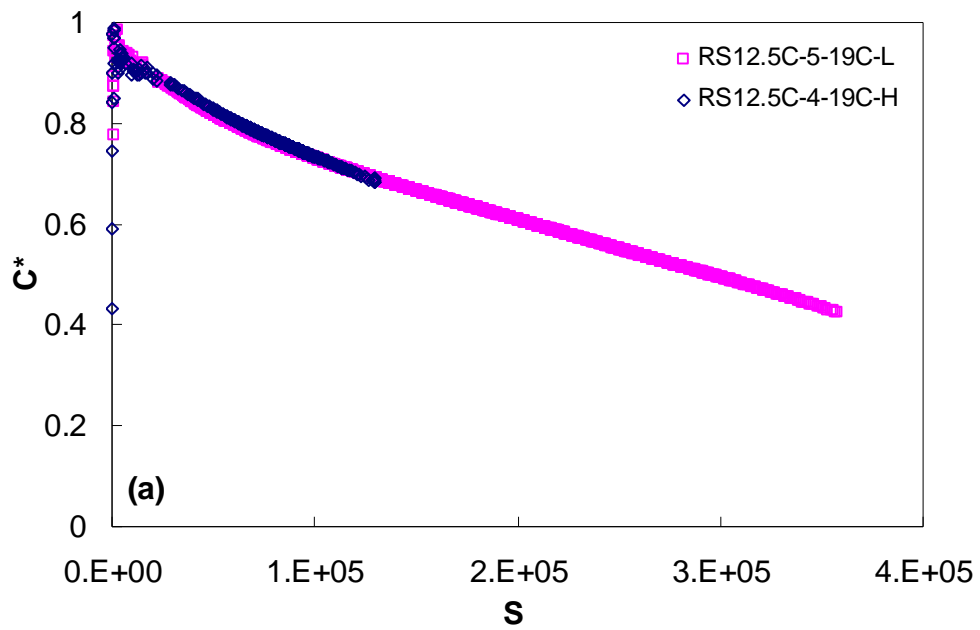


Figure B. 8 Damage curves for RS12.5C mixture using (a) DMR and (b) I as specimen-to-specimen variability factor

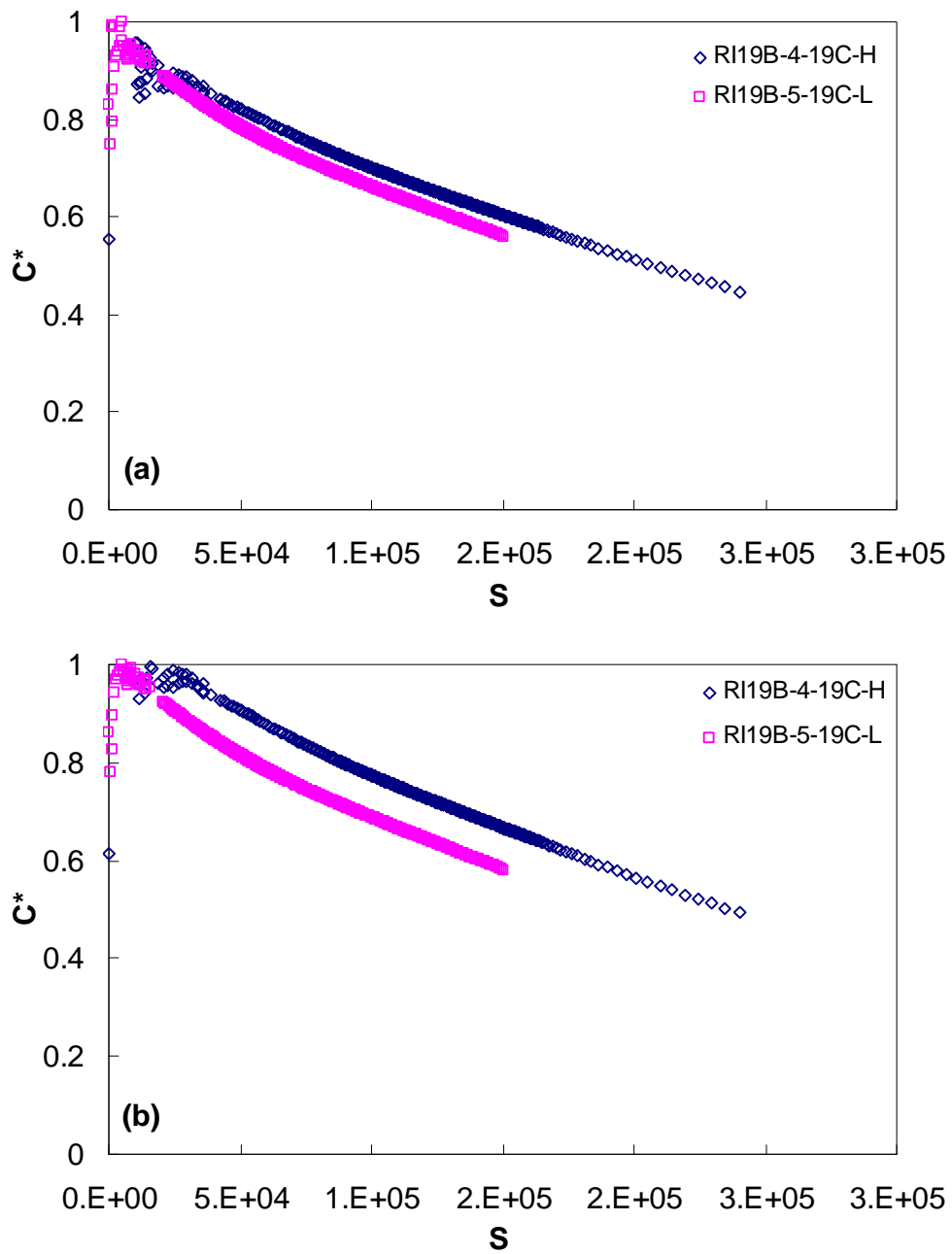


Figure B. 9 Damage curves for RI19B mixture using (a) DMR and (b) I as specimen-to-specimen variability factor

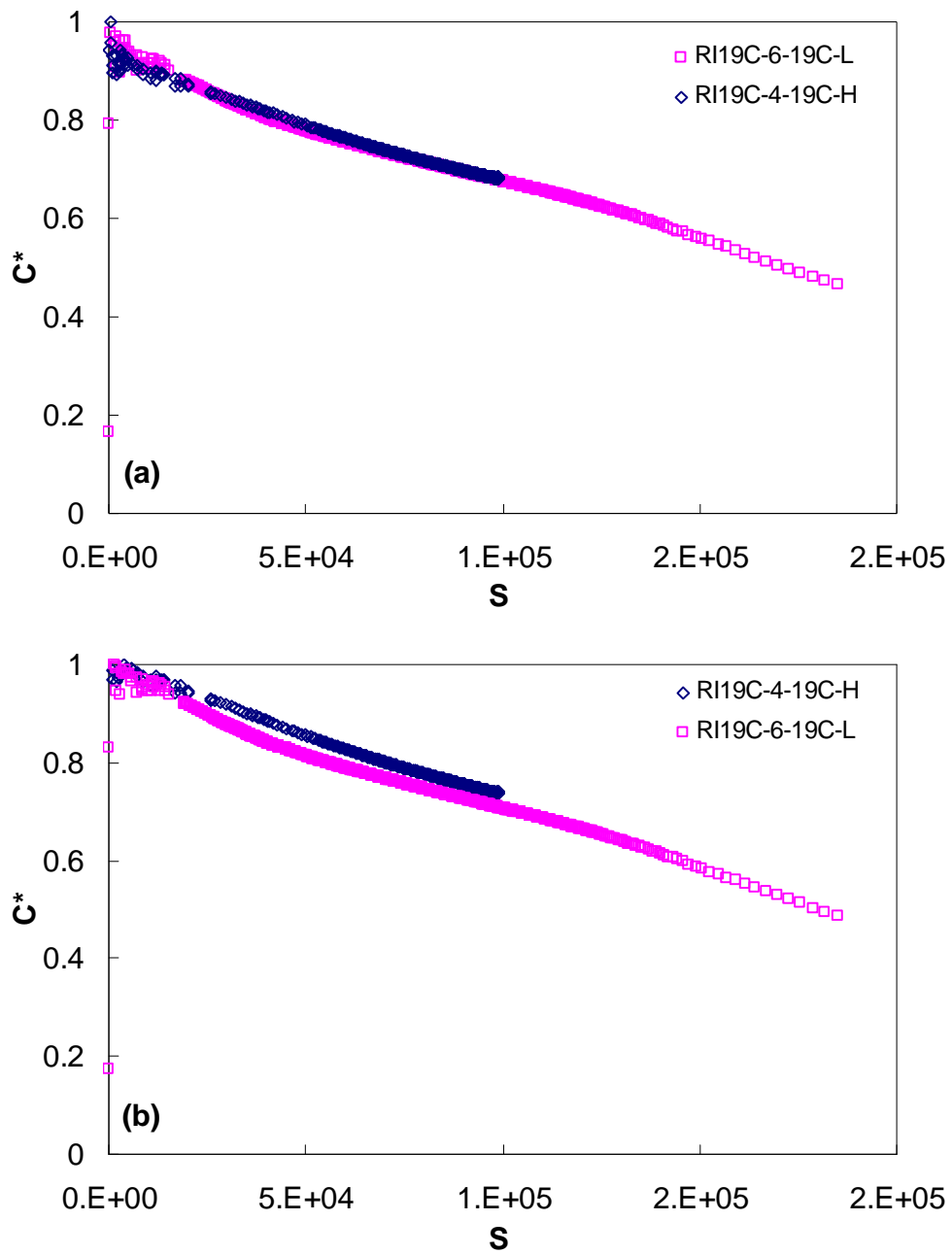


Figure B. 10 Damage curves for RI19C mixture using (a) DMR and (b) I as specimen-to-specimen variability factor

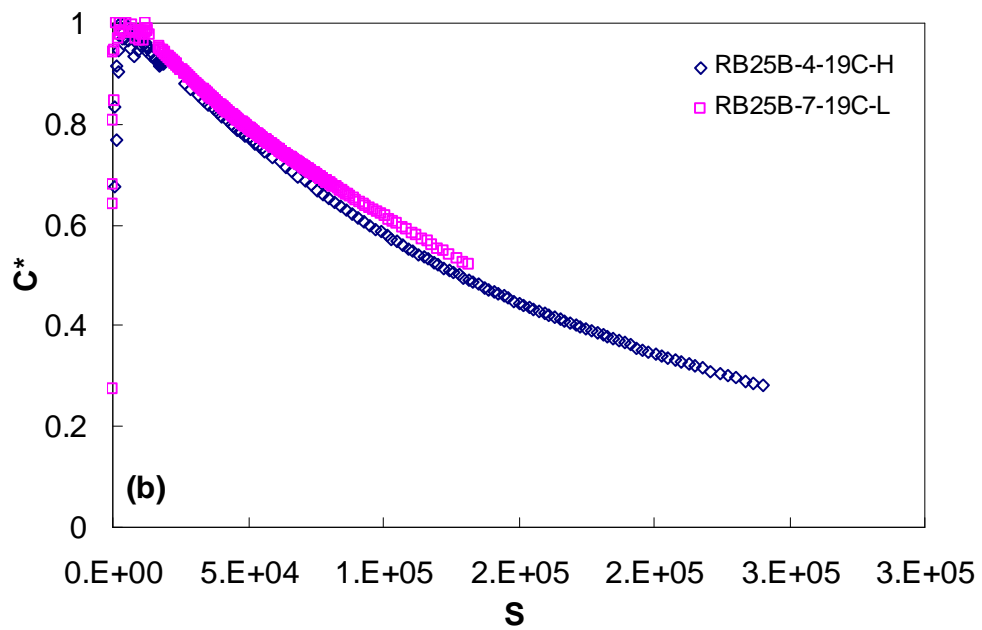
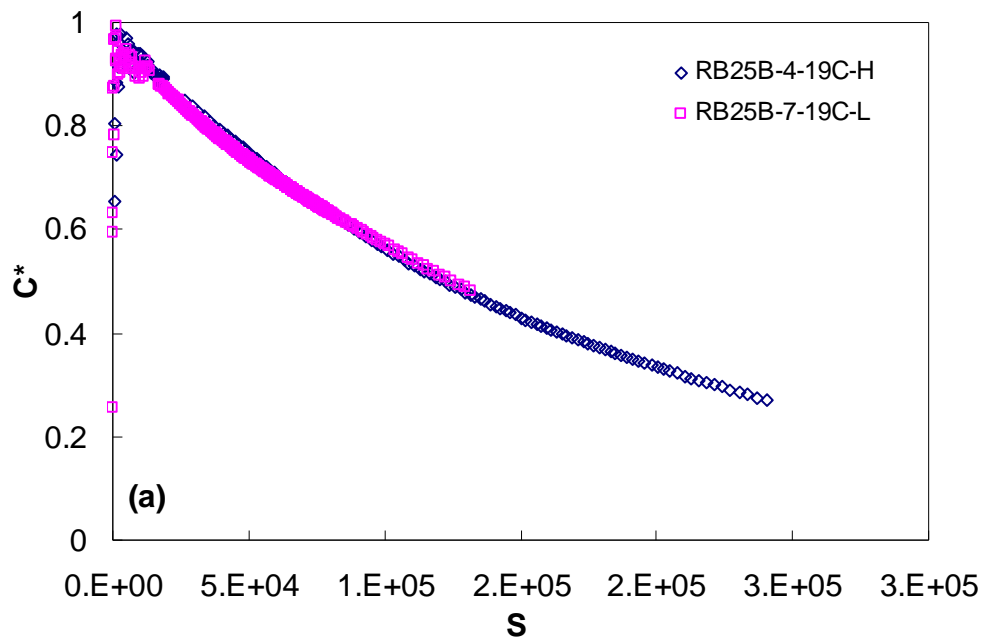


Figure B. 11 Damage curves for RB25B mixture using (a) DMR and (b) I as specimen-to-specimen variability factor

Appendix C Damage Characterization Data

Table C. 1 Viscoelastic damage characterization coefficients for all mixtures

Mixture	Parameters		
	C_{11}	C_{12}	α
S9.5C	0.003881	0.397445	4.126583
S9.5B	0.000900	0.518480	4.126662
I19C	0.000297	0.618120	3.637603
B25B	0.000240	0.630360	3.753415
RS9.5C	0.000687	0.517349	3.773737
S12.5C	0.000592	0.554818	3.951061
I19B	0.000348	0.611581	4.045163
RS12.5C	0.000425	0.559518	4.000179
RI19B	0.000220	0.635777	3.695799
RI19C	0.000578	0.548996	3.804381
RB25B	0.000156	0.687772	3.881082

Appendix D Comparison of Different Failure Definitions in Cyclic Test

Although the advantage of using phase angle failure definition over the empirical 50% stiffness deduction failure definition has been stated clearly in Chapter 3, it is still interesting to examine their relationships through actual test results. The fatigue lives defined by these two methods for all mixtures are listed in

Table D. 1, and they are plotted against each other in the following graphs, together with a linear of equality. Note that those end-failure test results are not included for failure definition comparison.

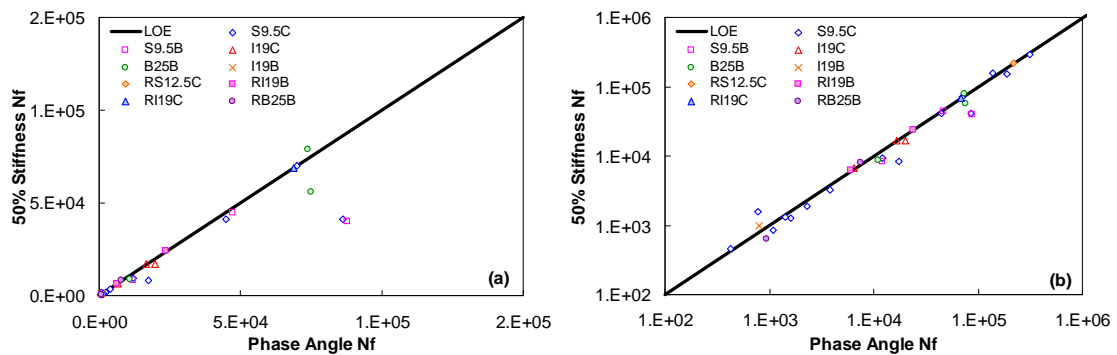


Figure D. 1 Comparison of different failure definitions: (a) arithmetic scale; (b) log scale

Figure D. 1 shows that phase angle method tends to give a slightly longer fatigue life than the 50% stiffness method. However, in general, the differences between these two methods are quite small, usually within 25%.

Table D. 1 Experimental measured fatigue lives by two different definitions

Material	Specimen Name	N_f (phase angle)	N_f (50% Stiffness)
S9.5C	S9.5C-28	1600	1250
	S9.5C-29	420	453
	S9.5C-30	17500	8460
	S9.5C-31	86100	41223
	S9.5C-37	780	1580
	S9.5C-43	190000	149208
	S9.5C-13	45000	40927
	S9.5C-14	311000	290505
	S9.5C-22	2280	1870
	S9.5C-39	3780	3290
	S9.5C-40	12100	9350
	S9.5C-26	70000	70041
	S9.5C-27	140000	157813
	S9.5C-41	1430	1290
	S9.5C-42	1100	853
S9.5B	S9.5B-4	12100	8380
	S9.5B-6	47000	44587
	S9.5B-7	87900	40200
I19C	I19C-4	6500	6742
	I19C-6	19900	16800
	I19C-10	16600	16765
B25B	B25B-18	73800	78729
	B25B-20	75000	56022
	B25B-22	11000	8560
I19B	I19B-5	800	972
RS12.5C	RS12.5C-5	220000	217336
RI19B	RI19B-4	6000	6333
	RI19B-5	23700	23835
RI19C	RI19C-6	68900	69052
RB25B	RB25B-4	950	643
	RB25B-7	7550	8155

Appendix E Fatigue Test Prediction Results

Table E. 1 Summary of fatigue test prediction results

Material	Specimen Name	Temperature (C)	Failure Location	Measured N _f	Predicted N _f	Prediction Error (%)
S9.5C	S9.5C-28	26.80	middle	1600	1420	11
	S9.5C-29	26.80	middle	420	440	5
	S9.5C-30	26.80	middle	17500	16369	6
	S9.5C-31	26.60	middle	86100	103682	20
	S9.5C-37	26.95	middle	780	1190	53
	S9.5C-38	26.80	end	165000	278603	69
	S9.5C-43	27.40	middle	190000	212829	12
	S9.5C-13	19.05	middle	45000	51806	15
	S9.5C-14	19.00	middle	311000	385469	24
	S9.5C-22	18.50	middle	2280	2245	2
	S9.5C-39	18.70	middle	3780	3360	11
	S9.5C-40	18.80	middle	12100	12088	0
	S9.5C-26	5.00	middle	70000	84612	21
	S9.5C-27	4.90	middle	140000	181083	29
	S9.5C-41	4.60	middle	1430	1420	1
S9.5C-42	5.30	middle	1100	1310	19	
S9.5B	S9.5B-4	27.40	middle	12100	10400	14
	S9.5B-5	19.20	end	4570	5531	21
	S9.5B-6	19.30	middle	47000	50909	8
	S9.5B-7	27.30	middle	87900	106620	21
	S9.5B-8	5.50	end	4600	6041	31
	S9.5B-9	5.50	end	198000	257996	30
I19C	I19C-4	19.15	middle	6500	5555	15
	I19C-6	27.40	middle	19900	22880	15
	I19C-7	27.40	end	217000	113400	48
	I19C-8	5.40		>277200 ^a	355473	
	I19C-9	19.50	end	27000	31687	17
	I19C-10	5.15	middle	16600	18423	11

Table E. 1 Continued

Material	Specimen Name	Temperature (C)	Failure Location	Measured N_f	Predicted N_f	Prediction Error (%)
B25B	B25B-5	19.10	end	4780	5176	8
	B25B-11	19.10	end	7160	12364	73
	B25B-14	5.40	end	11000	16980	54
	B25B-18	5.15	middle	73800	78020	6
	B25B-20	27.50	middle	75000	104470	39
	B25B-22	27.40	middle	11000	13812	26
RS9.5C	RS9.5C-5	19.40	end	44000	49513	13
	RS9.5C-6	19.60	end	148000	191711	30
	RS9.5C-7	27.30	end	27500	44222	61
	RS9.5C-8	5.15		>168000 ^a	231008	
	RS9.5C-9	27.35	end	79000	111266	41
	RS9.5C-10	5.35	end	41000	61350	50
S12.5C	S12.5C-4	19.20	end	1250	2140	71
	S12.5C-5	19.20	end	74100	106659	44
I19B	I19B-5	19.00	middle	800	600	25
	I19B-6	19.20	end	19000	23741	25
RS12.5C	RS12.5C-4	19.10	end	9330	12716	36
	RS12.5C-5	19.00	middle	220000	230711	5
RI19B	RI19B-4	19.45	middle	6000	6071	1
	RI19B-5	19.50	middle	23700	28732	21
RI19C	RI19C-4	19.35	end	3450	5020	46
	RI19C-6	19.20	middle	68900	85294	24
RB25B	RB25B-4	19.20	middle	950	430	55
	RB25B-7	19.20	middle	7550	7682	2

^a Test stopped at that number of loading cycle and specimen didn't fail